DTIC FILE COPY

Energy

(1)

AD-A225 624

IRS

INSTITUT FÜR RAUMFAHRTSYSTEME
UNIVERSITÄT STUTTGART

PFAFFENWALDRING 31
7000 STUTTGART 80 (VAIHINGEN)

90 08 13 145

IRS-90-P4
Institut für Raumfahrtsysteme
Universität Stuttgart

Grant AFOSR-88-0325

High Power Steady State MPD Thruster

Final Report
Covering Period September 1, 1988 - August 31, 1989

Authors:

Monika Auweter-Kurtz
Helmut Kurtz
Wolfgang Merke
Herbert Schrade - Principal Investigator
Christian Sleziona
Thomas Wegmann

DTIC
ELECTE
AUG 15 1990
S D
B

Prepared for the
Air Force Astronautics Laboratory
Edwards Air Force Base
Edwards, CA.

March 1990

90 08 13 145

DISTRIBUTION STATEMENT A
Approved for public release;
Distribution Unlimited

SECURITY CLASSIFICATION OF THIS PAGE

REPORT DOCUMENTATION PAGE

Form Approved OMB No. 0704-0188

1a REPORT SECURITY CLASSIFICATION unclassified	1b RESTRICTIVE MARKINGS
2a SECURITY CLASSIFICATION AUTHORITY	3. DISTRIBUTION/AVAILABILITY OF REPORT Approved for public release Distribution is unlimited
2b DECLASSIFICATION/DOWNGRADING SCHEDULE	
4 PERFORMING ORGANIZATION REPORT NUMBER(S) IRS-90-P4	5 MONITORING ORGANIZATION REPORT NUMBER(S)
6a NAME OF PERFORMING ORGANIZATION Institut für Raumfahrt-systeme, Univ. Stuttgart 6b OFFICE SYMBOL (If applicable) IRS	7a. NAME OF MONITORING ORGANIZATION EOARD/LRL
6c ADDRESS (City, State, and ZIP Code) Pfaffenwaldring 31 D-7000 Stuttgart 80, West Germany	7b ADDRESS (City, State, and ZIP Code) Box 14 FPO New York, NY 09510-0200
8a NAME OF FUNDING/SPONSORING ORGANIZATION AFAL 8b. OFFICE SYMBOL (If applicable) LSVE	9 PROCUREMENT INSTRUMENT IDENTIFICATION NUMBER Grant AFOSR-88-0325
8c ADDRESS (City, State, and ZIP Code) Edwards AFB, CA 93523-5000	10. SOURCE OF FUNDING NUMBERS PROGRAM ELEMENT NO. / PROJECT NO. / TASK NO. / WORK UNIT ACCESSION NO

11 TITLE (Include Security Classification)
High Power Steady State MPD Thruster (U)

12 PERSONAL AUTHOR(S)
M.Auweter-Kurtz, H. Kurtz, W. Merke, H. Schrade, C. Sleziona, T. Wegmann

13a TYPE OF REPORT	13b TIME COVERED	14. DATE OF REPORT (Year, Month, Day)	15. PAGE COUNT
Final	FROM 09/1/88 TO 8/31/89	90/4	68

16 SUPPLEMENTARY NOTATION

17. COSATI CODES			18. SUBJECT TERMS (Continue on reverse if necessary and identify by block number)
FIELD	GROUP	SUB-GROUP	Steady State Magnetoplasmadynamic Thrusters; Electric Propulsion; Cathodes

19 ABSTRACT (Continue on reverse if necessary and identify by block number)

Rotation symmetric magnetoplasmadynamic thrusters with self induced magnetic fields are investigated at higher current levels in a steady state operation mode. Three thruster development lines are followed:

a) watercooled nozzle type thrusters,
b) partly radiation cooled nozzle type thrusters, and
c) cylindrical watercooled thrusters.

The goal to get 1 MW steady state power input could not be reached in the contract period because of two reasons: the heatflux into the nozzle throat of the investigated DT2 thruster got to unacceptable high values, which has to be overcome by a new construction and both for the nozzle type and cylindrical thrusters the cathode raised problems at high current densities: the thorium oxide agglomerates and the cathodes begin to melt out of their inner zones and become destroyed.

20 DISTRIBUTION/AVAILABILITY OF ABSTRACT ☐ UNCLASSIFIED/UNLIMITED ☒ SAME AS RPT. ☐ DTIC USERS	21 ABSTRACT SECURITY CLASSIFICATION Unclassified
22a NAME OF RESPONSIBLE INDIVIDUAL Terry M. Sanks, 2 Lt., USAF	22b TELEPHONE (Include Area Code) 805-275-5473 22c. OFFICE SYMBOL LSVE

DD Form 1473, JUN 86 Previous editions are obsolete SECURITY CLASSIFICATION OF THIS PAGE

Block 19 continued

Due to a new installed gas purification system, the erosion rates of the cathode could be diminished to values which are in the order of magnitude of the expected sublimation.

The partly radiation cooled "Hot Anode Thruster (HAT)" showed promising results: the discharge voltage with the hot anode is about 7V lower than with the watercooled thruster, so that better efficiencies could be expected.

Accession For	
NTIS GRA&I	☑
DTIC TAB	☐
Unannounced	☐
Justification	
By	
Distribution/	
Availability Codes	
Dist	Avail and/or Special
A-1	

QUALITY INSPECTED 4

Table of Contents

		Page
1.	Introduction	3
2.	High Power Steady State MPD Thruster -Experimental Investigations	4
2.1	Nozzle Type MPD Thruster	4
2.1.1	Thruster Configuration	4
2.1.2	Experimental Results	7
2.1.2.1	Variation of the gas species	7
2.1.2.2	Variation of the cathode position and diameter	16
2.1.2.3	Influence of the mass flow rate	26
2.1.2.4	Variations of the cathode diameter	30
2.1.3	The Onset-Phenomena	34
2.2	Hot Anode Thruster	38
2.3	Cylindrical MPD Thruster	45
3.	Cathode Phenomena	58
3.1.	Erosion Data	58
3.2.	High Temperature - High Current Density Damage of Cathodes	62
4.	Numerical Modeling of the Flow in MPD Accelerators	64
5.	References	68

1. Introduction

With the possible deployment of nuclear space power systems in the near future, new missions also came nearer to realization like manned mars missions or large maneuverable radar satellites or nuclear electric OTVs. One of the most promising candidates or even the only one for the propulsion of these devices is the high power self-field magnetoplasmadynamic thruster working in a continuous mode. Moreover, the specific impulses reached with continuous MPD thrusters in the region between 1000 and 2000 s are optimal in respect of mass savings and trip times for near earth missions, as shown in some recent mission studies [1,2].

But as yet, the high power range for MPDs was only reached with pulsed quasi-steady thrusters, which have inherent disadvantages such as complicated power conditioning and cold cathodes, yielding an intolerably high cathode erosion.

However, because of the missing availability of adequate power supplies and vacuum systems, continuous MPD thrusters were only tested up to some 400kW power level. The objective of this AFOSR contract is to try to raise the operating and testing limits of steady state thrusters up to about 1 MW and to investigate the encountered problems.

On the other hand, this contract is in effect a continuation of the former grants AFOSR F49 62O-82-C-0100, AFOSR-84-0394 [3] and ONR N00014-87-G-0119 [4] which dealt with lower power steady state MPD thruster development.

The submitted report consists of three parts: in section 2 the experiments with high power steady state nozzle type and cylindrical MPD thrusters are described. Further, first results of experiments with hot, glowing anodes in connection with high power steady state MPD thrusters are described. The Hot Anode Thruster (HAT) was initiated and built under the above mentioned preceding contracts, but for manpower and hardware reasons, it could not be tested before 1989. The results are quite promising, so that the lines of investigation will be followed in future. Section 3 shows the effect of gas purification on the erosion of the cathode and the difficulties with the thoriated tungsten as cathode material at high current densities and temperatures. Lastly, in section 4 some improvements in the computer models and codes compared to the corresponding data given in the final report "Plasma Thruster Development" of the ONR grant N00014-87-G-0119 of October 1988 are briefly explained.

2. Nozzle Type MPD Thrusters

2.1. Thruster Configuration

The DT-thruster configuration, shown in Figure 2.1.1, has been developed from many years of research and tests done on the nozzle type MPD thrusters at the IRS.

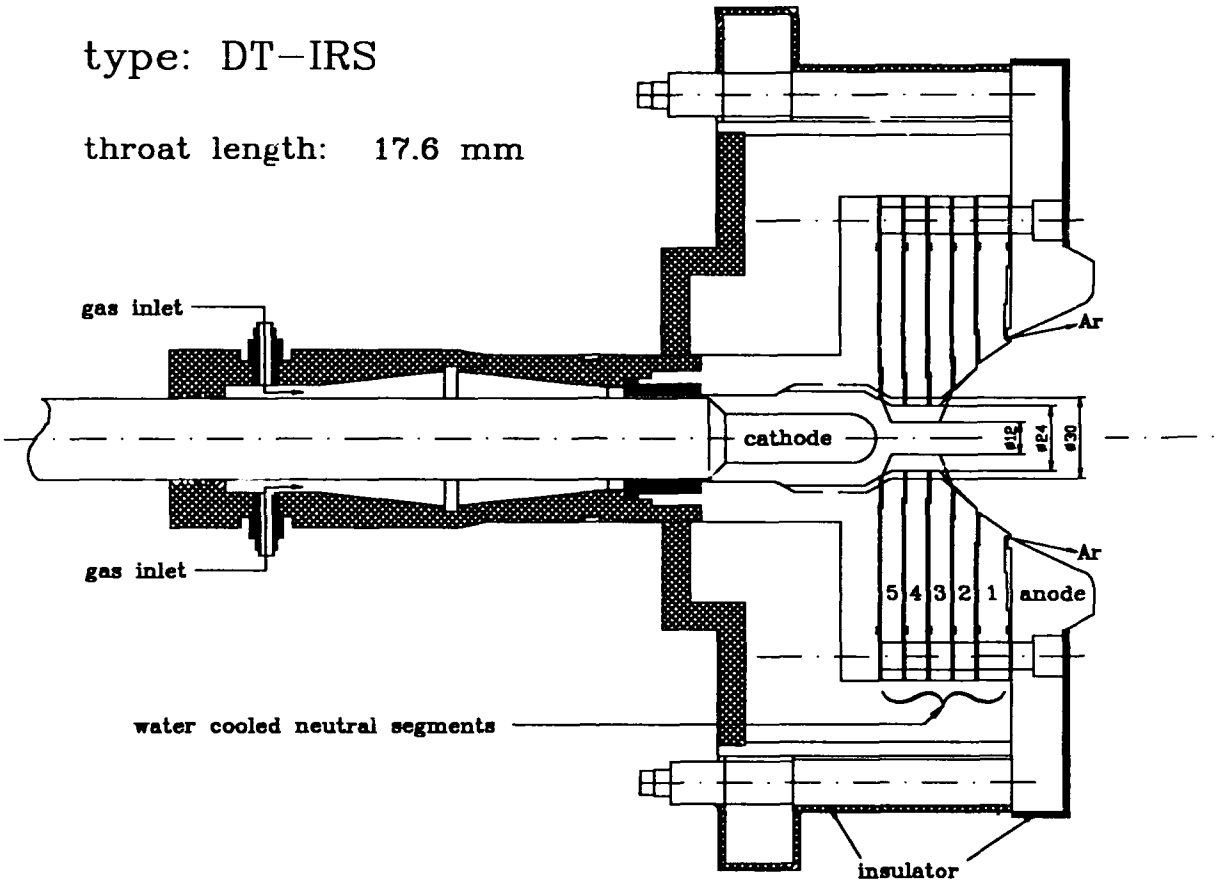

Fig. 2.1.1: Configuration of the DT-thruster-head-series at the IRS

The thruster head consists of an anode, a cathode, an arc chamber, and five neutral segments. The anode and neutral segments are made of copper and are cooled by high-pressure water. The different versions of the DT-thrusters differ in the nozzle throat diameter: for the DT2-thrusters the three throat segments have a diameter of 24mm, for the DT3-thruster this diameter was halved (12mm). The DT5- thruster, under construction has a diameter of 30mm . All other thruster parameters like for example the throat length are identical. The outer anode diameter is 142mm. All parts of the anode with greater diameter are covered with a ceramic insulation, so that the arc's anode attachment region is relatively well defined.

The upstream cathode is made of thoriated (2%) tungsten, which is cast in a water cooled copper rod. Normally it has a diameter of 18mm and is positioned at a distance of 85mm from the exit plane of the thruster.

The propellant is fed mainly through the nozzle chamber, but additional gas can be injected at the anode ring. The total mass flow rate consists of the cathode and anode gas fractions. The anode gas, which is 10% of the anode gas during all tests described in this report, seems to stabilize the arc mainly relative to its symmetry axis.

Except for the tests with hydrogen, where the anode gas was argon, the anode gas species were the same as the cathode gases.

The thruster is installed in a vacuum tank with a length of 5 m and a diameter of 2 m, which has double, water cooled walls. It is mounted on a thrust balance.

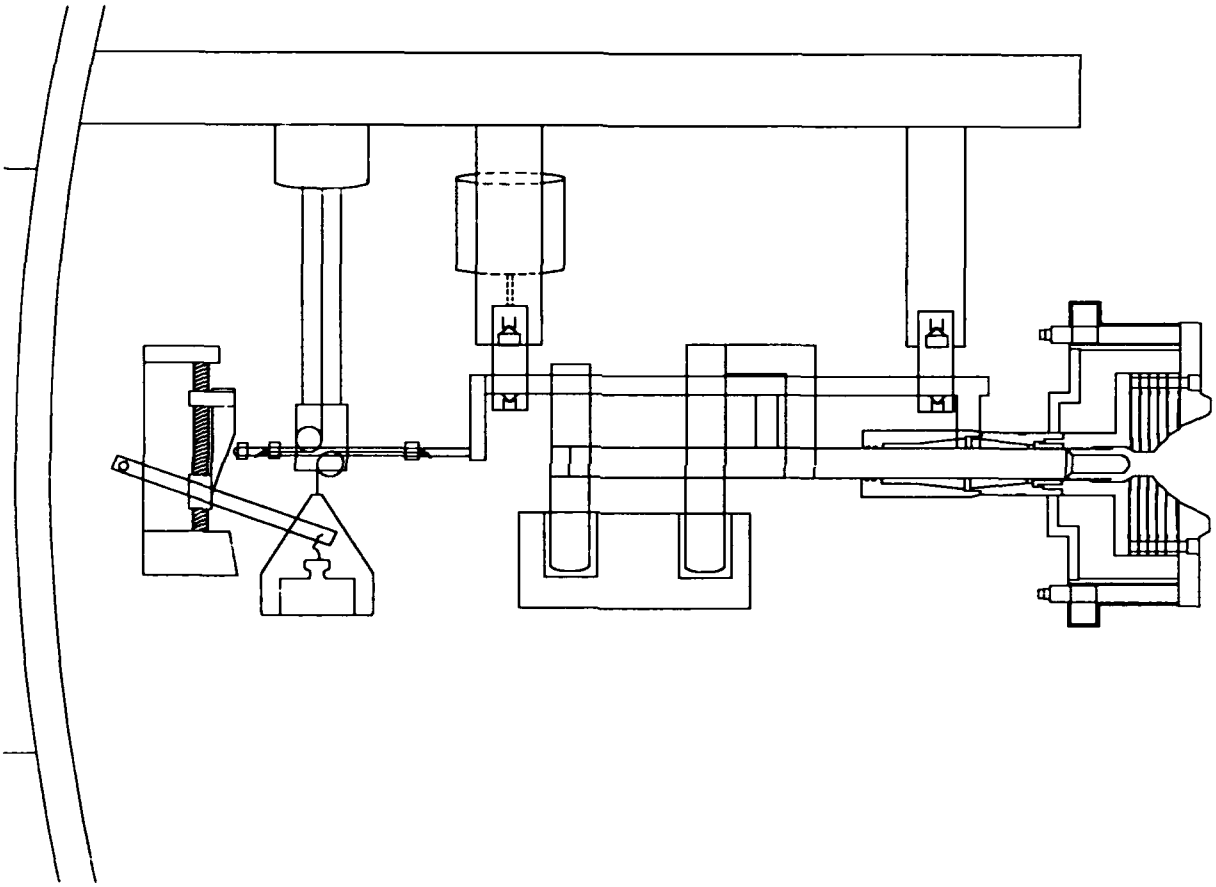

Fig. 2.1.2: Scheme of the thrust balance

This thrust balance is a pendulum thrust balance, positioned on edges. The force is measured by a wire strain gauge force transducer. The current feed to the balance is achieved through mercury baths. Propellant and cooling water are supplied by nylon hoses which form large bows in vertical planes. In order to eliminate errors due to electromagnetic and mechanical interactions, calibration measurements have been performed with the thruster short circuited and with running cooling water. In addition, the thrust balance is remotely calibrated always before and after every test, allowing thrust measurements within an error of less than 2%. The schematic of the thrust stand is shown in Fig. 2.1.2. Further, the current, the discharge voltage, propellant mass throughflow, the discharge chamber pressure, and thermal losses for each thruster segment and for the electrodes are measured.

The data acquisition and control system consists of a multichannel Intercole Spectra data acquisition system controlled by a PDP 11/73, which also controls the gas valves and mass flow controllers. The graphical data reduction is done by IBM compatible PCs. Fig. 2.1.3 shows the scheme of the experimental set-up with the different control loops.

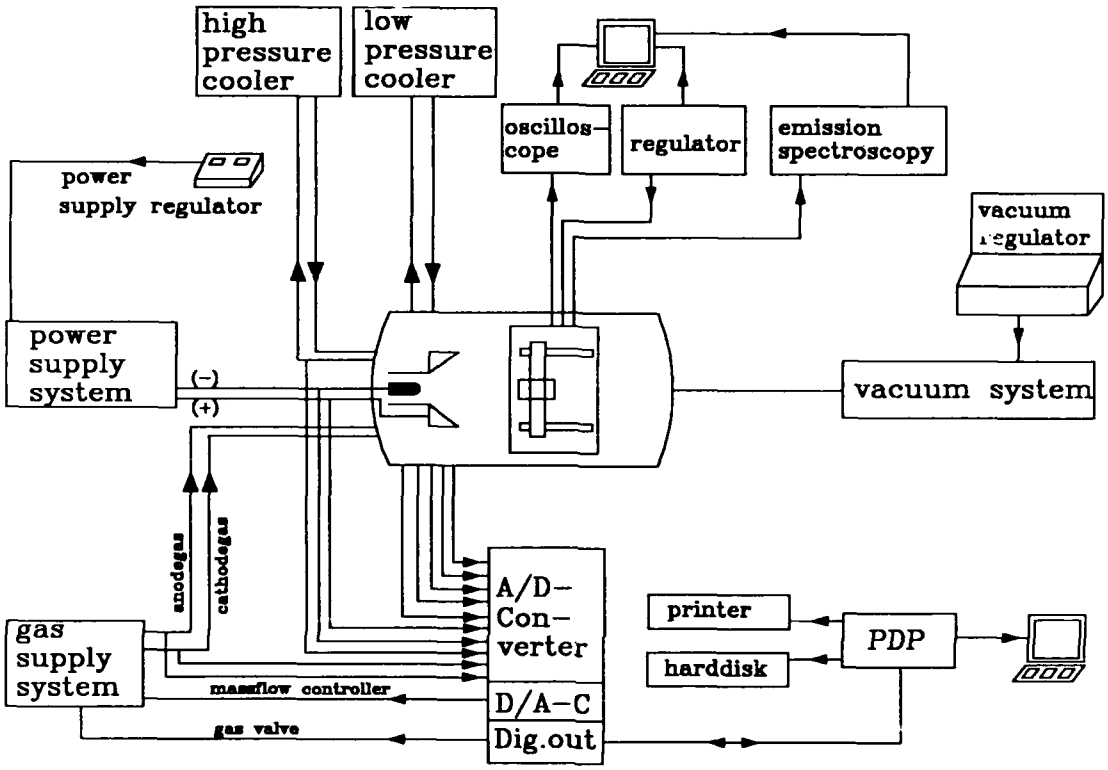

Fig. 2.1.3: Scheme of the supply and data measuring arrangement

2.1.2 Experimental Results

2.1.2.1 Variation of the gas species

At first the characteristic performence data of the DT2-thruster with different gas species as propellant were measured.

Figure 2.1.4 shows the voltage-current dependence of the DT2-thruster running with different gases: hydrogen, nitrogen and argon.

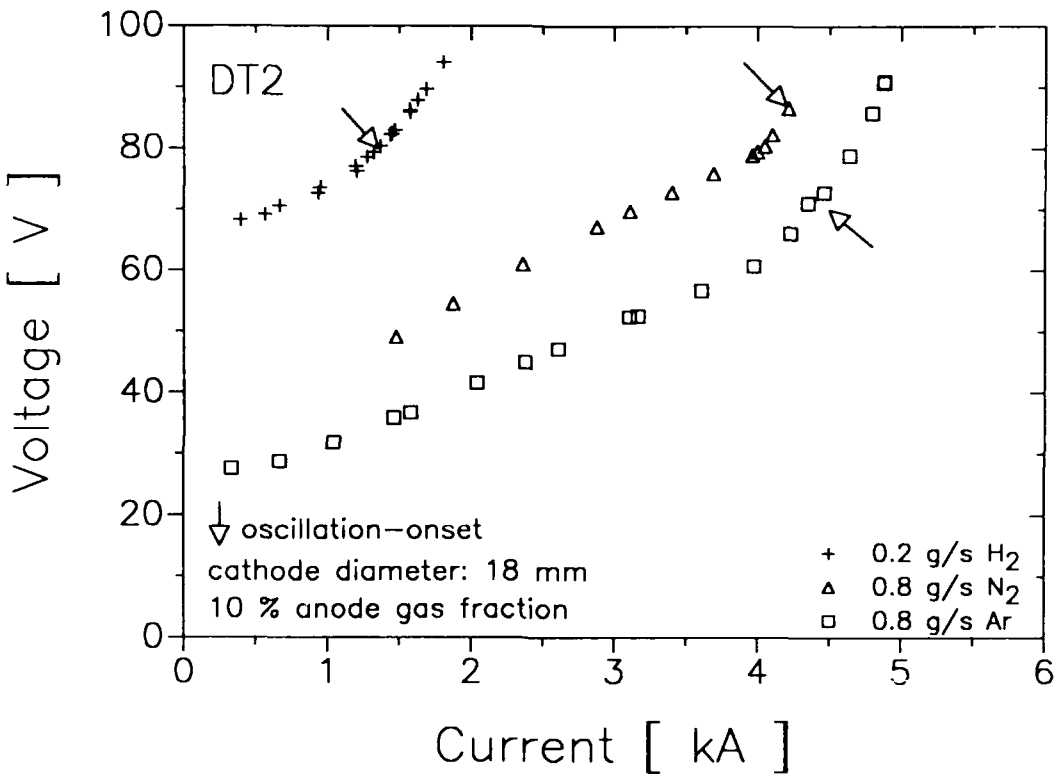

Fig. 2.1.4: Voltage - current dependence of the DT2-Thruster running with various gases

The voltage-current dependence curves are similar for all gases. With increasing power, a break occurs on each voltage-current line, marking a distinct variation in slope. At power levels above these breaks there is an oscillation onset, where plasma instabilities occur. These points are marked in the diagram by arrows. Finally one reaches a point, where the behavior of the plasma jet changes drastically: the normally diffuse arc anode attachment concentrates on one spot and because of the high local thermal stress, the anode will be destroyed.

In chapter 2.1.3 the onset-phenomenon is considered in detail.

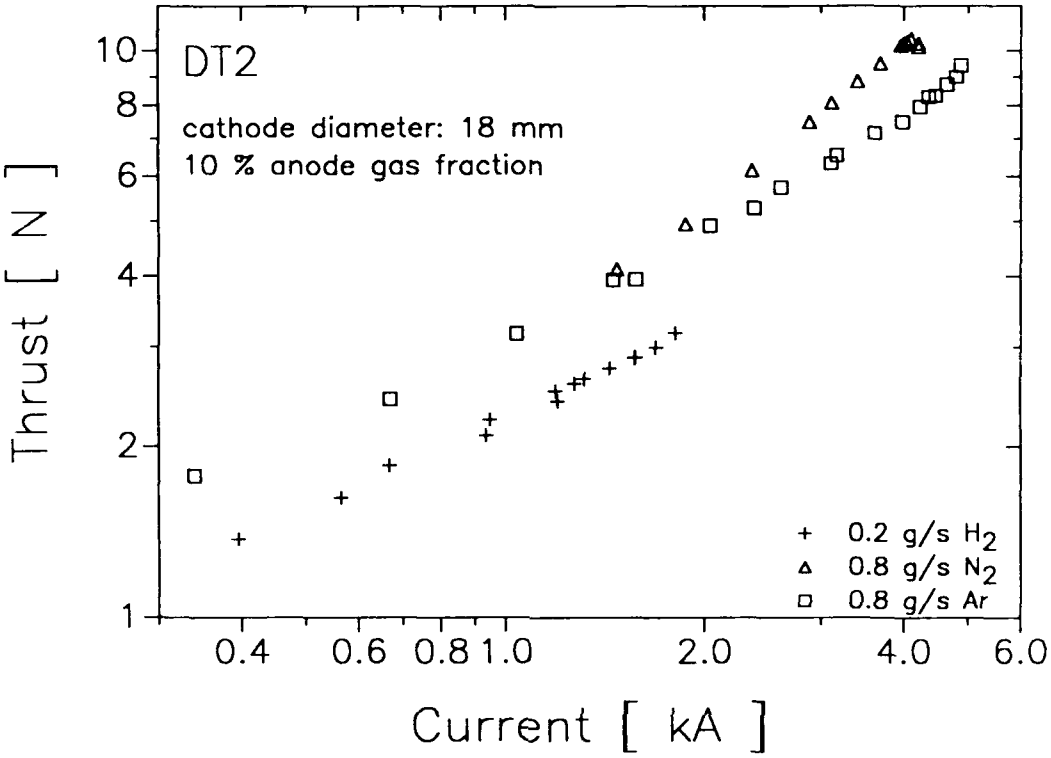

Fig. 2.1.5: Thrust - current dependence of the DT2-Thruster running with various gases

The comparison of the thrust for nitrogen and argon as propellant with the same total mass flow rates (Fig. 2.1.5) shows a better performance for nitrogen. The decrease of the thrust for nitrogen at high current values is caused by the plasma instabilities.

Figure 2.1.6 shows the thrust efficiency dependence on the specific impulse for the different propellants. The thrust efficiency is calculated as

$$\eta_T = \frac{T^2}{2\dot{m}UI}$$

where T is the thrust, U and I are the voltage and current respectively and $\dot{m}$ is the total mass flow rate of the various gases.

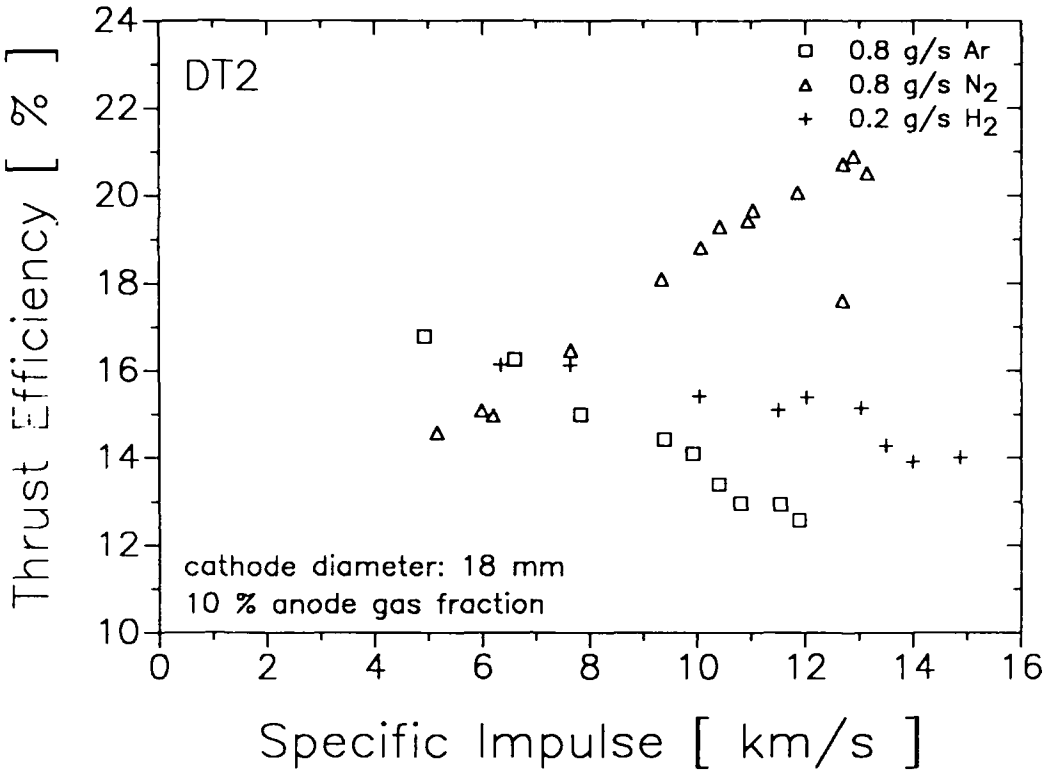

Fig. 2.1.6: Thrust efficiency - specific impulse of the DT2-Thruster

For hydrogen and argon, the thrust efficiency decreases with increasing specific impulses, in contrast to dependence for nitrogen. Here the thrust efficiency increases until the onset-point is reached. The highest specific impulse values are reached with hydrogen while the best efficiency can be reached with nitrogen.

In the next diagrams (Fig. 2.1.7 - Fig. 2.1.9) the heat balance of the DT2-thruster with various propellants will be compared. For the investigation of the thermal losses in the thruster, the water flow rates and also the temperatures of all in- and outflowing water are measured continuously by thermocouples during the tests.

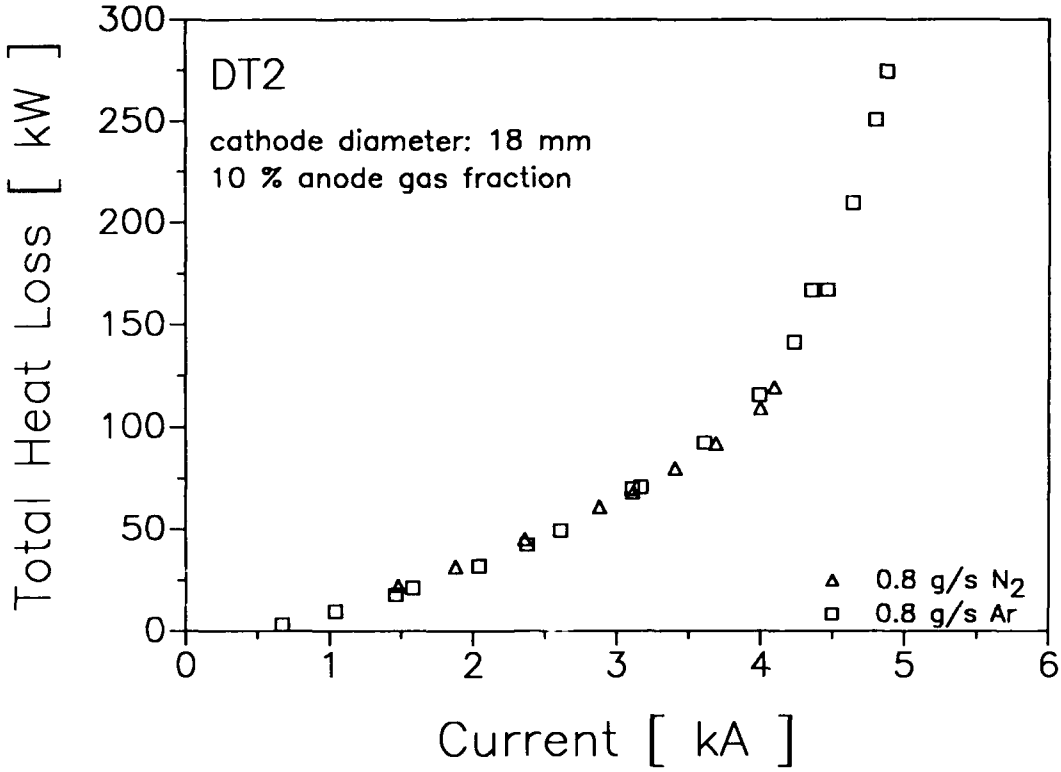

Fig. 2.1.7: Total heat losses vs. current for various gases

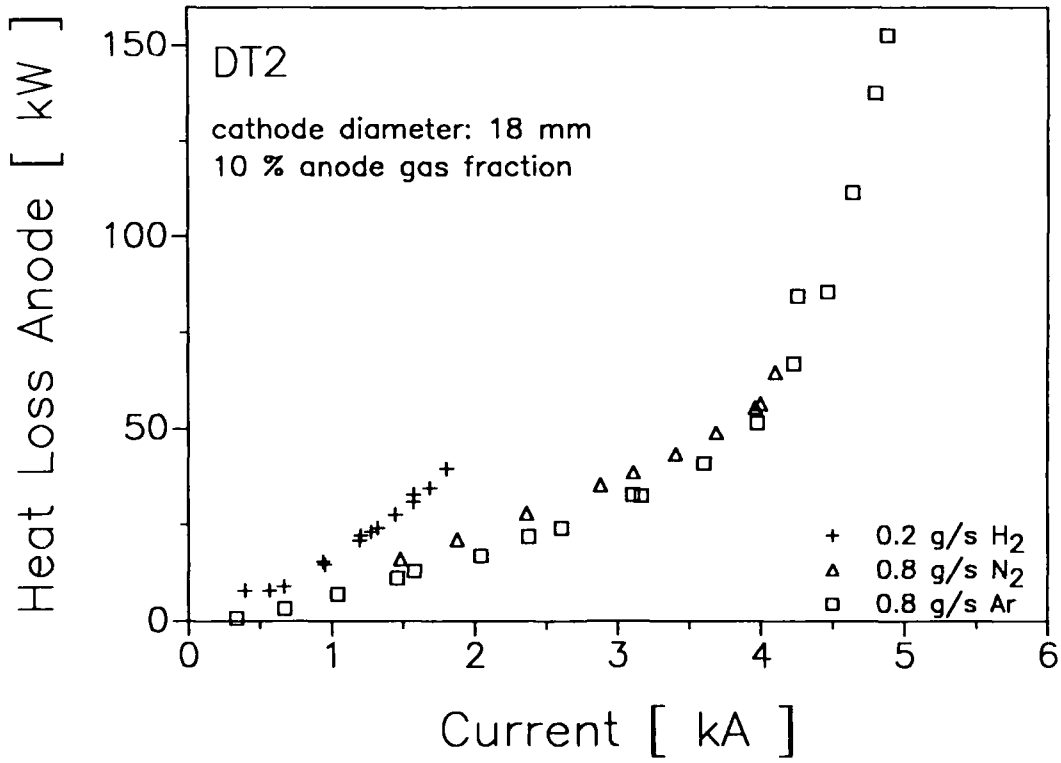

Fig. 2.1.8: Heat loss anode vs. current for various gases

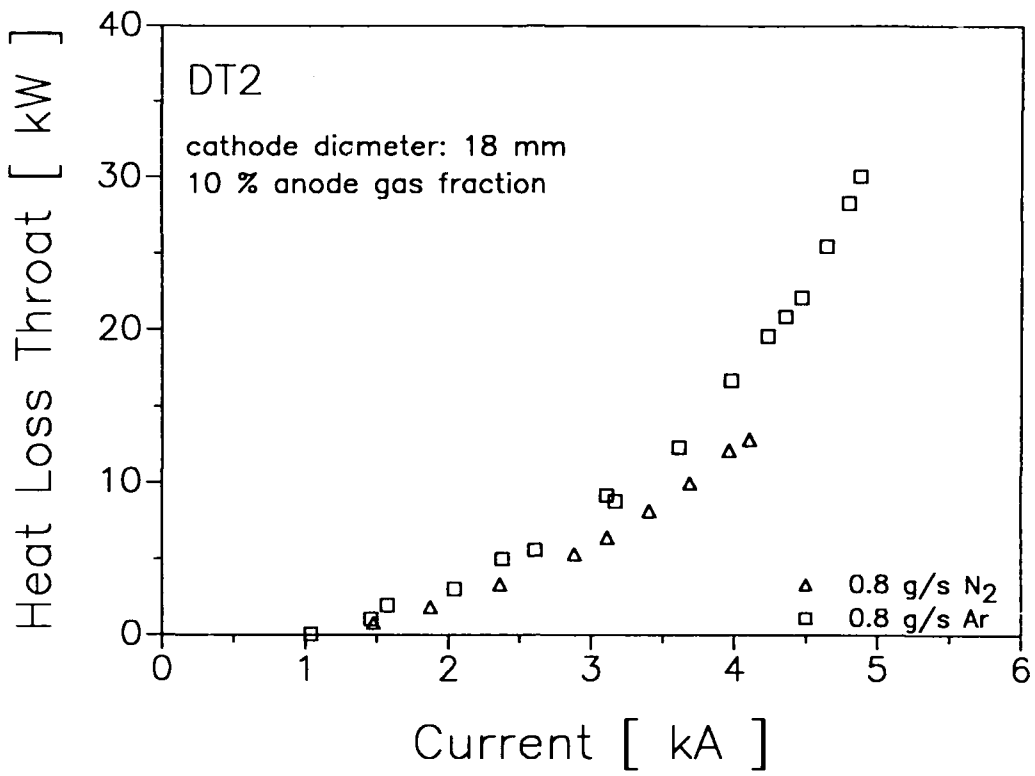

Fig. 2.1.9: Heat loss segment 4 (throat) vs. current for various gases

The total heat losses for argon and nitrogen show the same current dependence; they increase strongly with the current. The most part of the thermal losses occurs at the anode, Fig. 2.1.8, it amounts to 50% and 70 % of the total losses. While the anode heat losses for argon are higher than for nitrogen, the throat heat losses show the inverse behavior. The steep rise of the heat flux into the anode at current higher than the onset point is typical for the onset, investigated some years ago by Hügel [5].

In Figure 2.1.8 the anode heat losses for hydrogen are also registered, which are higher than for the other propellants.

The heat flux into segment 4, the inner part of the nozzle throat is depicted in Fig. 2.1.9. It should be noticed that the total constrictor length (and hence the constrictor area) is twice as long. The steeper rise of the heat flux with argon could probably be explained by the higher atomic mass of argon, which leads to a quicker expansion of the arc core in the constrictor [6]. In Figure 2.1.10 the thermal efficiency is plotted against the current. While for nitrogen the thermal efficiency decreases only slowly to about 65%, for argon it decreases continuously below 40%.

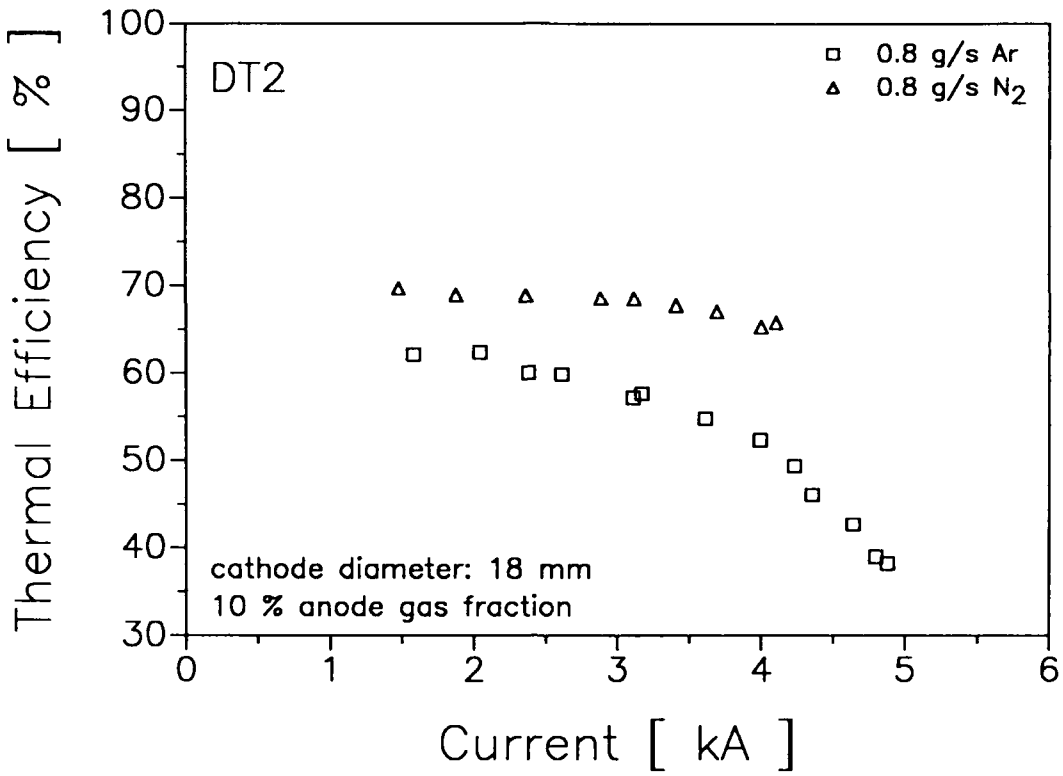

Fig. 2.1.10: Thermal efficiency vs. current for various gases

From the heat balance at the anode the anode voltage drop can be determined approximately. The total anode heat loss $\dot{Q}_A$ can be split up in the following components, neglecting radiation:

$$\dot{Q}_A = (U_A + 5/2\, k\, T_e + \Phi + U_{conv}) \cdot I$$

Here U_A is the anode drop voltage, T_e the electron temperature near the anode, Φ the entry energy of the electrons, U_{conv} the convective heat transfer, and I the total current input. For the following results of the anode fall voltage we have made the following assumptions:

- for the electron temperature 15000 K was taken, which is a good estimation, extrapolated from probe measurements in the immediate vicinity of the anode
- for the work function of the electron into copper 4.62 V
- the convective heat transfer at the anode was determined approximately from the heat loss of the neighboring neutral segment according the following equation:

$$U_{conv,An} = U_{conv,R1} \cdot A_{An} / A_{R1}$$

Here A_{An} and A_{R1} are the surfaces of the anode and the first segment

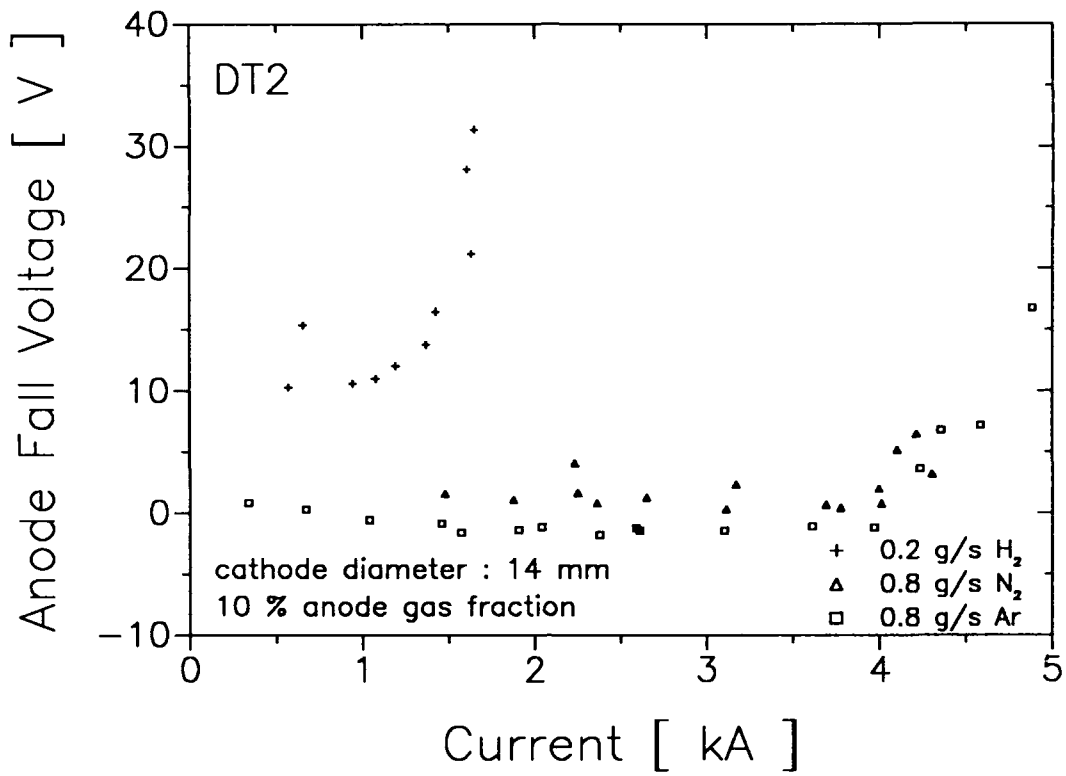

Fig. 2.1.11: Anode fall voltage vs. current for various gases

Figure 2.1.11 shows the anode fall voltage as a function of the current the various gases. In the operation range of the thruster below the onset point the fall voltage is relativly low, normally lower than 2 V for Ar and N_2, but it increases very fast after passing the onset point. For hydrogen the minimum anode fall voltage is about 10 V higher than the low continuum of the other gases.

In Fig. 2.1.12 to 2.1.14, photos of the plasma jet of the DT2 for argon and nitrogen are shown.

Fig. 2.1.12 shows the argon jet side-on, mass flow rate 0.8 g/s, I = 4500 A. A shock structure can clearly be seen, emerging from inside the nozzle. Fig. 2.1.13 shows the thruster end-on. The nozzle throat and cathode region are very bright and over-radiate the geometric contours. Also the anode region is brighter than the neutral segments.

Fig. 2.1.14 shows the nitrogen jet side-on $\dot{m}$ = 0.8 g/s, I = 4000 A. The jet is much brighter than with argon and no Mach structures can be seen. The jet looks more unsteady than the argon jet, which appears very calm and smooth.

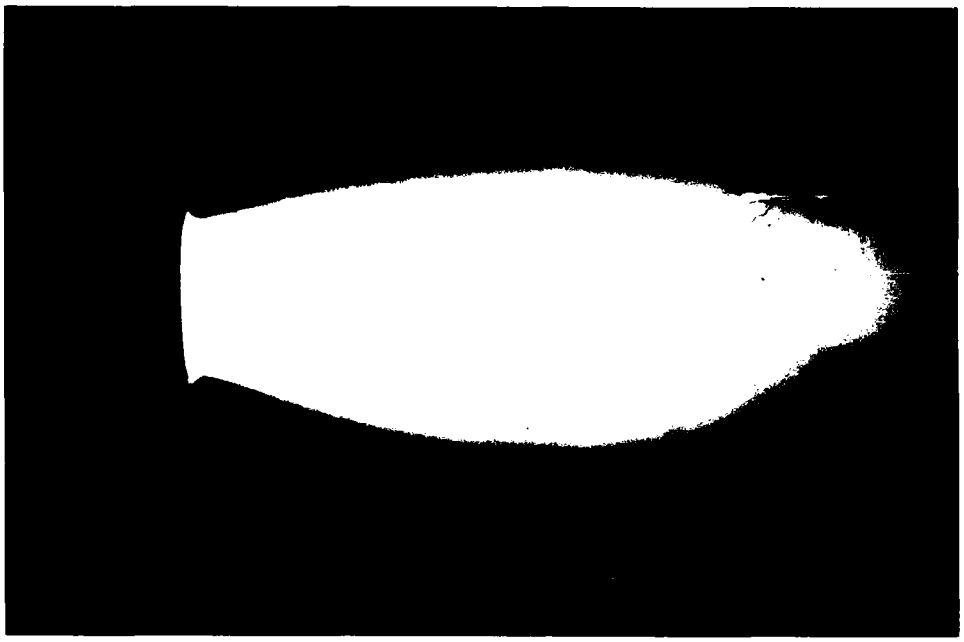

Fig. 2.1.12: Argon plasma jet, side-on

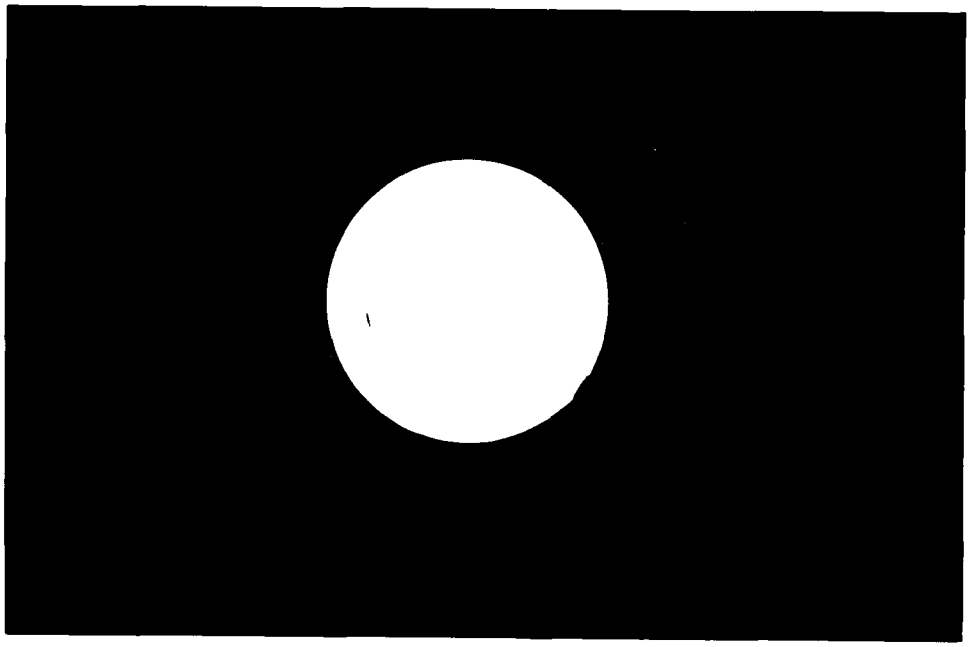

Fig. 2.1.13: Argon plasma jet, end-on

Fig. 2.1.14: Nitrogen plasma jet, side-on

2.1.2.2 Variation of the cathode position and diameter

In the following chapter the influence of the cathode position and the cathode diameter on the operating conditions of the DT2-thruster are illustrated.

Here the results of varying the position of a cathode with small diameter are presented.

Based on the original, unchanged DT2-thruster, the cathode position relative to the anode exit plane was varied between 79 mm and 93 mm. The cathode diameter was 14 mm, the gas propellant was argon with a total mass flow rate of 0.8 g/s, 10% of which was injected at the anode. For each cathode position two tests were carried out at short intervals, so that the reproducibility of the results could be verified.

Figure 2.1.15 shows the current dependence of the voltage at the different cathode positions.

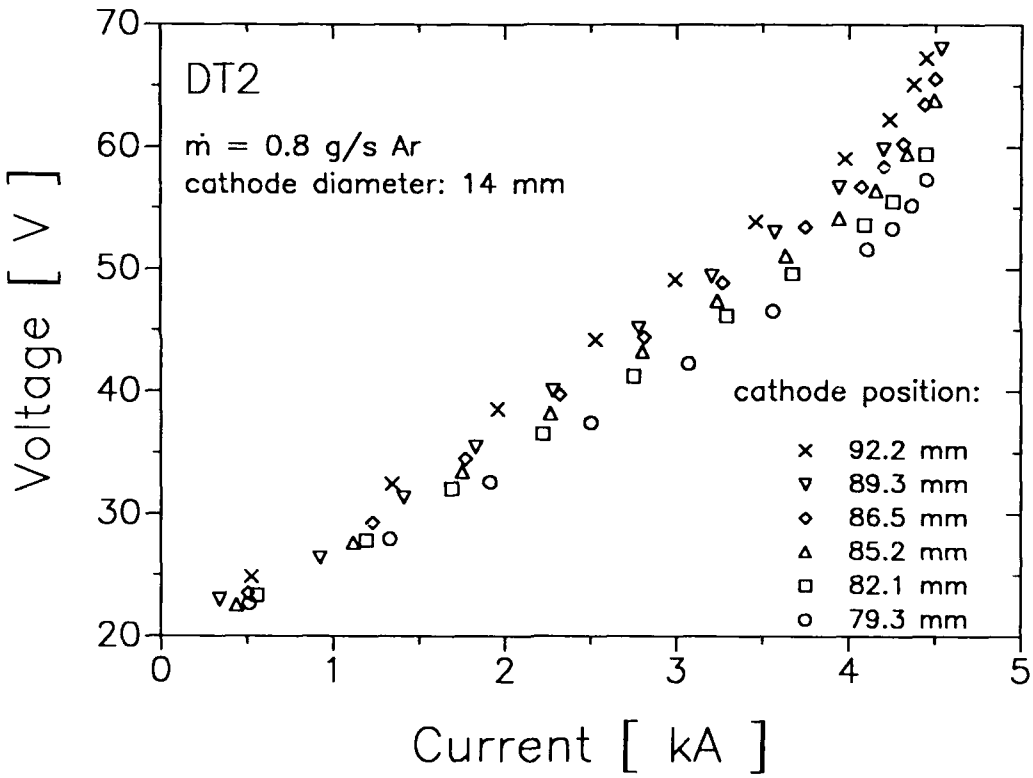

Fig. 2.1.15: Voltage vs. current at various cathode positions

All curves show a strong variation in slope at about 4400 A, not depending on the cathode position. At constant current levels, the arc voltage increases with the cathode position. Figure 2.1.16 presents the arc voltage as a function of the cathode position at three current levels. The curves are relatively linear and parallel to each other, which suggests an almost constant electric field strength in the arc chamber.

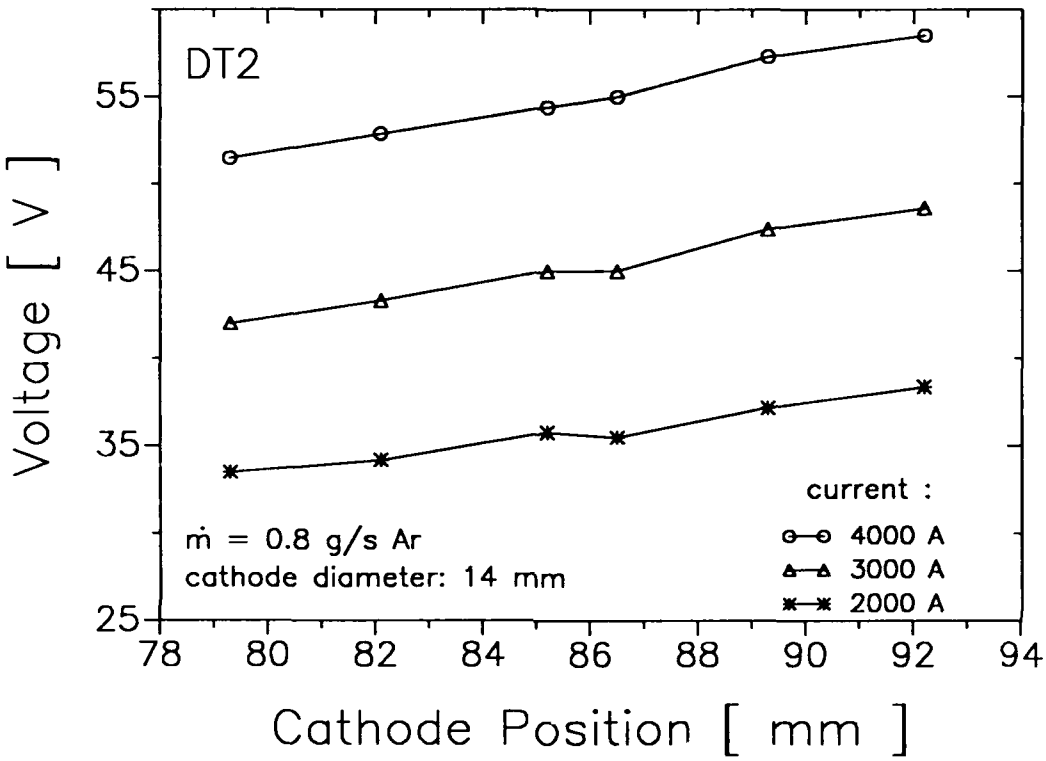

Fig. 2.1.16: Voltage vs. cathode position at various current levels

By increasing the distance from minimum to maximum, the arc voltage rises by ca. 7V. Assuming a distance variance of 12.9 mm, an electric field strength of ca. 0.5 V/mm is obtained.

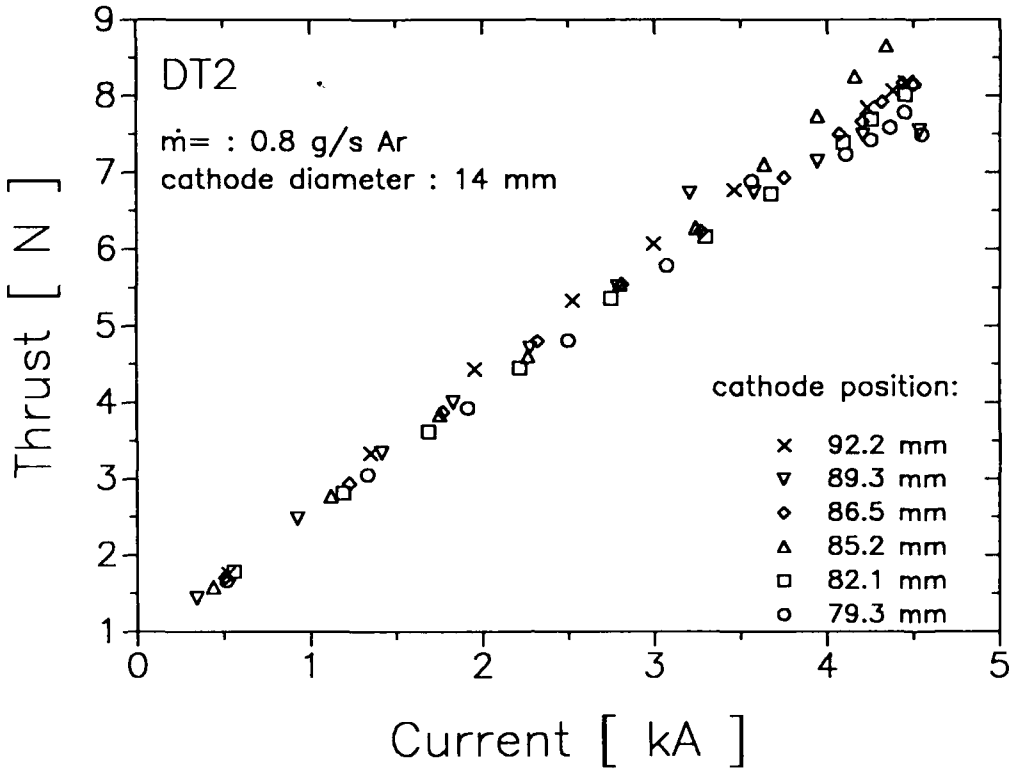

Fig. 2.1.17: Thrust vs. current for various cathode positions

The thrust against current plot, Fig.2.1.17, shows less distinct dispersions than those of the voltage lines. Nevertheless it is evident that the minimum distance leads to a lower thrust than the maximum.

Like the voltage, also the thrust has the tendency to rise slowly with the increasing cathode position, Fig.2.1.18. The thrust efficiency reaches a maximum at a cathode position of 85.2 mm, as can be seen in Figure 2.1.19. At high specific impulses the thrust efficiency decreases rapidly because of the voltage rise. The upper limit of the specific impulse was about 1100 s.

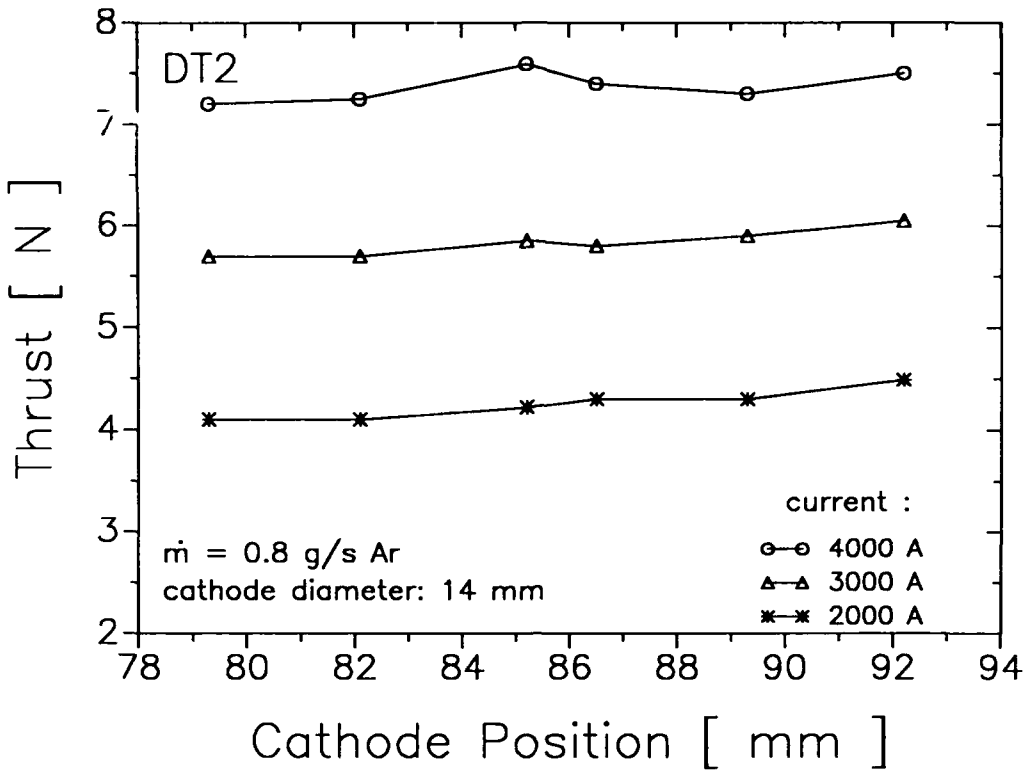

Fig. 2.1.18: Thrust vs. cathode position at various current levels

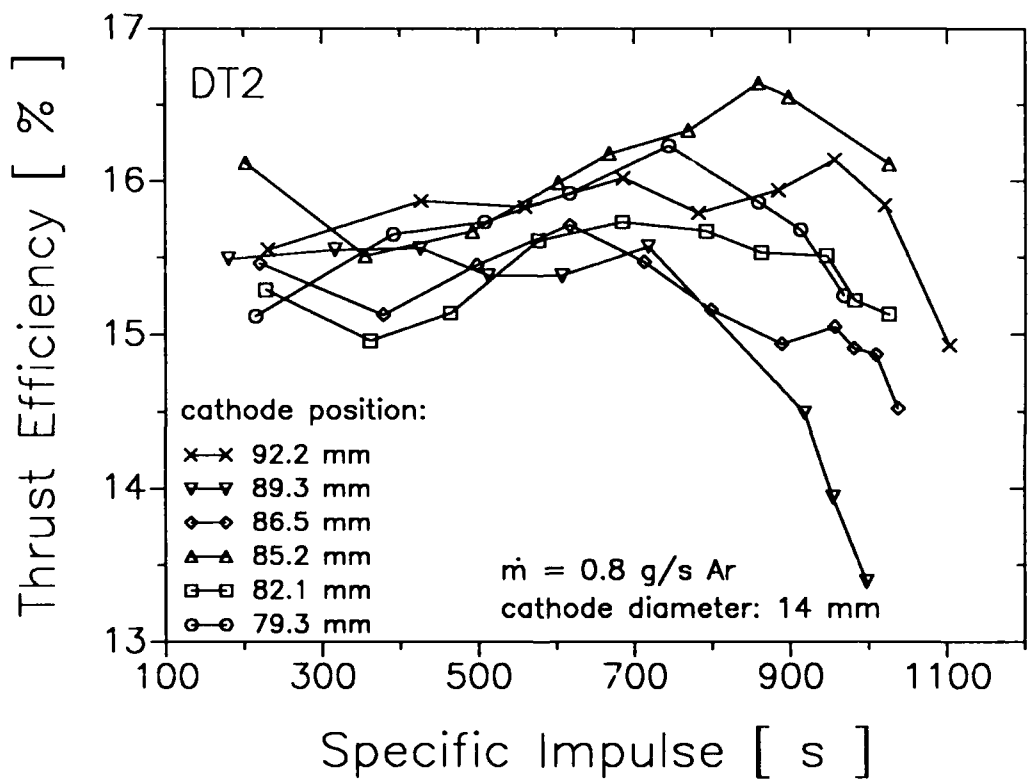

Fig. 2.1.19: Thrust efficiency vs. specific impulse at various cathode positions

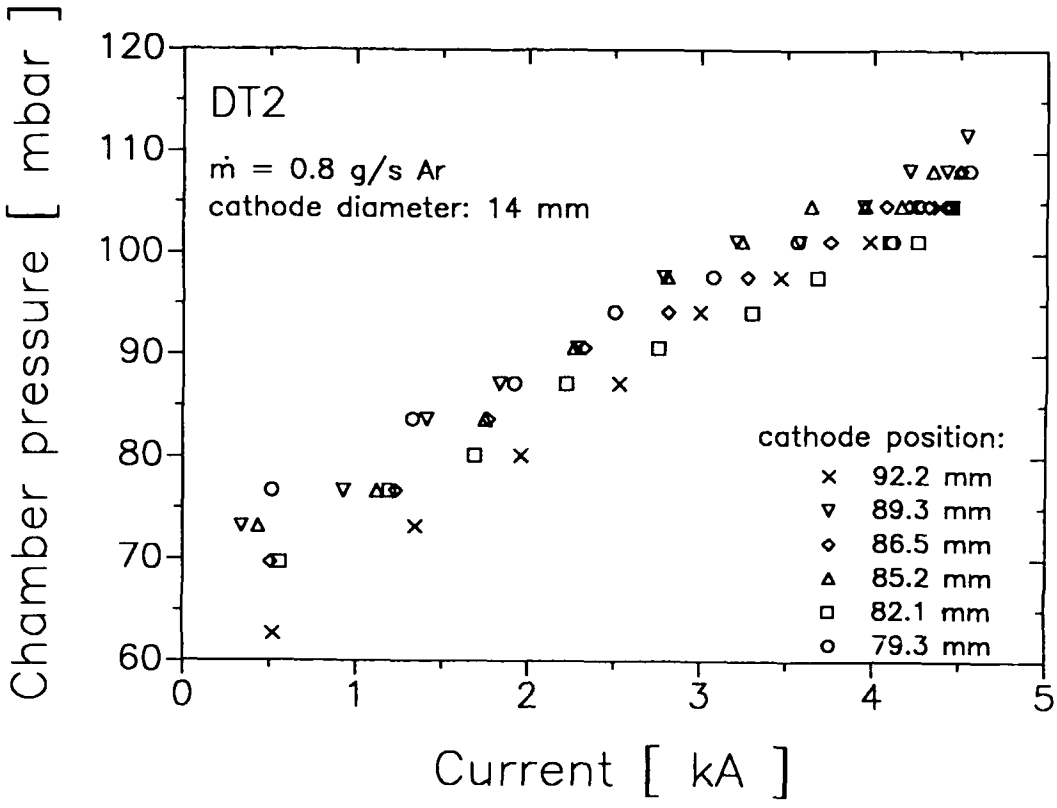

Fig. 2.1.20: Chamber pressure vs. current at various cathode positions

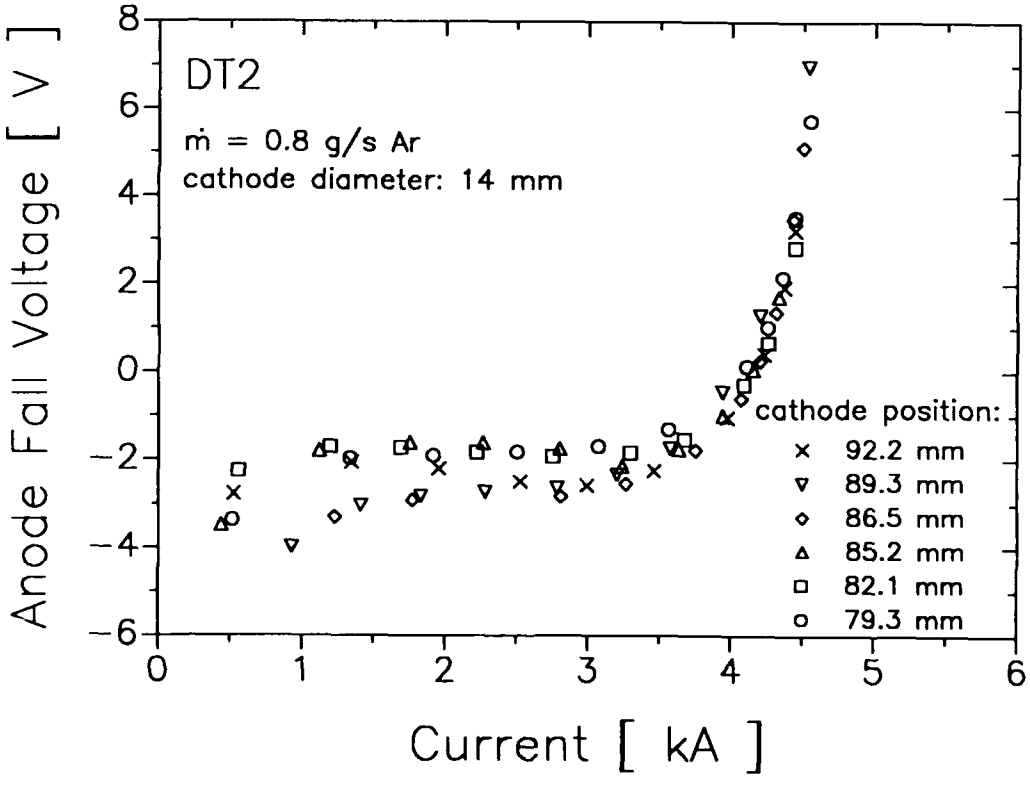

Fig. 2.1.21: Anode fall voltage vs. current at various cathode positions

Figure 2.1.20 shows the current dependence of the arc chamber pressure. The chamber pressure increases with the rising current. At constant current levels, especially at lower current values, the pressure in the arc chamber decreases with increasing cathode positions, but no clear tendency could be made out.

The anode fall voltages for all cathode positions are within the range of -1 V to -3 V for current levels below 4 kA. Reaching the unstable running mode above this current value, the anode fall voltage rises abruptly (Fig. 2.1.21). The cathode position does not influence the anode fall, so the increase in voltage (Fig.2.1.15) is mainly due to the longer current path.

Now the heat balance and the dependence from the cathode positions will be investigated in detail.

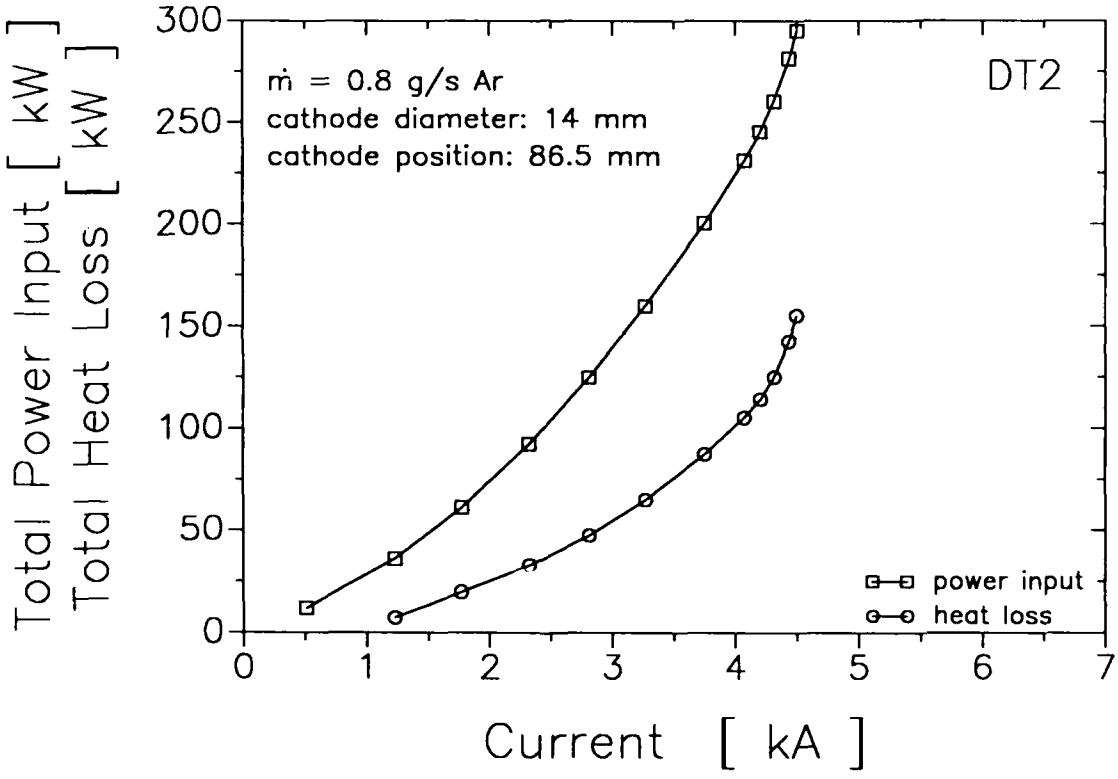

Fig. 2.1.22: Comparison of power input and total heat loss

Figure 2.1.22 shows that between 40% and 50% of the total power input will be eliminated as heat loss in the thruster. At high current values a strong rise in the total heat loss can be observed, resulting mainly from the increasing heat losses at the anode (Fig. 2.1.24), which is independent of the cathode position.

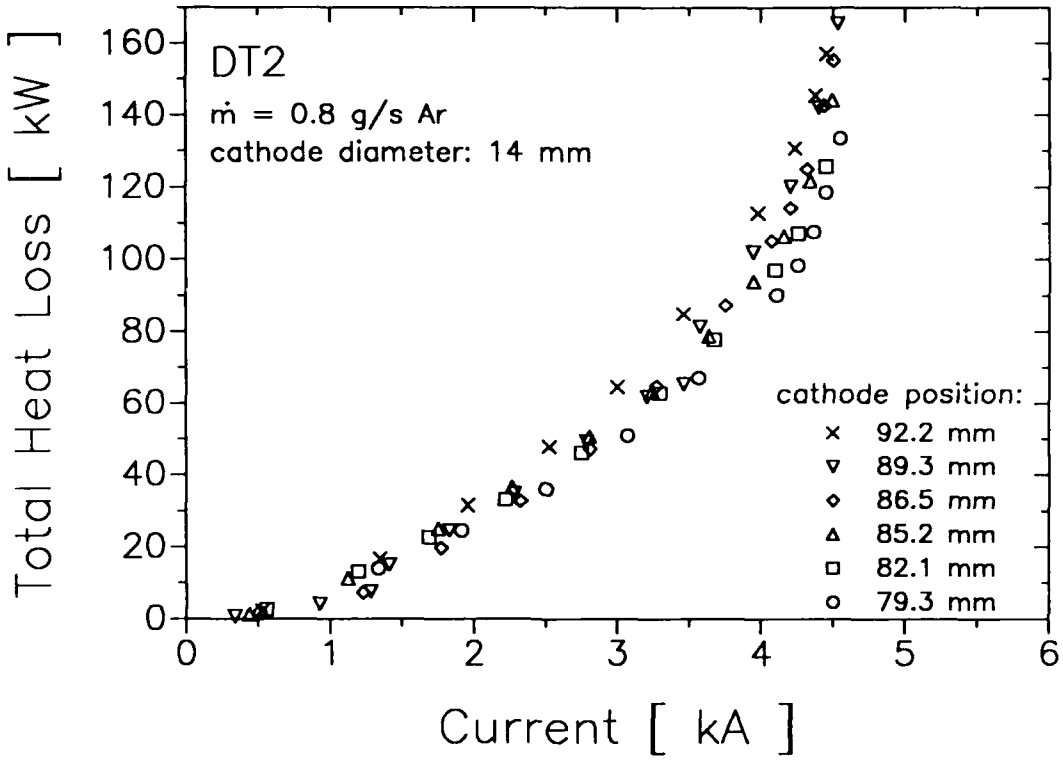

Fig. 2.1.23: Total heat loss vs. current at various cathode positions

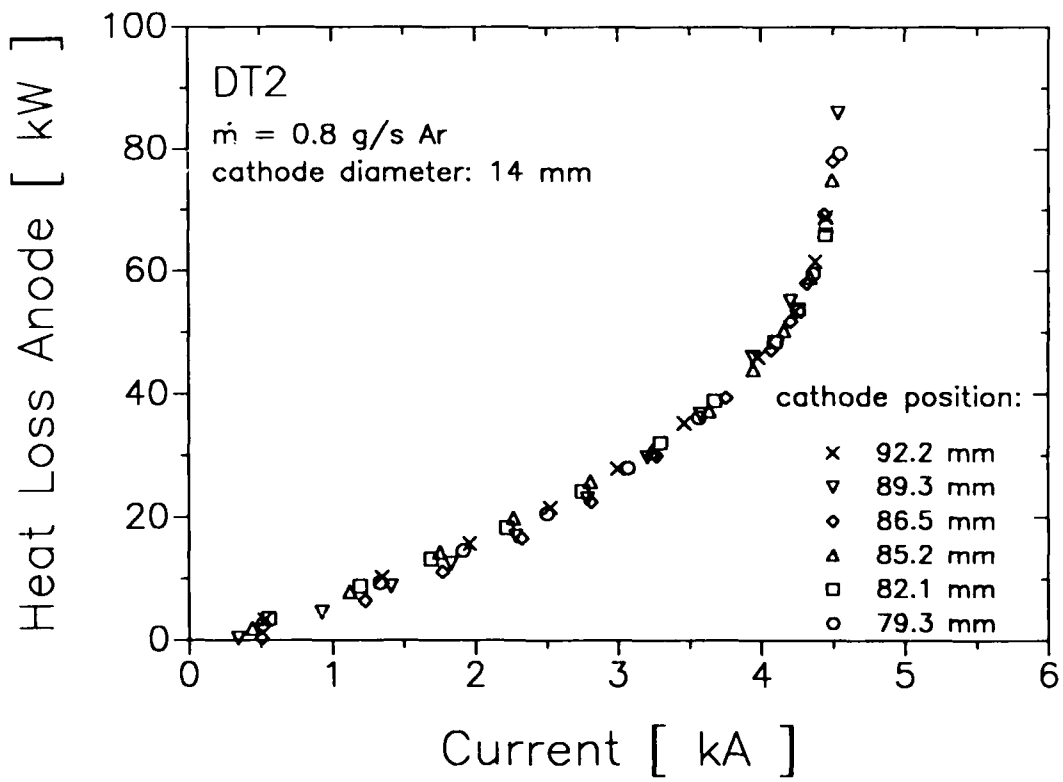

Fig. 2.1.24: Anode heat loss vs. current at various cathode positions

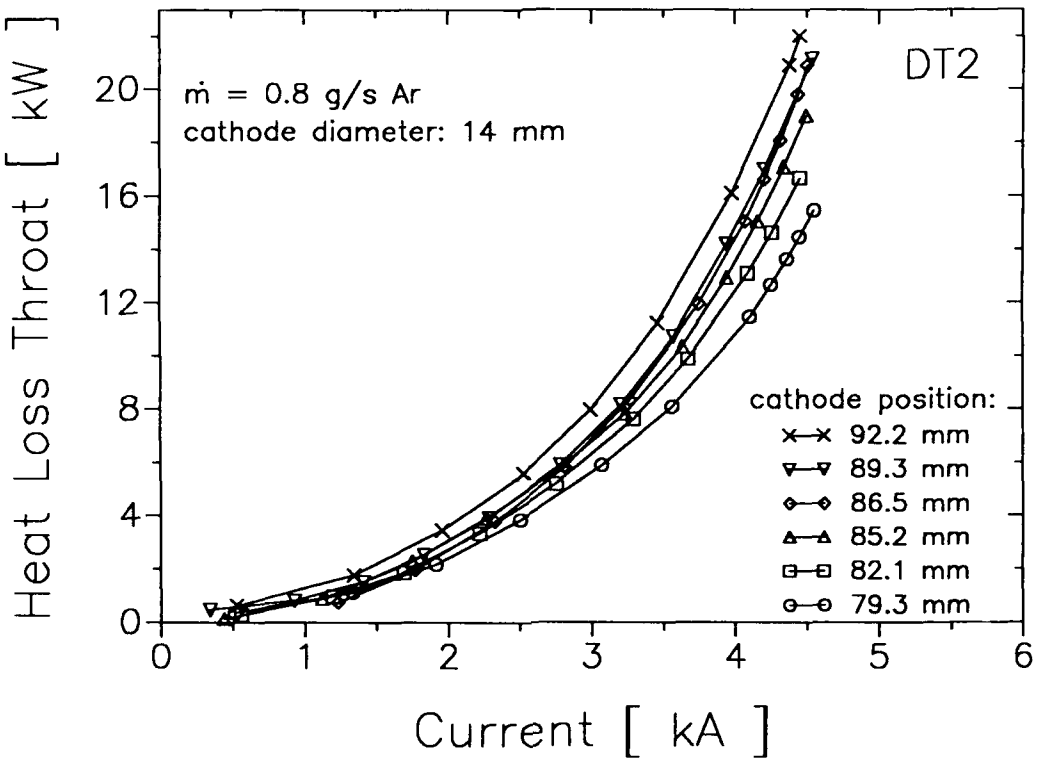

Fig. 2.1.25: Throat heat loss vs. current at various cathode positions

The total heat loss of the thruster increases with the cathode position, Fig.2.1.23. This is an effect of the heat losses at the throat segment (Fig. 2.1.25). At cathode positions further back, the arc chamber pressure will be lower, so that the arc can expand more. Therefore the thermal stress of the segments, building throat and arc chamber, increases. This can also be seen in Figures 2.1.26 - 29. Here the heat loss of the particular segments at the minimum, medium and maximum cathode positions are plotted. Especially conspicuous is the strong rise of the heat loss of the arc chamber at the maximal cathode position.

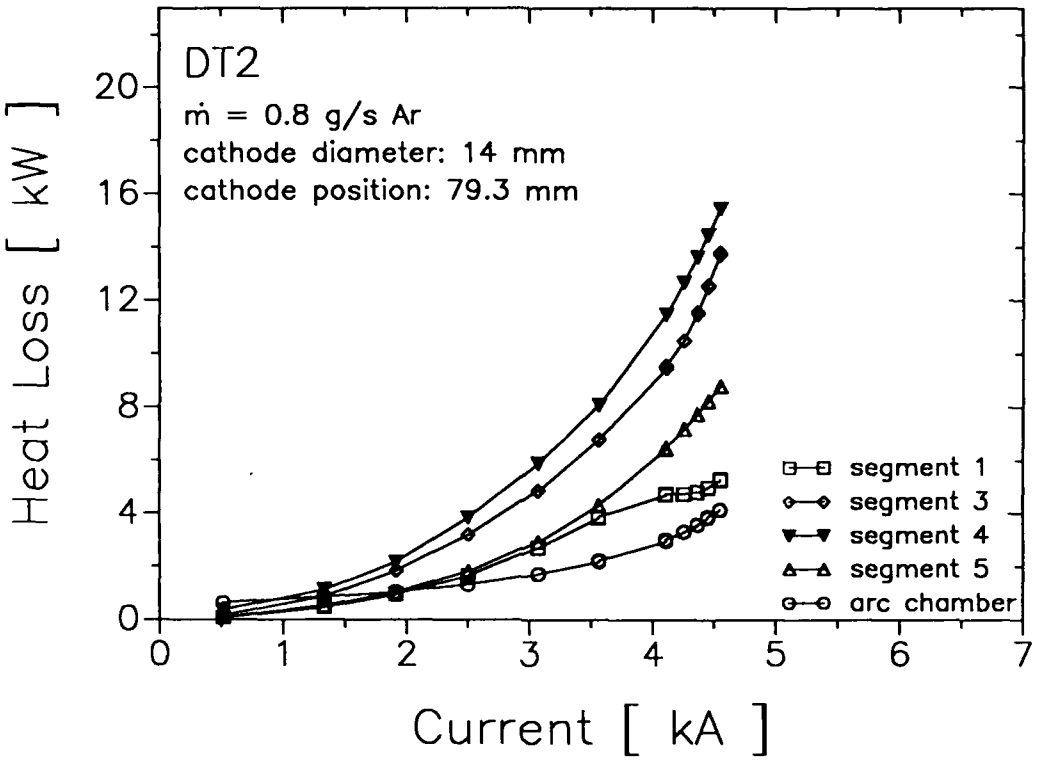

Fig. 2.1.26: Segment heat loss vs. current at 79.3 mm cathode position

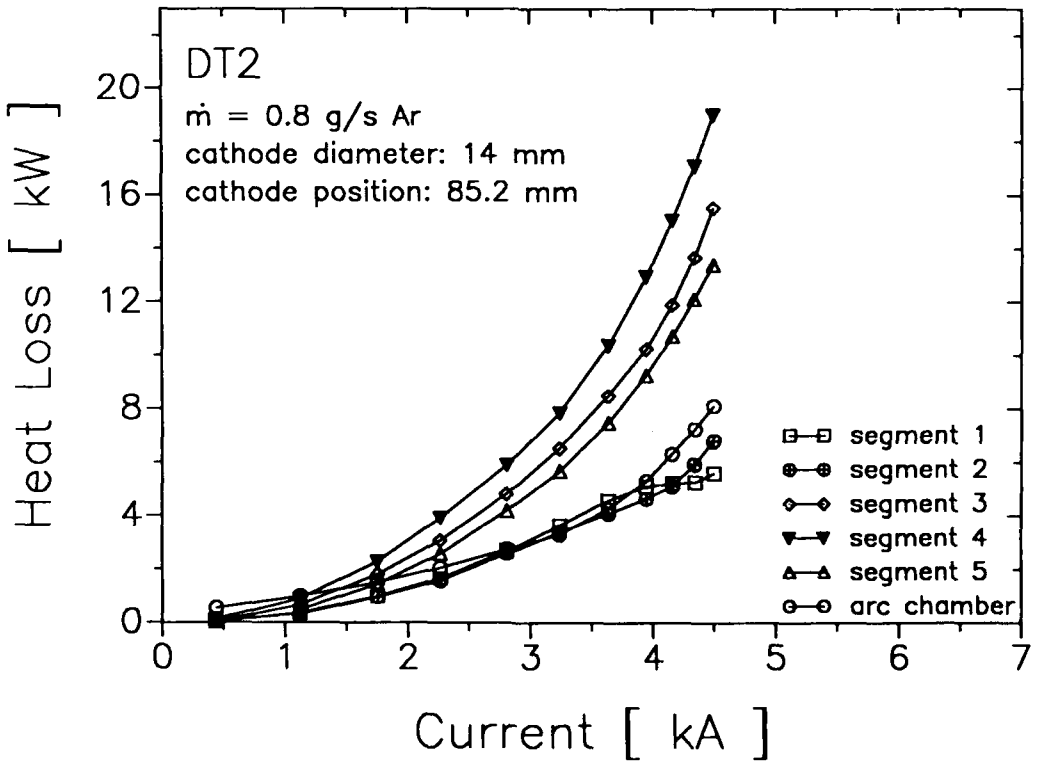

Fig. 2.1.27: Segment heat loss vs. current at 85.2 mm cathode position

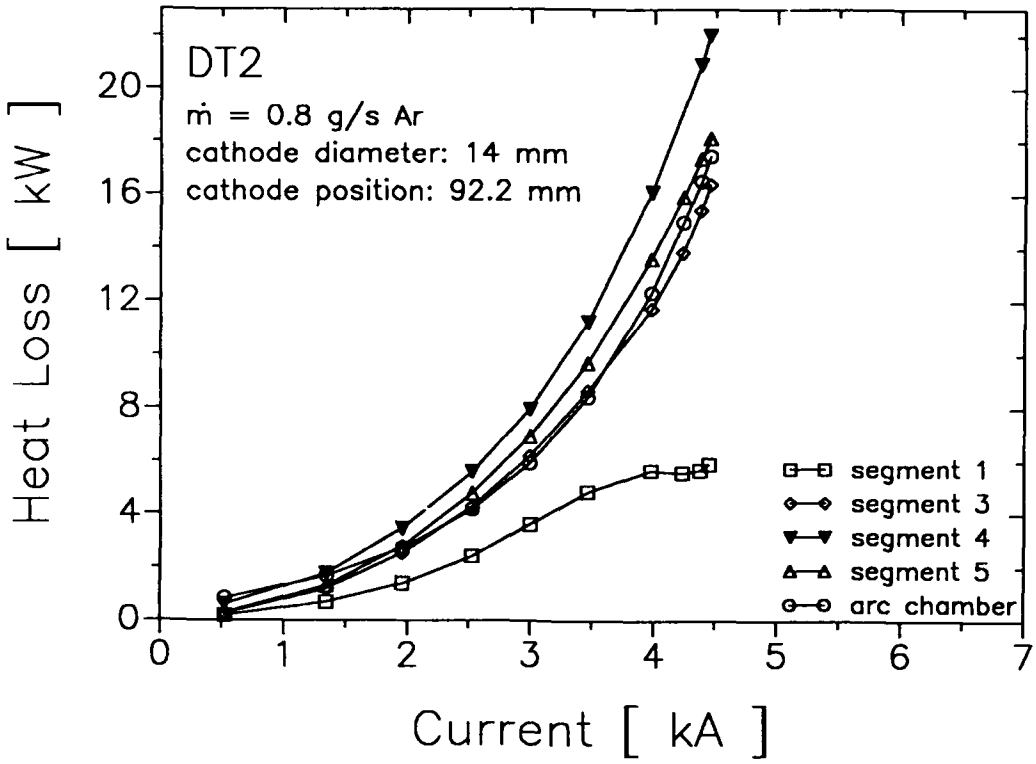

Fig. 2.1.28: Segment heat loss vs. current at 92.2 mm cathode position

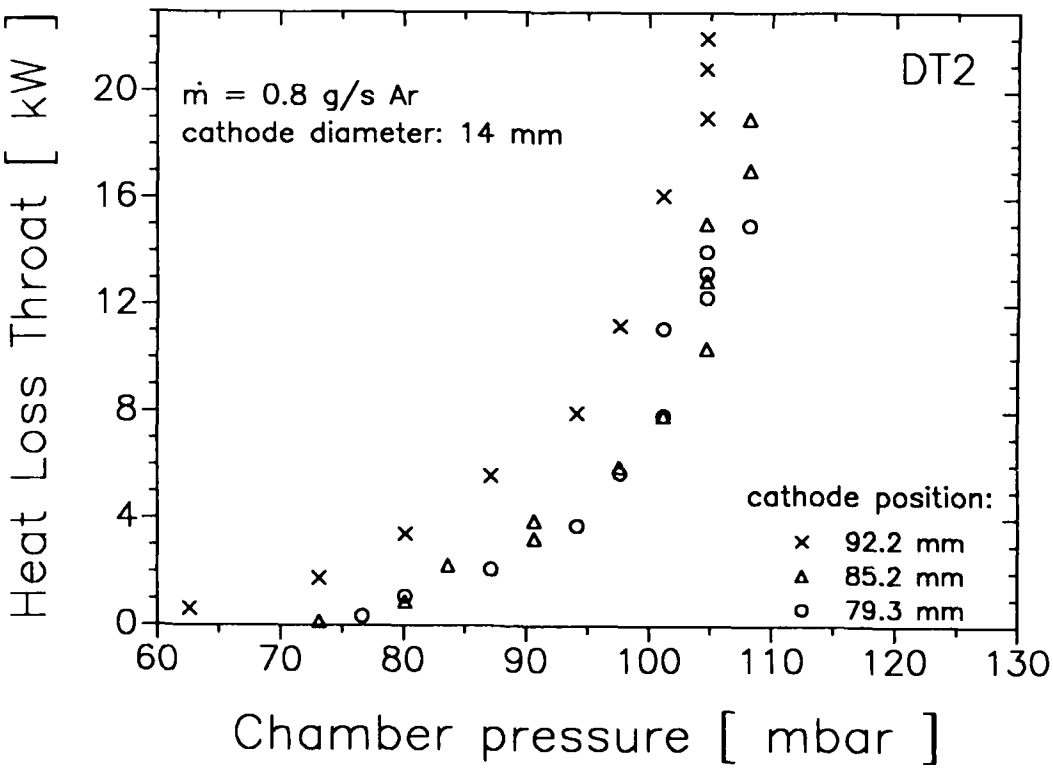

Fig. 2.1.29: Throat heat loss vs. chamber pressure at various cathode positions

2.1.2.3 Influence of the mass flow rate

Since the previous tests do not indicate a clear advantage for a particular cathode position, the original position of Sk = 85 mm was taken for this test series. In this test cycle the mass flow rates were increased step by step from 0.4 g/s to 2.8 g/s argon, 10% of it injected as anode gas.

Figure 2.1.30 shows the voltage vs. current curves for the different mass flow rates.

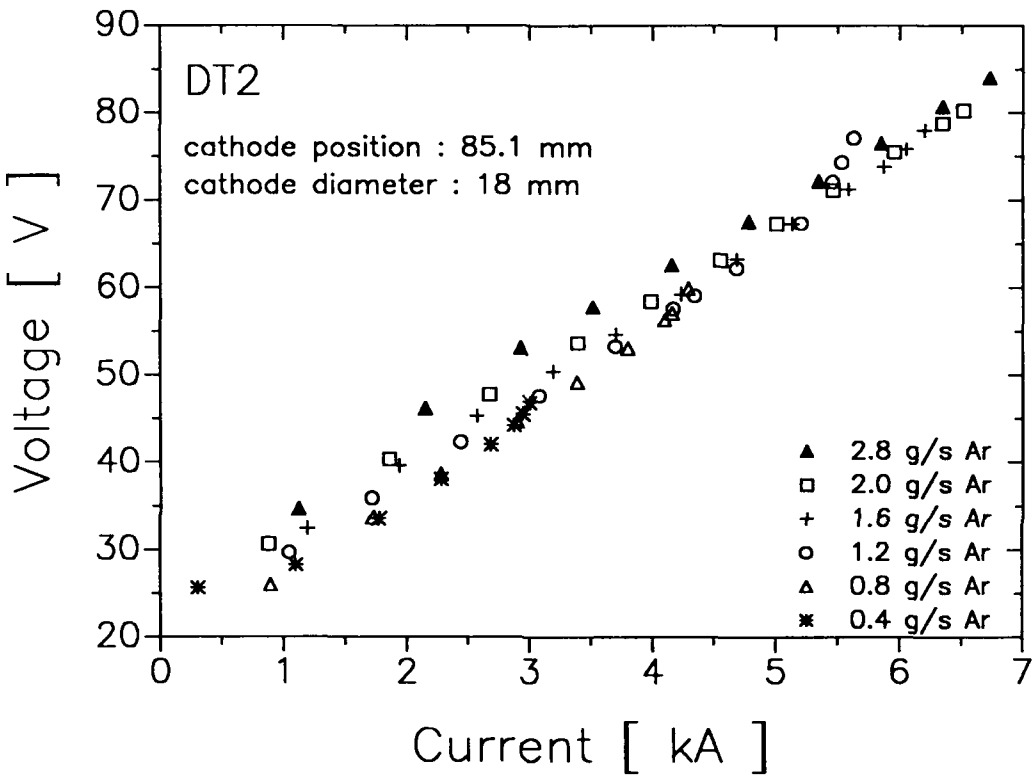

Fig 2.1.30: Voltage vs. current for various mass flow rates

The voltage at constant current levels and also the current value where the voltage rise starts increase with the mass flow rate.

With higher mass flow rates the current dependence of the thrust will be intensified (Fig 2.1.31). The higher thrust values also improve the thrust efficiency. The tendency is quite clear: from a very low efficiency (around 10%) obtained with 0.4 g/s, the values increase to nearly 22% with a 2.8 g/s argon mass flow rate (Fig. 2.1.32). For all mass flow rates an upper limit of 1100 s for the specific impulse could not be exceeded.

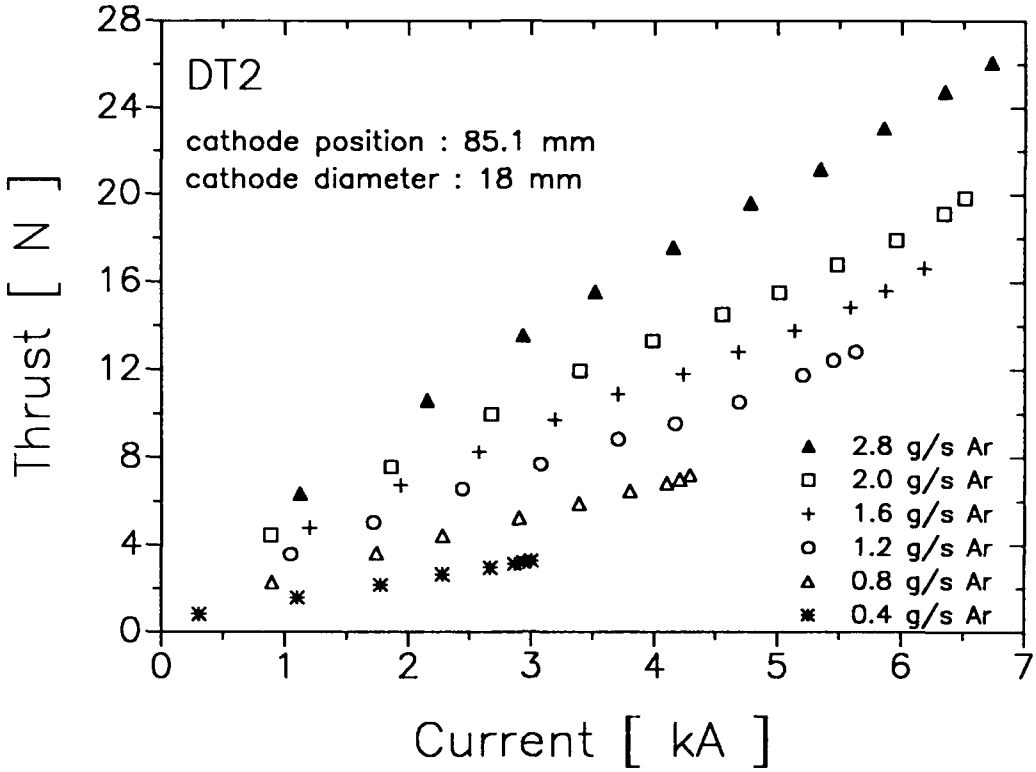

Fig. 2.1.31: Thrust vs. current at various mass flow rates

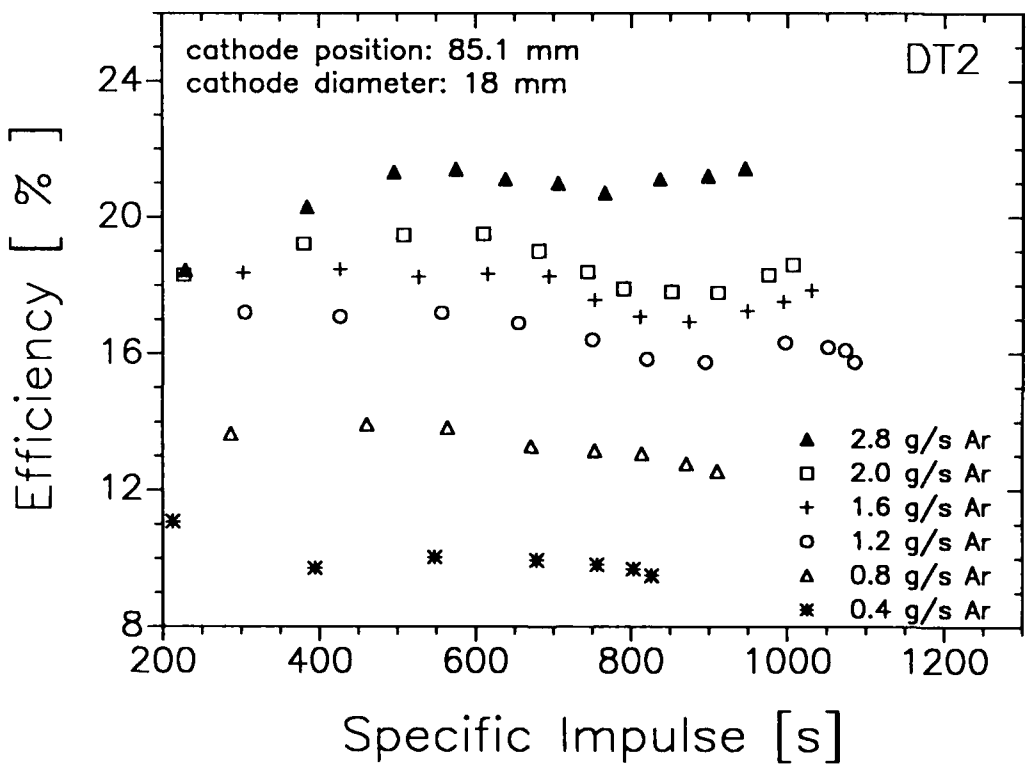

Fig. 2.1.32: Thrust efficiency vs. specific impulse for various mass flow rates

At low mass flow rates the current level with the nozzle type DT thrusters is limited by the onset phenomenon (see page 34), at higher mass flow rates by thermal reasons. Figure 2.1.33 shows clearly that although the thermal flux into the throat segment decreases with the mass flow, at higher current levels (6000 A to 7000 A) it approaches 5 kW/cm^2 which we set as the upper limit for safe tests.

Figure 2.1.34 shows the arc chamber pressure as a function of the current for the different mass flow rates. Both the absolut value of the pressure and the current dependence increase with the mass flow rate.

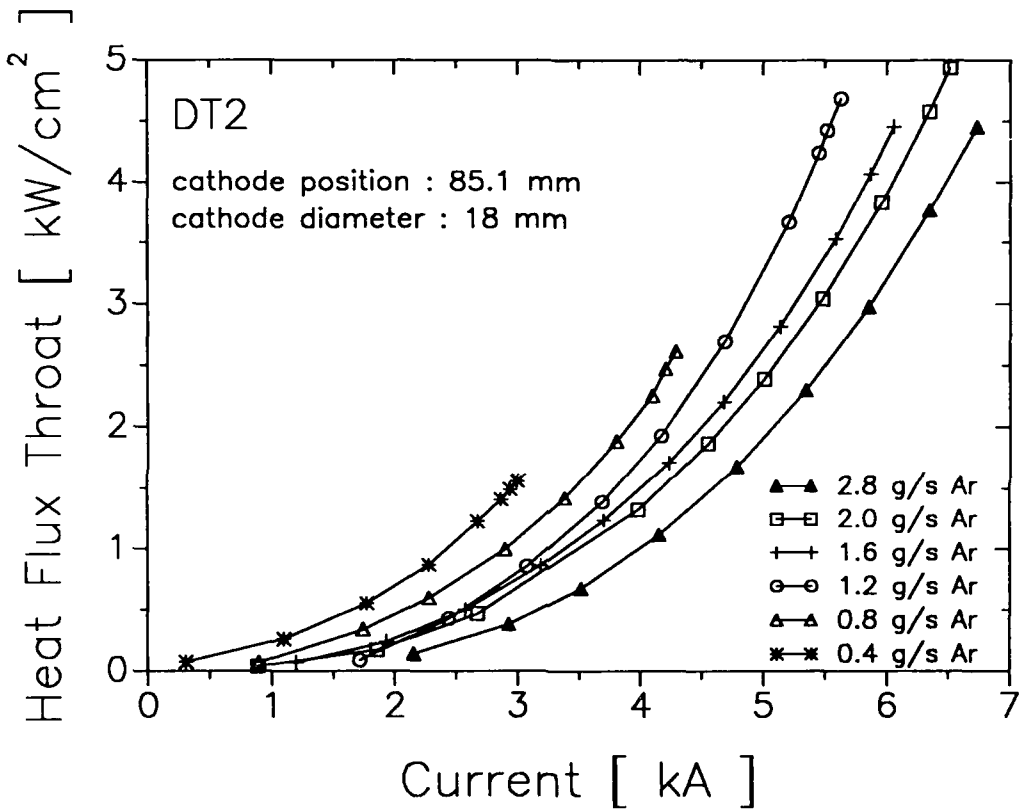

Fig. 2.1.33: Throat heat flux vs. current for various mass flow rates

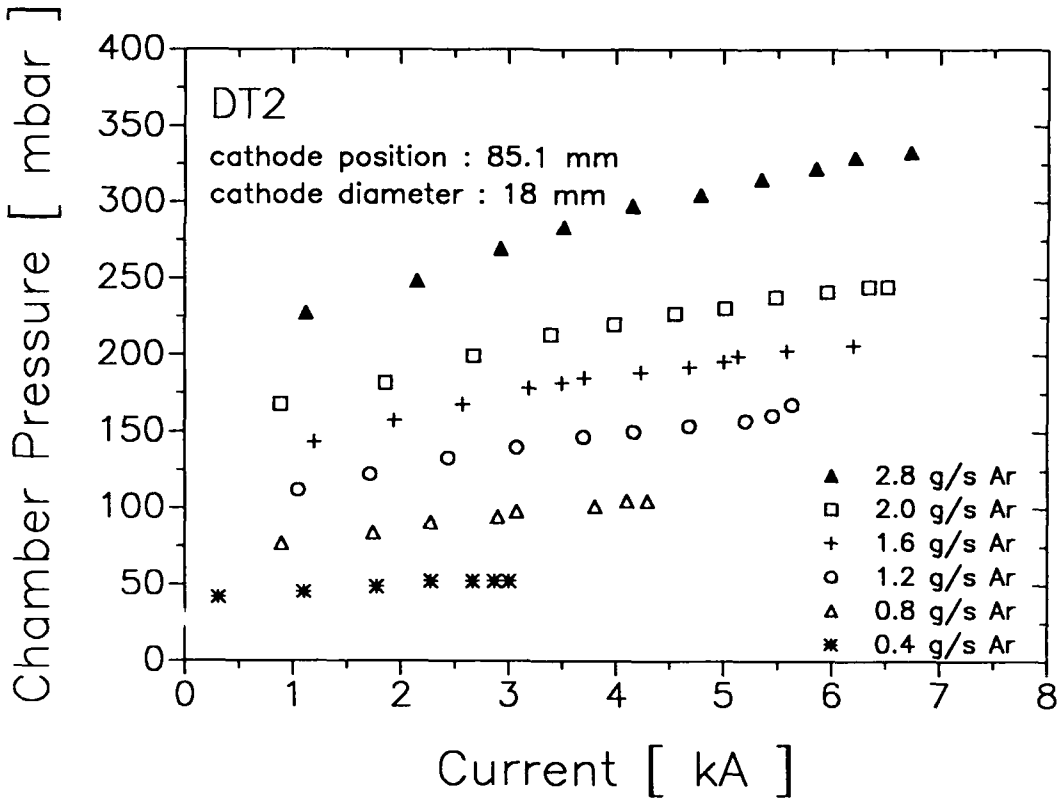

Fig. 2.1.34: Chamber pressure vs. current for various mass flow rates

2.1.2.4 Variations of the cathode diameter

Figure 2.1.35 shows the voltage versus current curve for two cathode diameters.

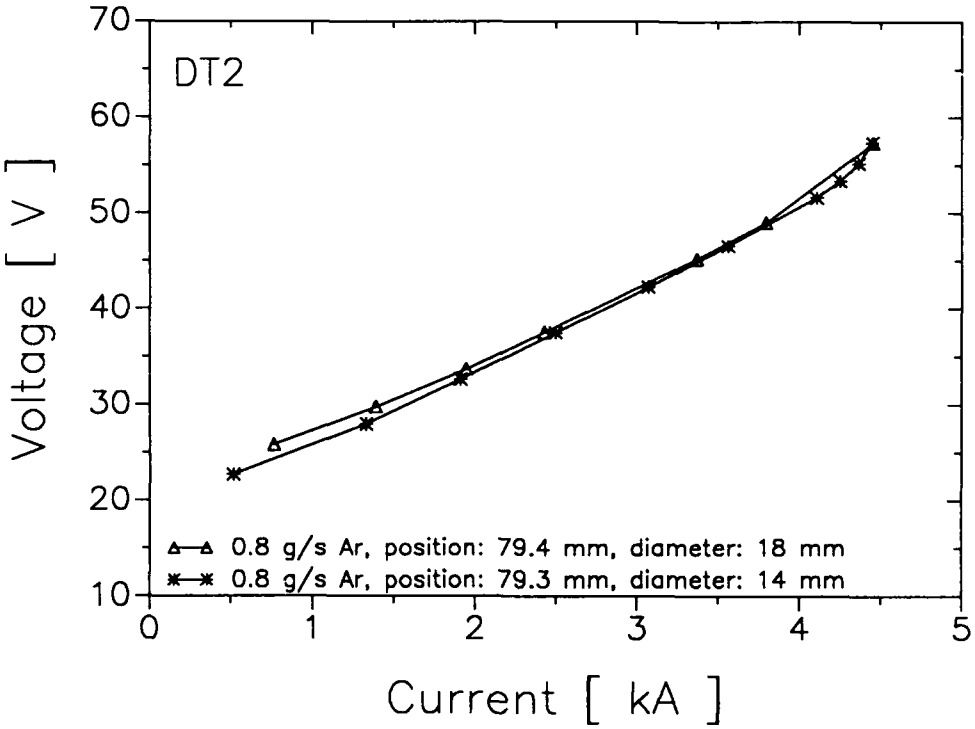

Fig. 2.1.35: Voltage vs. current at different parameters

A greater cathode diameter, 18 mm compared to 14 mm, results in a higher voltage at constant current levels. At higher currents, this difference disappears.

The cathode diameter has no significant influence on the thrust (Fig. 2.1.36). The thrust efficiency of the DT2-thruster with a smaller cathode diameter will be between 1% and 2% better than the thruster with 18 mm cathode diameter, Fig.2.1.37.

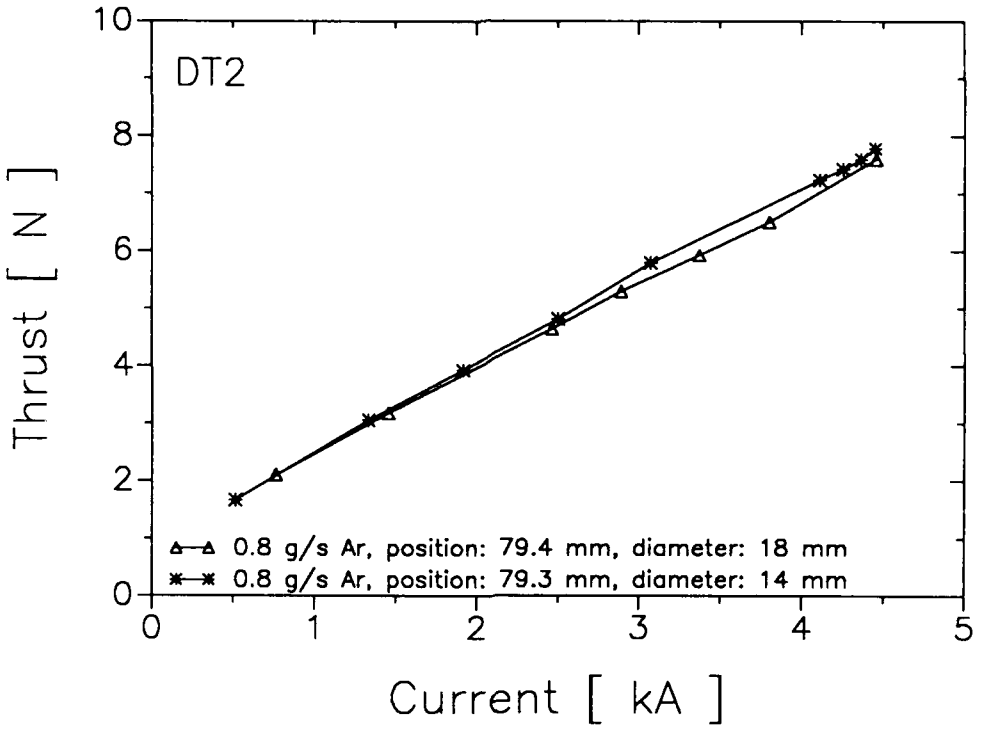

Fig. 2.1.36: Thrust vs. current at different parameters

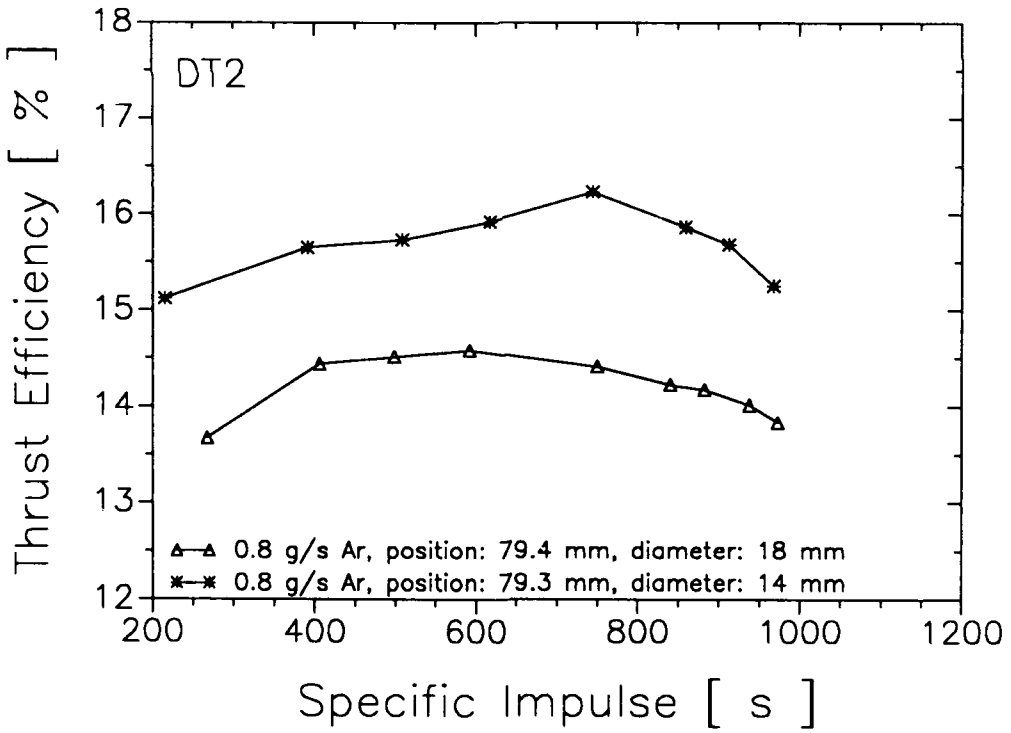

Fig. 2.1.37: Thrust efficiency vs. specific impulses at different parameters

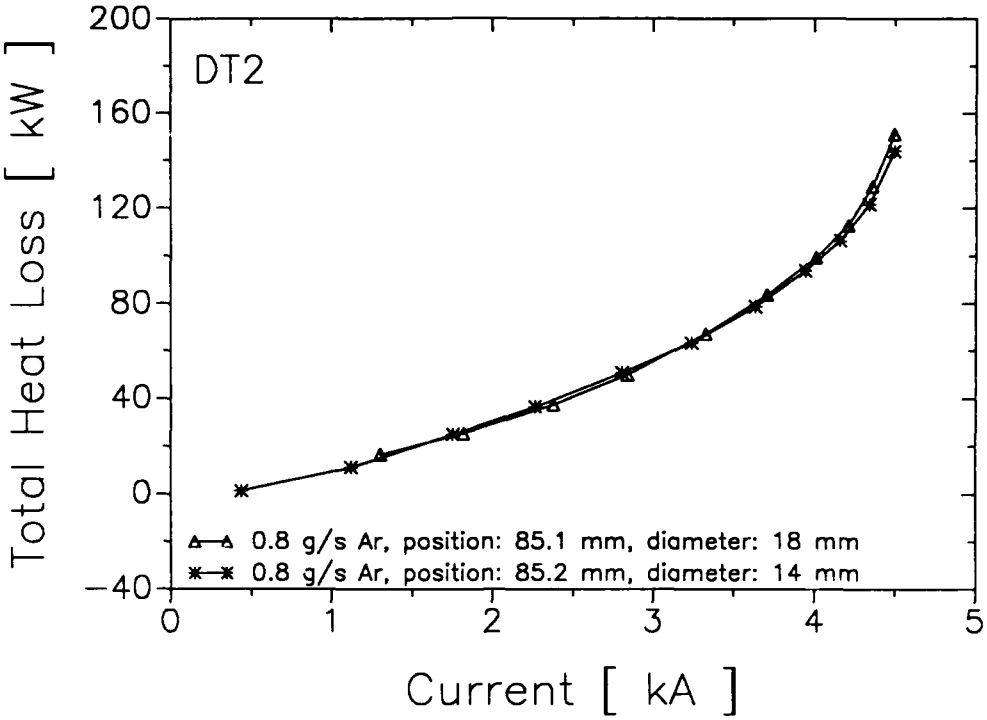

Fig. 2.1.38: Total heat loss vs. current at different parameters

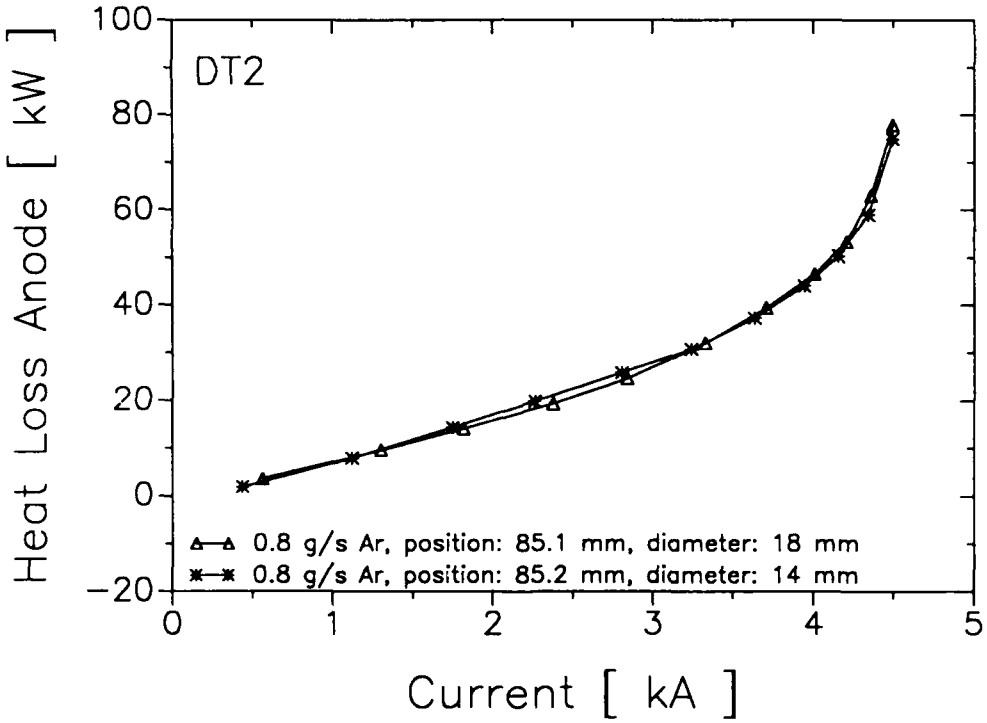

Fig. 2.1.39: Anode heat loss vs. current at different parameters

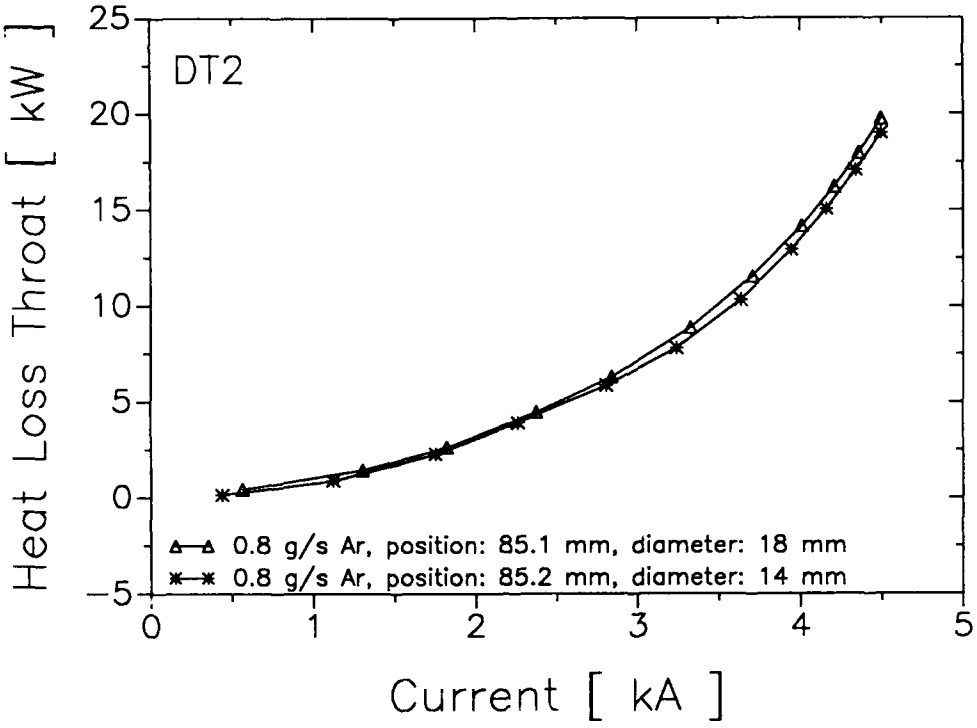

Fig. 2.1.40: Throat heat loss vs. current at different parameters

Figures 2.1.38-2.1.40 show the total, the anode and the throat heat losses. The cathode diameter has almost no effect on the thermal losses. Only the heat loss of the throat segment is slightly higher with greater cathode diameter.

2.1.3 The Onset-phenomena

As mentioned above the magneto-plasmadynamic thruster reach an unstable mode at high power levels: the voltage versus current curve rises steeply and therefore the thrust efficiency decreases. At a current level somewhat above this break in the voltage curve, oscillations of the plasma can be detected in low and high frequency ranges. These onset oscillations were measured with an electrical probe and analysed by a fast fourier transformation to get the frequency spectrum. Figure 2.1.41 shows such an spectrum for the DT2-Thruster, running with 0.8 g/s argon at a current level of 4962 A.

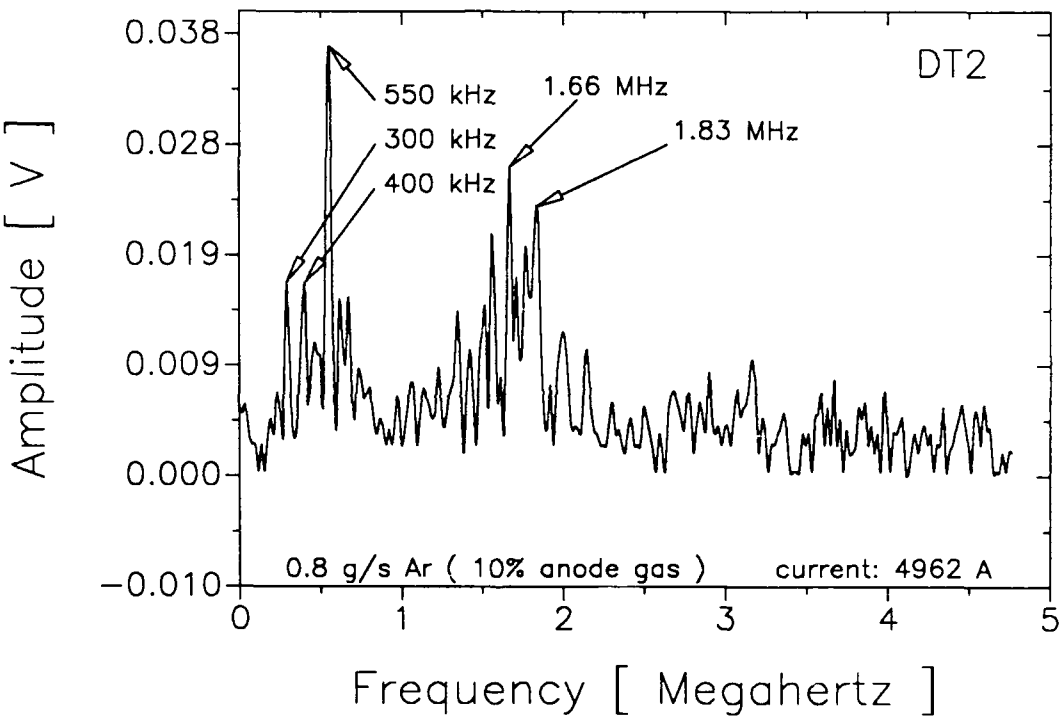

Fig. 2.1.41: Frequency spectrum of plasma oscilations at the DT2-Thruster

Figures 2.1.42 - 2.1.43 show the dependence of the current at the oscillation onset on the cathode position and cathode diameter.

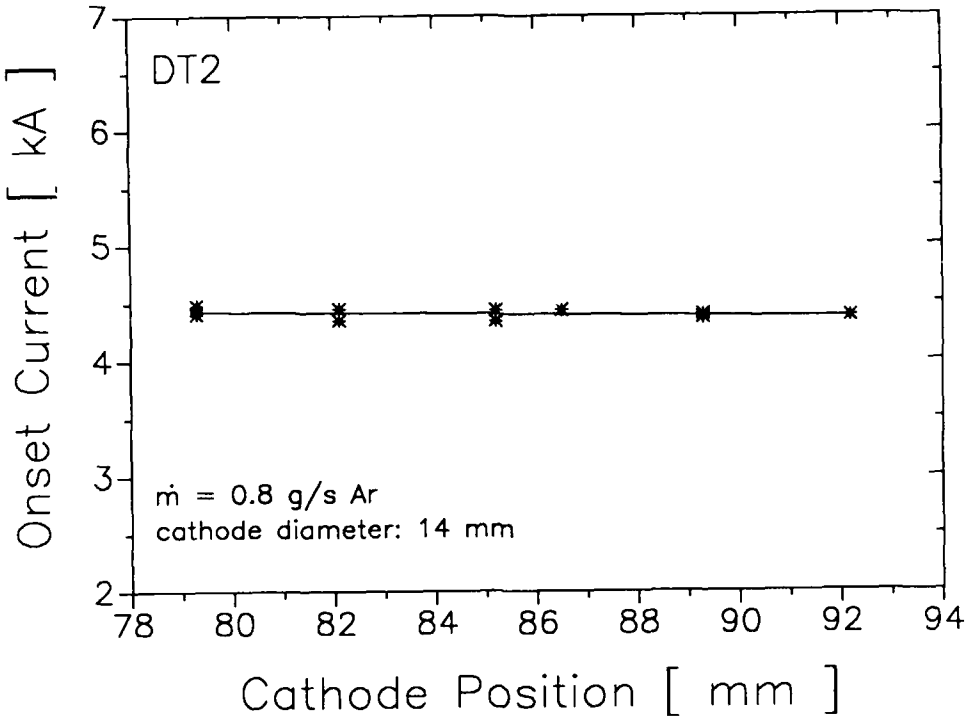

Fig. 2.1.42: Onset current vs. cathode position

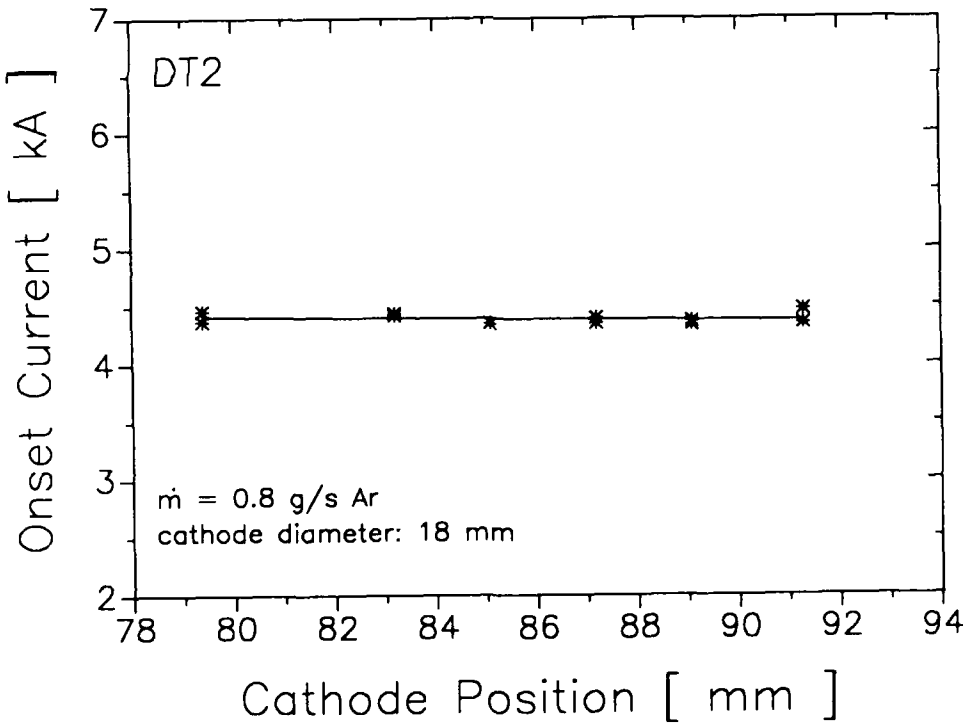

Fig. 2.1.43: Onset current vs. cathode position

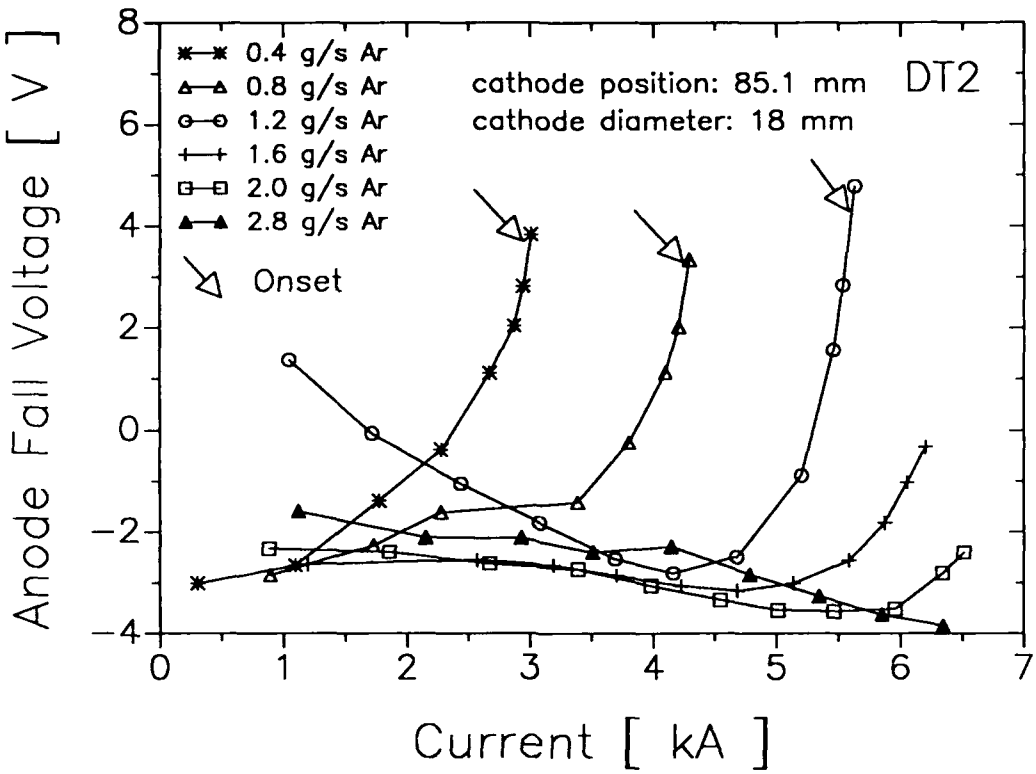

Fig. 2.1.44: Anode fall voltage vs. current for various mass flow rates

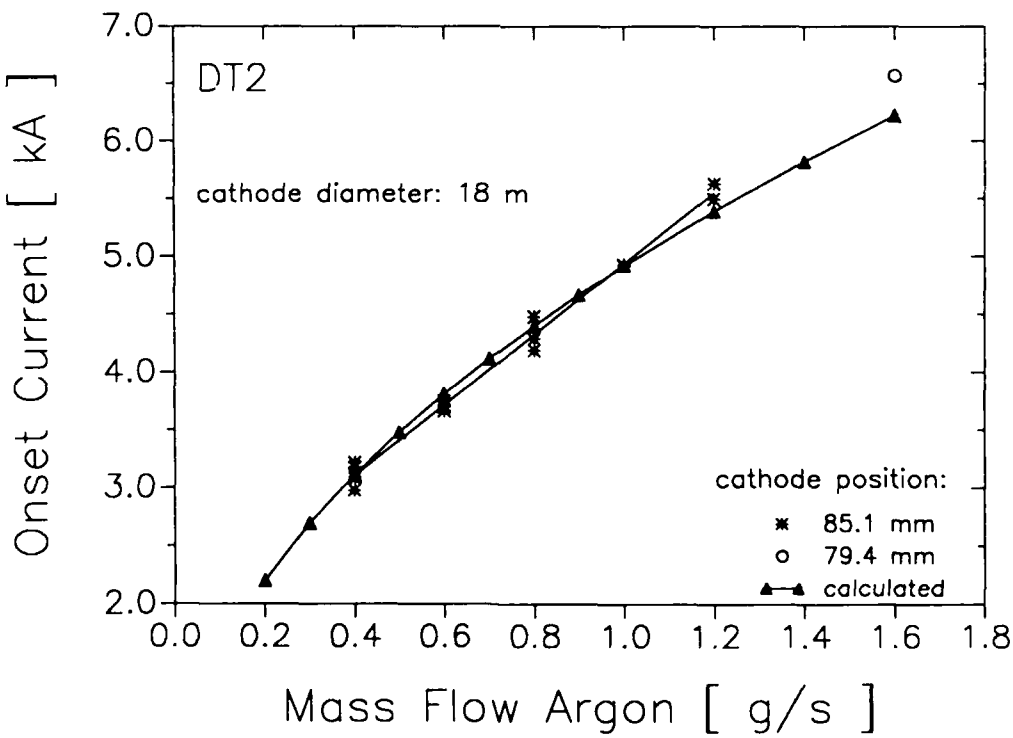

Fig. 2.1.45: Onset current vs. mass flow rates

The current of the oscillation onset does not depend on the cathode position, it is constant over the whole variation range. Also the cathode diameter has no influence on this current level.

The rise of the anode voltage (Fig.2.1.44) characterizes the onset phenomenon, the arrows show the point of oscillation occurence.

Taking these critical currents as a function of the mass flow, they yield an almost linear function, Fig.2.1.45.

Reducing them according to the correlation factor $A = I^2/\dot{m}$, the critical correlation value can be calculated with:

$$A_{crit} = 2{,}4 * 10^{10}\ A^2s/kg$$

With this value, the onset current curve is calculated and also depicted in diagram 2.1.45. It fits very well with the measured curve, indicating that this A_{crit} is a relatively good constant.

First spectroscopic measurements, done at the DT2-thruster running with 0.8 g/s argon, show that in the current range where the voltage rises the second ionisation of the argon atoms starts.

The plasma instabilities will be investigated in more detail theoretically and experimentally at the IRS in the next research period.

2.2 Hot Anode Thruster

A substantial part (≈ 30-50%) of the input power of an MPD thruster is consumed in the anode. Thus, a decrease in these anode losses would raise the performance of these devices.

Former investigations of MPD thrusters with radiation-cooled anodes showed higher thermal efficiencies than those with water-cooled ones, but they were used only with thrusters of a much lower power level and mainly of the applied magnetic field type.

The "Hot Anode Thruster" (HAT) is an attempt to use these advantages of radiation-cooled anodes for thrusters in the power class of 200 kW. Its schematic is shown in Fig.2.2.1. In order to provide a sufficiently large area to radiate the anode input power, the anode flange has a diameter of roughly 40 cm. It is made of thoriated tungsten; the areas not intended to be loaded by the current are covered by tantalum carbide, which is a relatively weak insulator. This coating insulates the radiating anode areas and at the same time increases the coefficient of emissivity by about a factor of 2 versus pure tungsten.

The hot anode is shielded from the other parts of the thruster by a water-cooled copper plate, which is diffusion welded and forms one of the neutral rings of the nozzle.

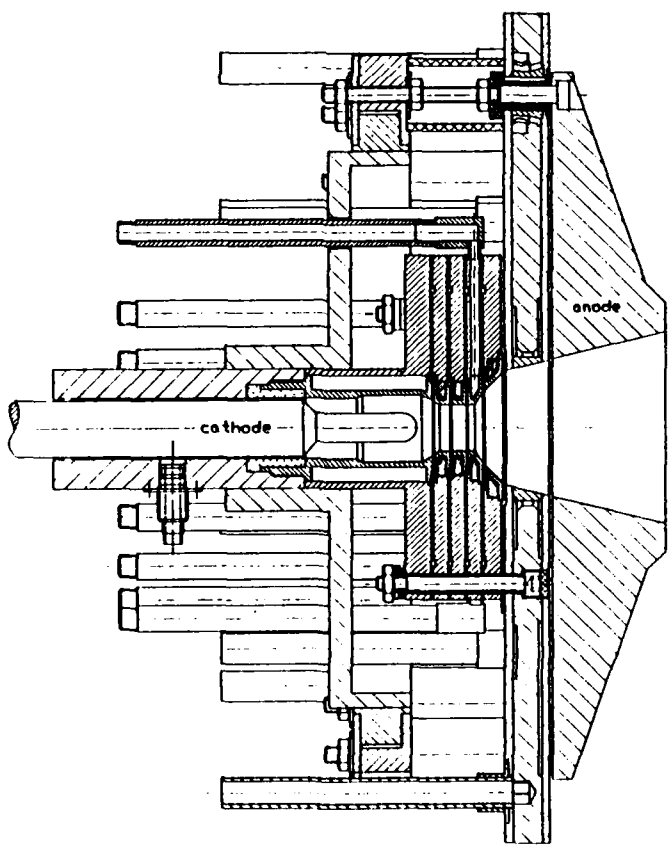

Fig. 2.2.1: Configuration of the "Hot Anode Thruster" (HAT)

The current is fed to the anode by 16 screws made of TZM, a molybdenum alloy, which at the same time act as mounting support for the heavy anode flange. In order to compare the experimental results with those of the water-cooled DT type thrusters, it is designed as closely as possible in the form of the "normal" nozzle type thruster DT2.

Due to the broader anode and first cooling segment, the cathode was put in the same position in respect to the nozzle throat as with thruster DT2. This results in a longer current path, which should yield a somewhat higher voltage than with the "bench-mark" water cooled device.

First experiments are presented in the following diagrams. All experiments were performed with argon. The experimental procedure was as follows: to avoid large temperature gradients, the discharge was ignited at low currents (and hence low power). The current level was held constant for about 10-20 minutes, till the temperature distribution on the anode was constant. Then the current level was raised, etc. The maximum discharge power with these first tests was restricted to about 90-100 kW, due to severe cooling problems of the vacuum tank, which will be solved in the next research period. Fig.2.2.2 shows typical warming up cycles, Fig.2.2.3 shows the temperature distribution on the anode. The indicated power levels are those of the discharge power.

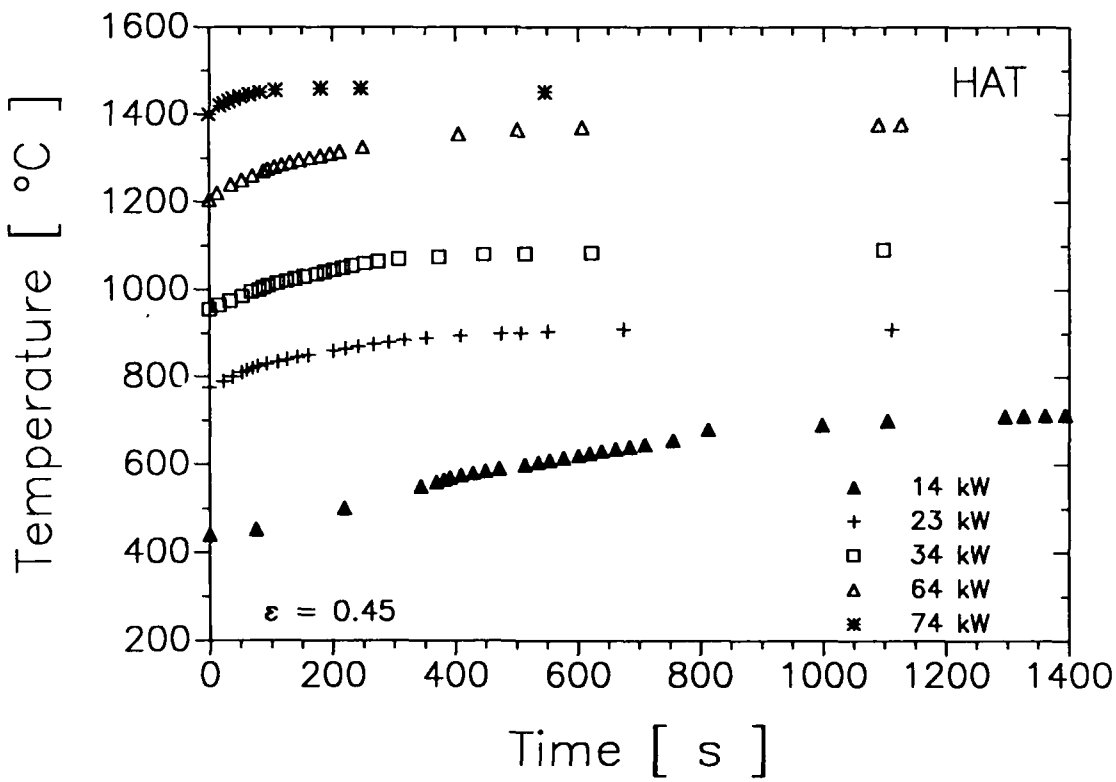

Fig. 2.2.2: Heating phases of the HAT running with $\dot{m}$ = 0.3 g/s argon

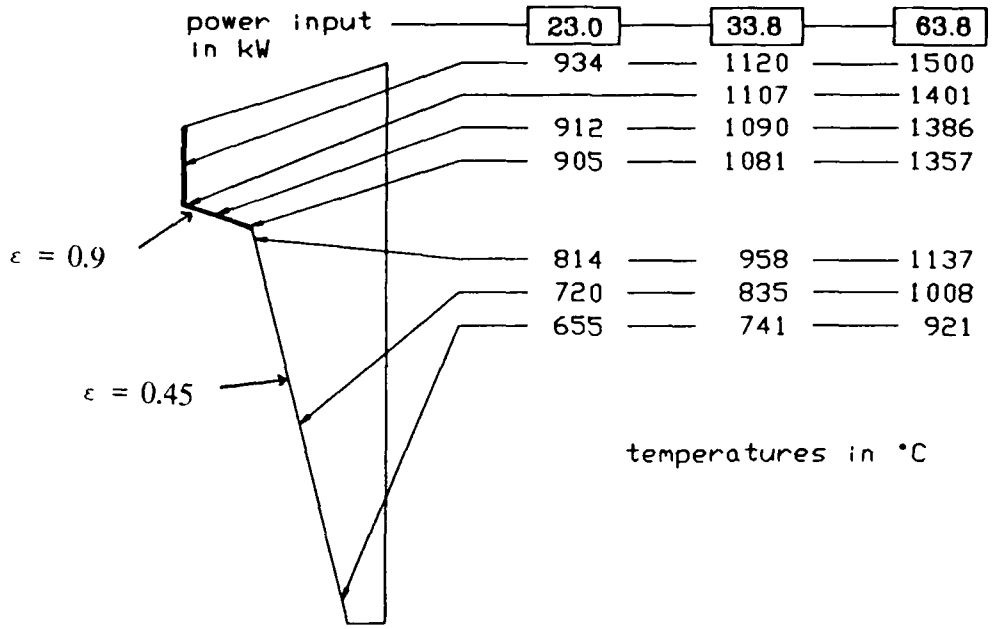

Fig. 2.2.3: Temperature distribution on the anode surface of the HAT, running with $\dot{m}$ = 0.3 g/s argon

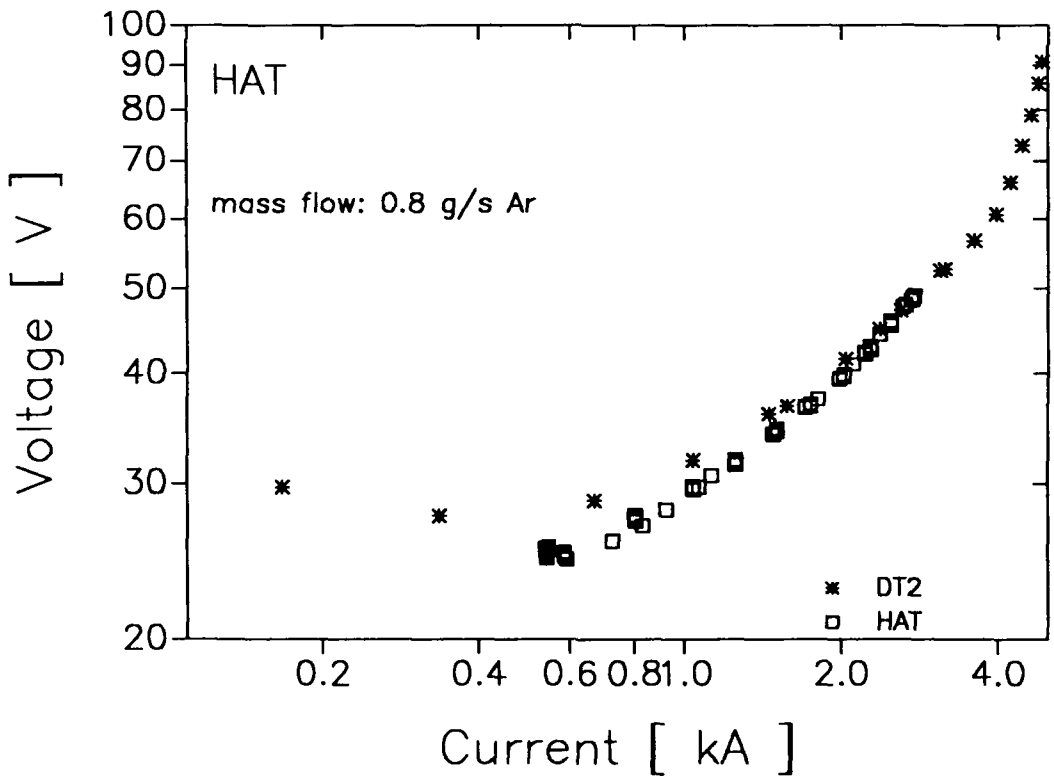

Fig. 2.2.4: Voltage vs. current curve of the HAT in comparision with the DT2-Thruster

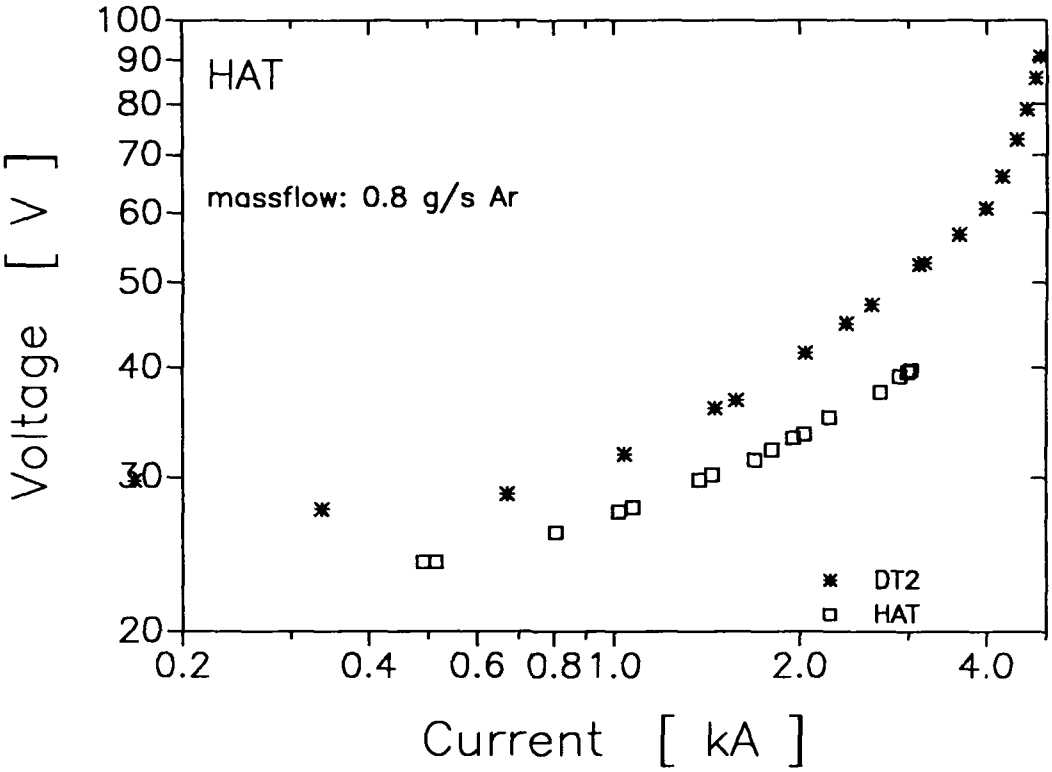

Fig. 2.2.5: Voltage vs. current for the HAT in comparision with the DT2-Thruster

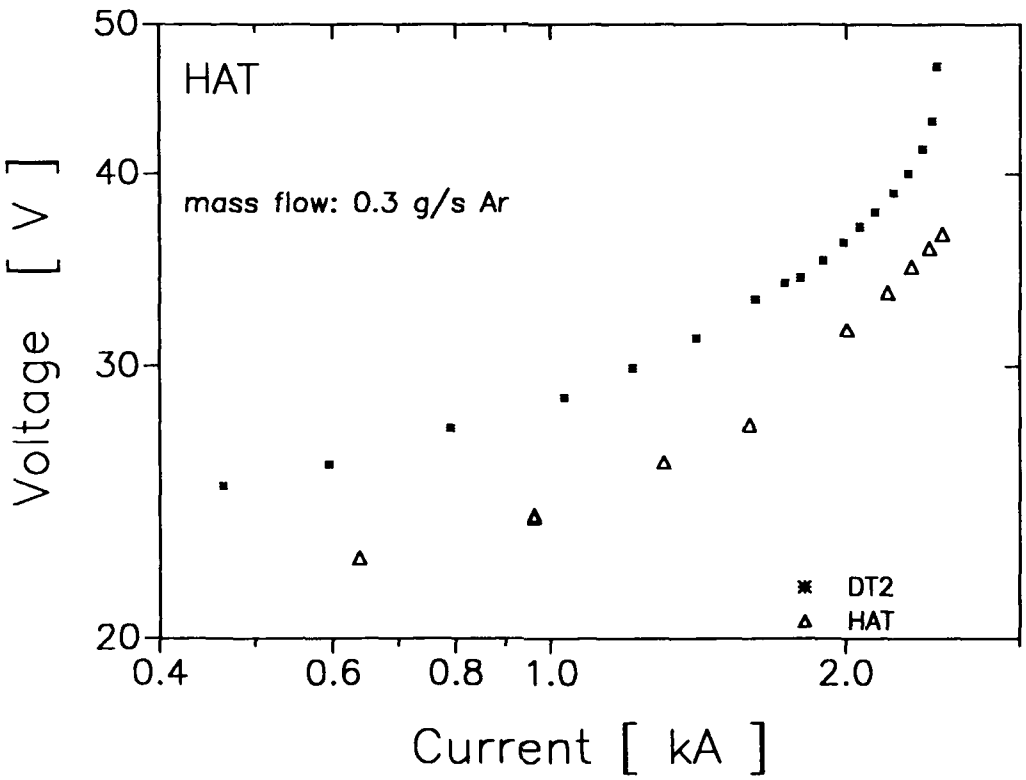

Fig. 2.2.6: Voltage vs. current for the HAT in comparision with the DT2-Thruster

Fig. 2.2.4 to 2.2.6 show the voltage - current characteristics with 0,8 g/s argon as propellant compared to the water-cooled DT2-thruster. In the very first run, Fig. 2.2.4, the voltage was only slightly lower than with the DT2, but in further runs, like those depicted in Fig. 2.2.5 and Fig. 2.2.6 ,there was a clear difference of about 5 to 10 V.

This difference or "run-in" effect could not yet be explained. The lower discharge voltages shown in the later HAT runs promises to achieve improvements in efficiency, so in a further research period the HAT will be put on a thrust stand.

The power input into the anode could only be estimated. In Fig. 2.2.7 the heat flux into the cooling plate is depicted as a function of the discharge power, an almost linear function. If one assumes that the anode flange radiates approximately as much at the front side as at the rear side, the power into the anode would be about one third of the discharge power.

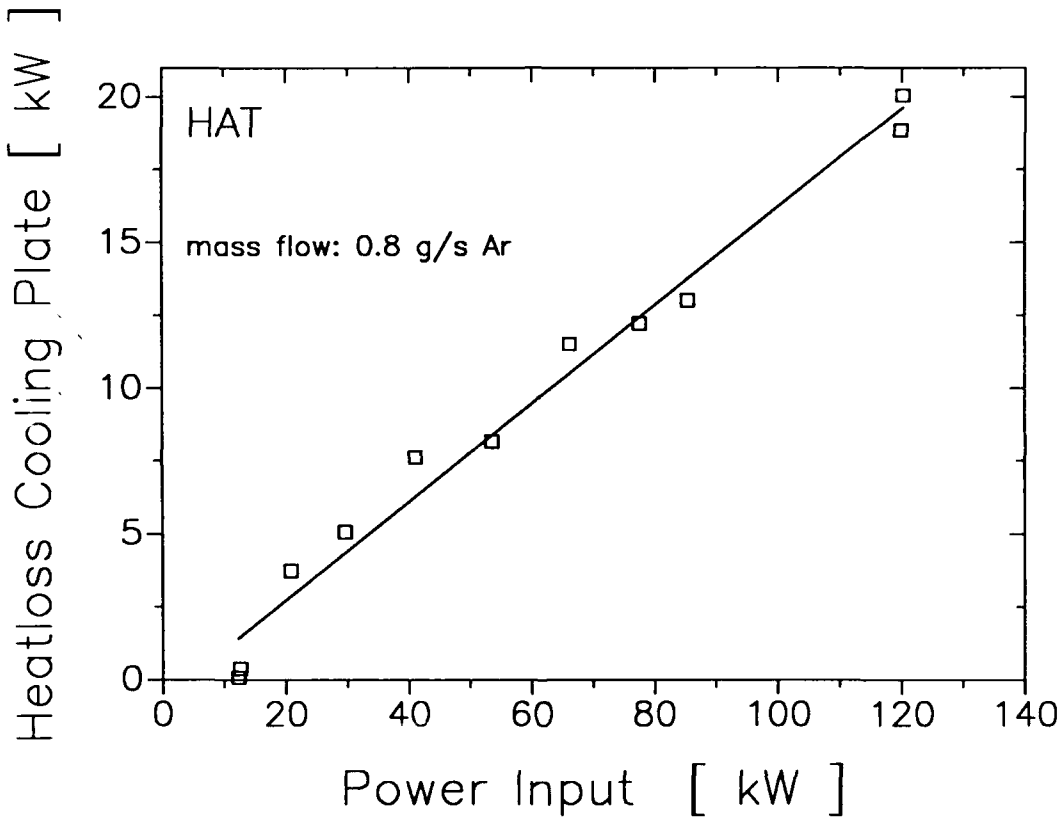

Fig. 2.2.7: Heat loss into the cooling plate

The temperature of the anode flange, measured with a pyrometer at the marked point in Fig. 2.2.3, is shown as function of the power and for the cooling phase as function of time for the propellant flow of 0.8 g/s and 0.3 g/s, Fig. 2.2.8 and 2.2.9. The maximum temperature reached was ca. 1600°C, and was limited by severe cooling problems of the vacuum tank. Fig. 2.2.10 shows a typical cooling down curve of the anode after a run. The photo 2.2.11 shows the HAT in operation, $\dot{m}$ = 0.8 g/s. The emissivity for tungsten was chosen ε = 0,45 , the emissivity of the TaC coating ε = 0,9.

With the water-cooled DT2 the onset of oscillations occurs with 0.3 g/s argon at 2400 A. With the HAT at 2500 A, the maximum current in this run, the onset was not yet noticed and the slope of the U, J curve was not as steep as with the DT2-thruster.

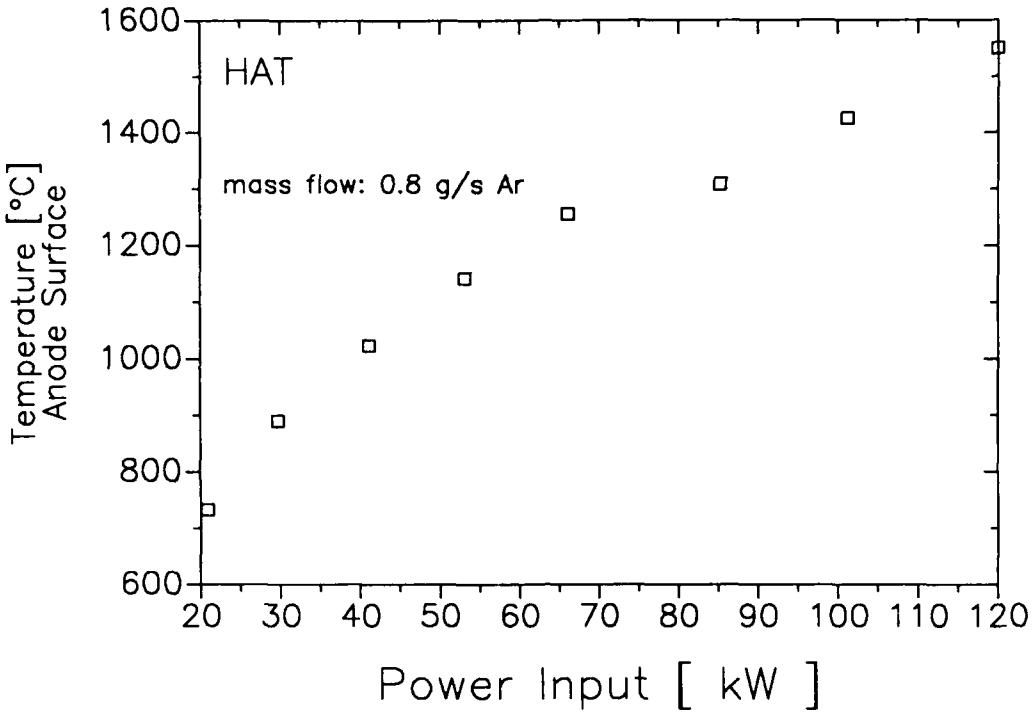

Fig. 2.2.8: Temperature of the anode surface as a function of the discharge power

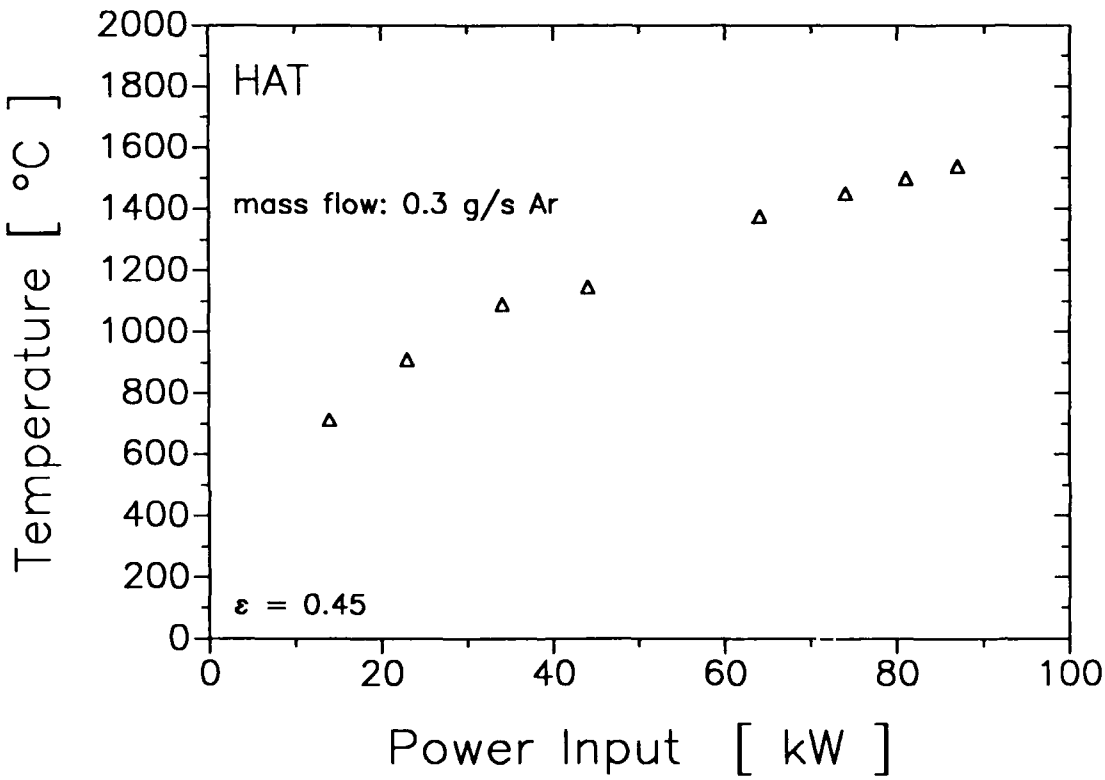

Fig. 2.2.9: Temperature of the anode surface as a function of the discharge power

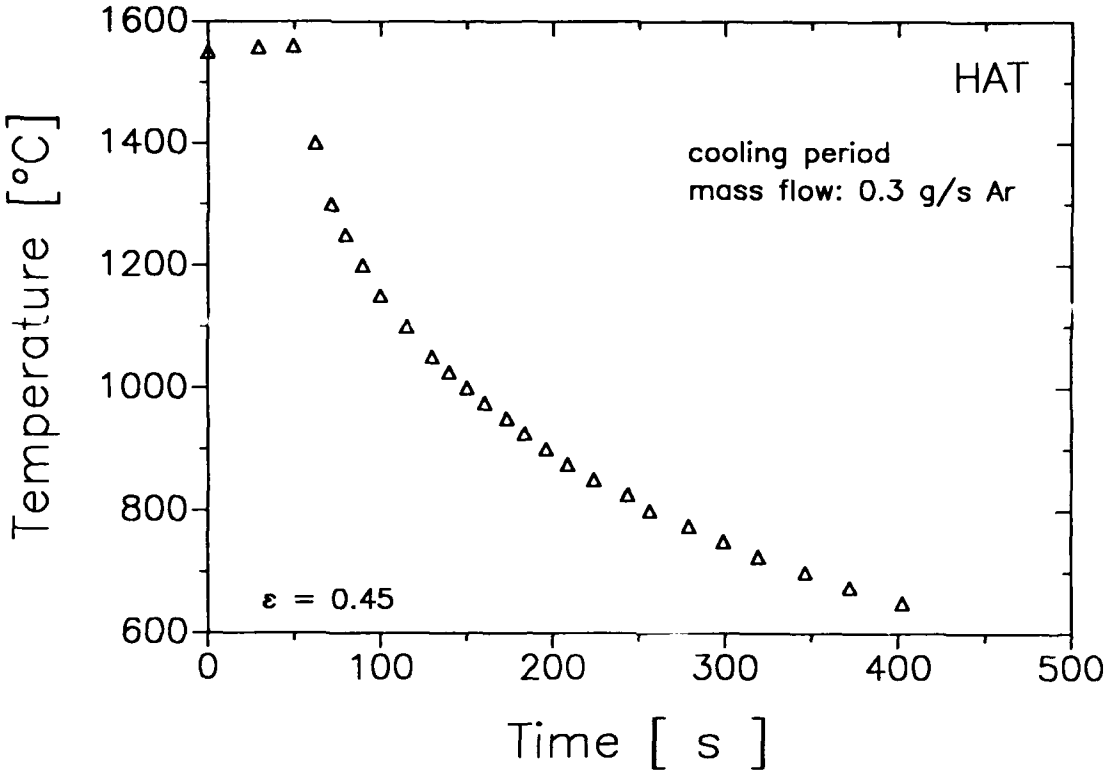

Fig. 2.2.10: Cooling-off curve of the anode, after running with $\dot{m}$ = 0.3 g/s argon

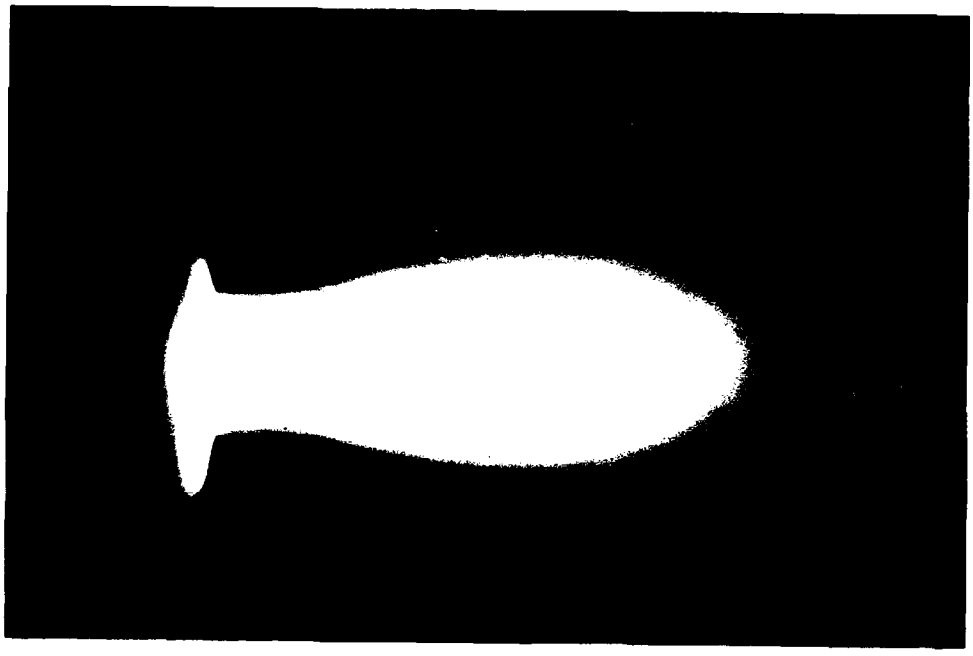

Fig. 2.2.11: The HAT in operation with argon as propellant

2.3 Cylindrical MPD Thruster

In contrast to the nozzel type MPD thrusters, which are in effect hybrids of pure MPD- and thermal arcjets, cylindrical thrusters are predominantly MPD devices. Therefore, they should give better insight into the mechanisms of MPD gas acceleration than the complex MPD arcjets. Further, the elongated electrodes should yield a relatively radial current distribution and therefore it is hoped to reduce the pinch effect found to be an essential factor affecting the anode mass starvation, according to the calculations of Hügel [5] and the Princeton [7] experiments. This may also be an explanation for the good performance results obtained with cylindrical thrusters in a pulsed operation mode at Princeton [8]. To prove these assumptions, a laboratory cylindrical MPD accelerator for high power and steady state operation was built and tested. The main emphasis of the experiments with this thruster during the contract period should have been high current experiments. However, due to cathode failures, which are described in a separate paragraph, the current limit was only about 8000 A. In a further research period, with redesigned cathode, it is hoped to overcome these constraints.

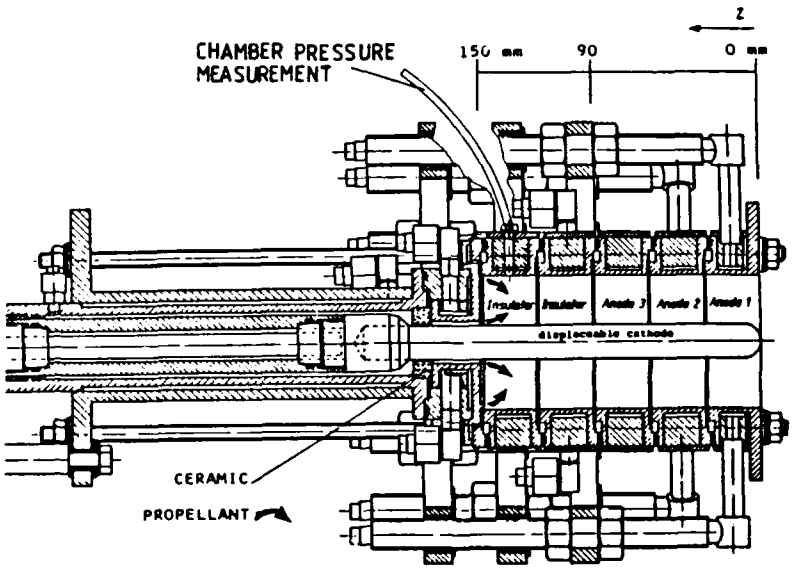

Fig. 2.3.1: Configuration of the MPD-Thruster ZT1

Thruster

The ZT1 thruster, shown in Fig. 2.3.1 is a pure laboratory model which has a modular construction to allow as many geometrical variations as possible. The thruster consists of a plenum chamber of 70 mm in diameter, which is divided into five copper rings of similar size, and a backplate. The last three downstream rings can be connected as anode; the current through each anode ring is measured separately. The reason for this partition is to give some insight into the anode current distribution. One of the neutral segments is supplied with a feed-through hole, which can serve as a part of the pressure gauge, as used in the experiments described in this paragraph, or as location for pyrometric cathode temperature measurement through optical fibres. The cathode, which is 220 mm long and 18 mm in diameter, is a 2% thoriated tungsten rod with a casted copper base. The cathode is built as a displaceable one and can be positioned during the experiment with a remotely controlled electromotor. The cathode is guided in boron nitride pivot upstream of the water cooled backplate. All parts but this ceramic pivot are individually water cooled. Two propellant ports are anticipated in a slit around the cathode and at the anode radius respectively, both at the backplate.

Vacuum Tank

The thruster is mounted in a partially water-cooled steel tank of 2 m diameter and 3 m length, which is connected to the 200,000 m^3/h plus vacuum pumping system. The tank is supplied with 9 windows, including one with optical glass for pyrometer measurements and one for end-on sight. Among the different feed-throughs are four for high currents up to 10 kA. The power supply is a current regulated rectifier with a maximum current of 48 kA and a maximum power output of 6 MW which allows a potential free use. No thrust measurement is foreseen at present, but will be implemented in future research periods.

Measurement System

The measured data were: The discharge voltage and the currents through the three anode segments. To avoid grounding the power supply, isolation amplifiers have to be used. The two propellant flows were determined by Tylan mass flow controllers. The cooling water flows and their temperature rises were measured to calculate the losses in the different neutral and anode segments and hence the anode fall voltage. The cathode position was measured by a potentiometer and the temperature of the cathode tip with a spectral pyrometer. The tank pressure was monitored by a Granville Phillips Convectron gauge. The discharge plenum pressure was measured with a Hottinger and Baldwin differential pressure gauge and the tank pressure was added. All data were registered by an Intercole multi-channel data acquisition system controlled by a DEC PDP 11/73, where the data were reduced and stored.

High Current Experiments

Two high current runs were performed, but had to be terminated because of cathode failure, as mentioned above.

The normal procedure of the test was as follows: The cathode was positioned with the cathode tip protruding about 10 mm from the backplate (z = 140). The gas flow was set and the discharge was ignited with a Paschen breakdown at a set current of about 2000 A. The discharge needed about 1 to 2 seconds to stabilize; that means that the tip glowed. Figures 2.3.2a and 2.3.2b depict two examples of such an ignition for a retracted and forward cathode position. With the thermionic emission (see chapter 3) the current stabilizes and becomes smooth and elongated. Then the current was raised to 4000 A and the cathode was shifted to the foreseen position by a motor with a velocity of about 1 mm/s.

In Fig. 2.3.3 to 2.3.8 the results are depicted for 4 g/s argon, divided 1:1 between the anode and cathode propellant inlets. Fig. 2.3.3 shows the evolution of the current distribution on the three anode rings on a time profile. The first part up to the indicating arrow describes the ignition and the positioning part of the cathode, the second part of the diagram shows the evolution of the anode current distribution during increasing current at the foremost cathode position x = 0 mm.

Directly after ignition, most of the current goes into the anode segment 3, the rear ring. Moving the cathode downstream leads to a shifting of the anode current attachment to the front anode ring, but now with a more even distribution between the three anode rings. The arc was ignited with a mass flow of 2 g/s. When stable conditions had been reached, the mass flow was raised to 4 g/s. The gap in Figures 2.3.3 and 2.3.4 indicates the time to set the new mass flows. The higher mass flow does not change the discharge voltage significantly. Raising the current up to ca. 8000 A does not change the current distribution essentially, except for some minor rearrangements. Only when the current is above 7500 A, it seems to concentrate at the front ring. Figure 2.3.4 shows the corresponding voltage. During the shifting of the cathode, the voltage declines from 33 V to 18 V (with a constant current of 4000 V) due to the shortening of the current path. The current rise from 4 to 8 kA effects only an almost linear voltage rise of 1.5 V, Fig. 2.3.5.

In Fig. 2.3.6 to 2.3.8 a similar run is plotted, in which the discharge was ignited with an elongated cathode (x = 0 mm). After ignition, almost no current is taken by anode ring 3 (rearmost anode ring), but almost 3/4 by the front ring. After a relatively quick current rise to 4000 A, the current distribution rearranged in ca. 40 sec to a roughly even distribution, which remained with the current rise up to ca. 8 kA. The voltage does not differ from the above described case. Also here the mass flow was raised from 2 g/s (during ignition) to 4 g/s, indicated by the gap in the curves of Fig.2.3.5 and 2.3.6.

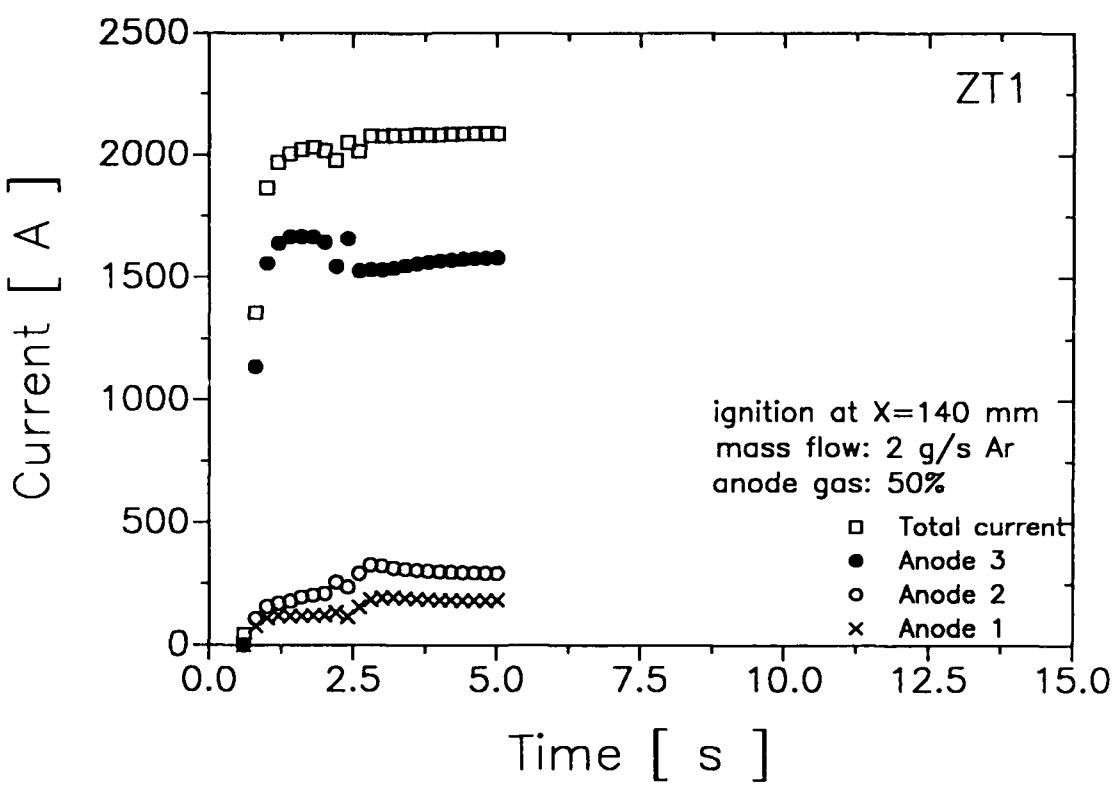

Fig. 2.3.2a: Current distribution during starting phase with retracted cathode (z = 140 mm)

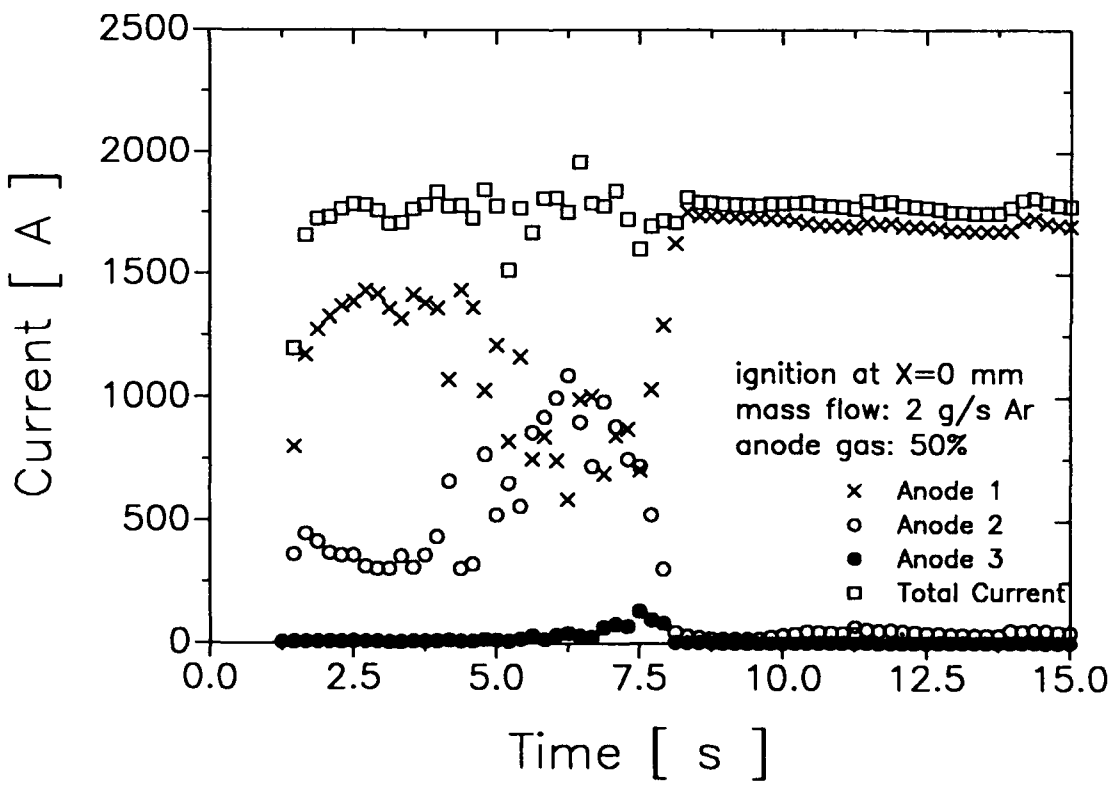

Fig. 2.3.2b: Current distribution during starting phase with elongated cathode (z = 0 mm)

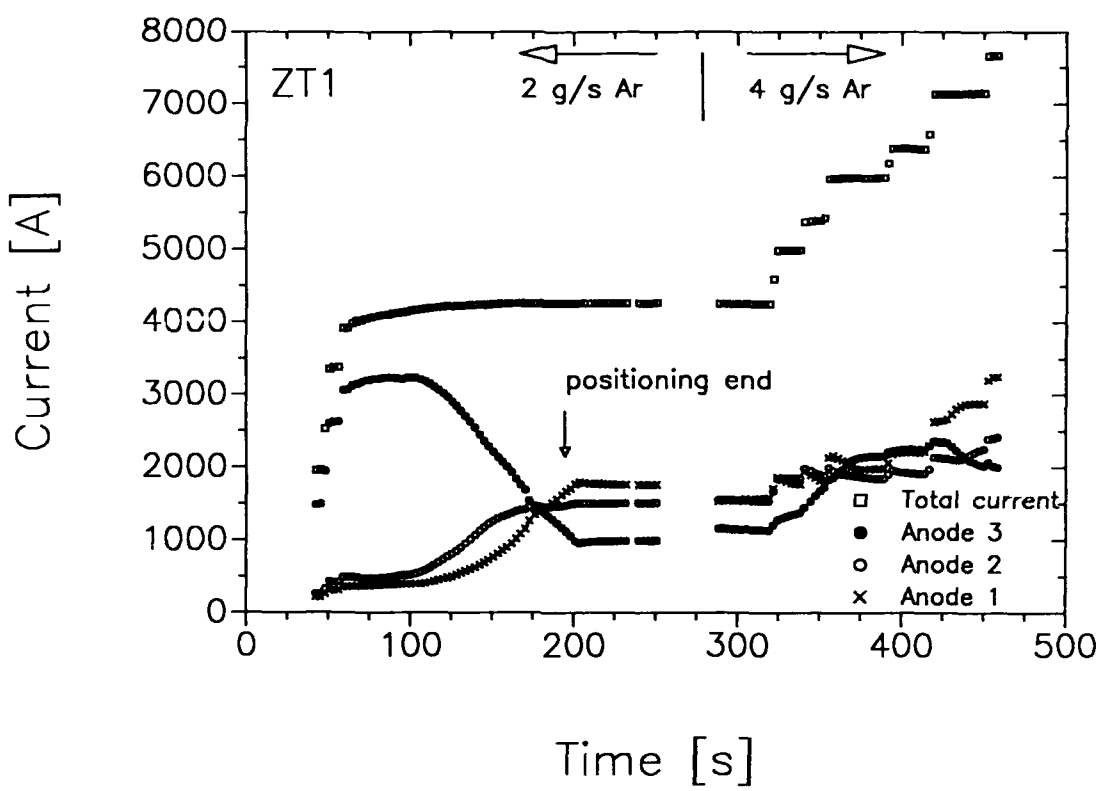

Fig. 2.3.3: Current distribution as a function of time

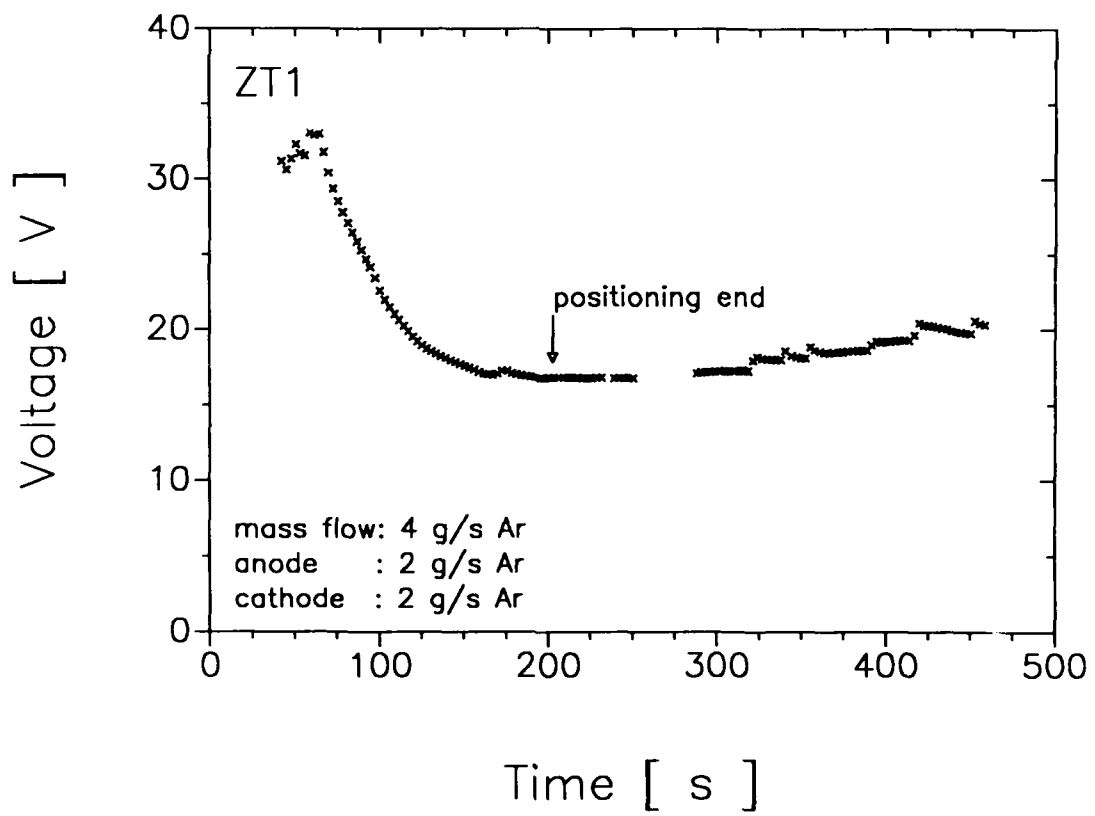

Fig. 2.3.4: Discharge voltage as a function of time

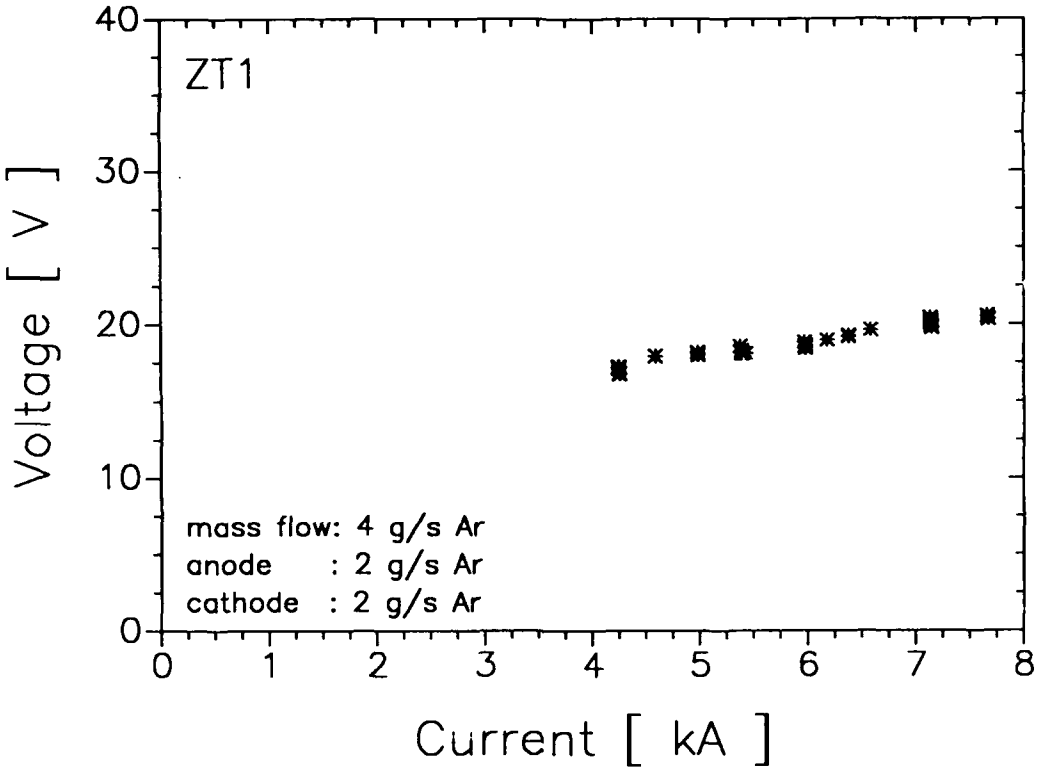

Fig. 2.3.5: Discharge voltage as a function of current for 4 g/s argon, cathode position: 0 mm

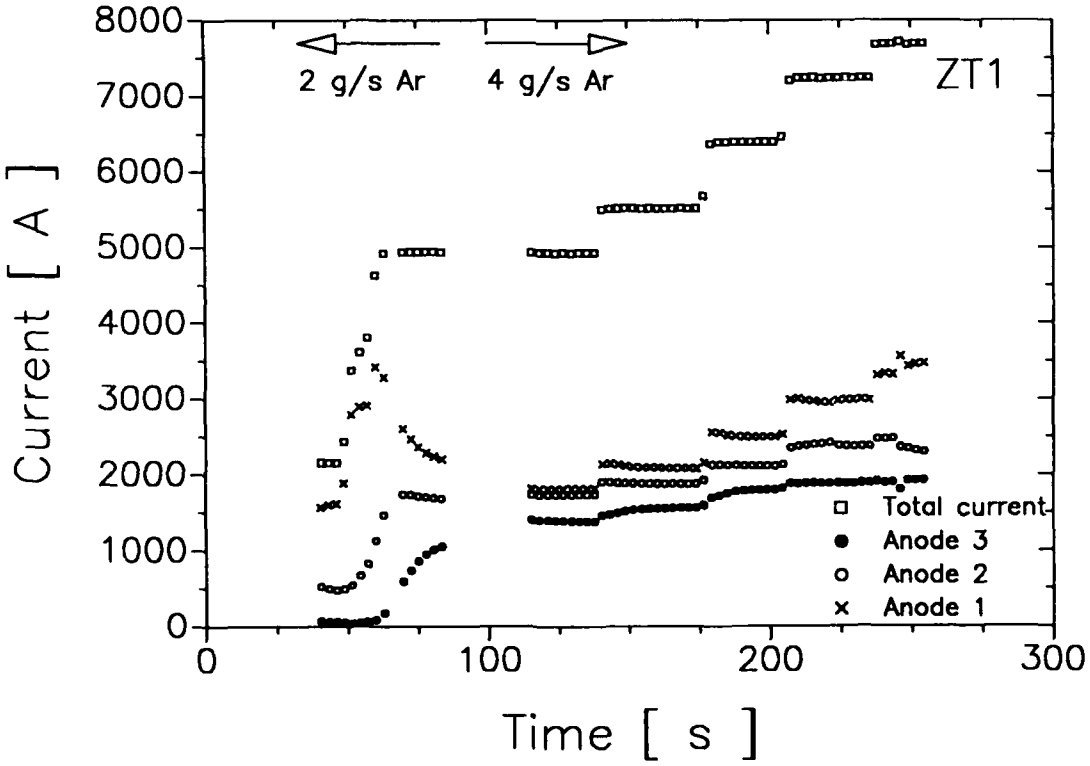

Fig. 2.3.6: Current distribution as a function of time

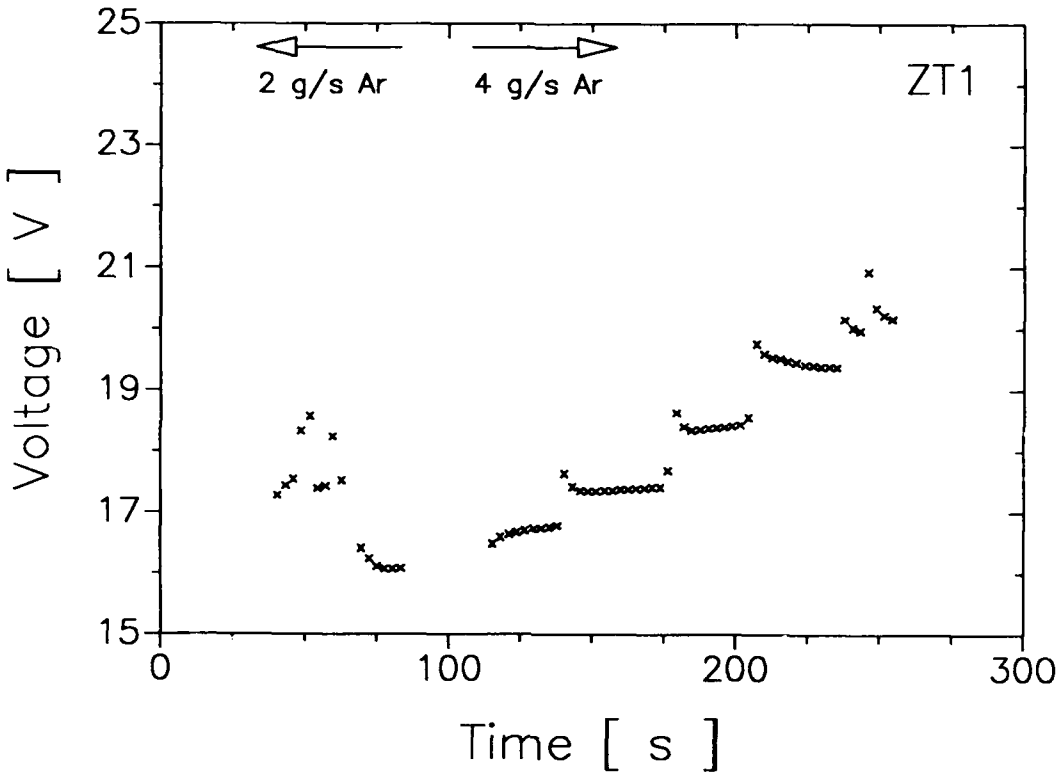

Fig. 2.3.7: Discharge voltage as a function of time

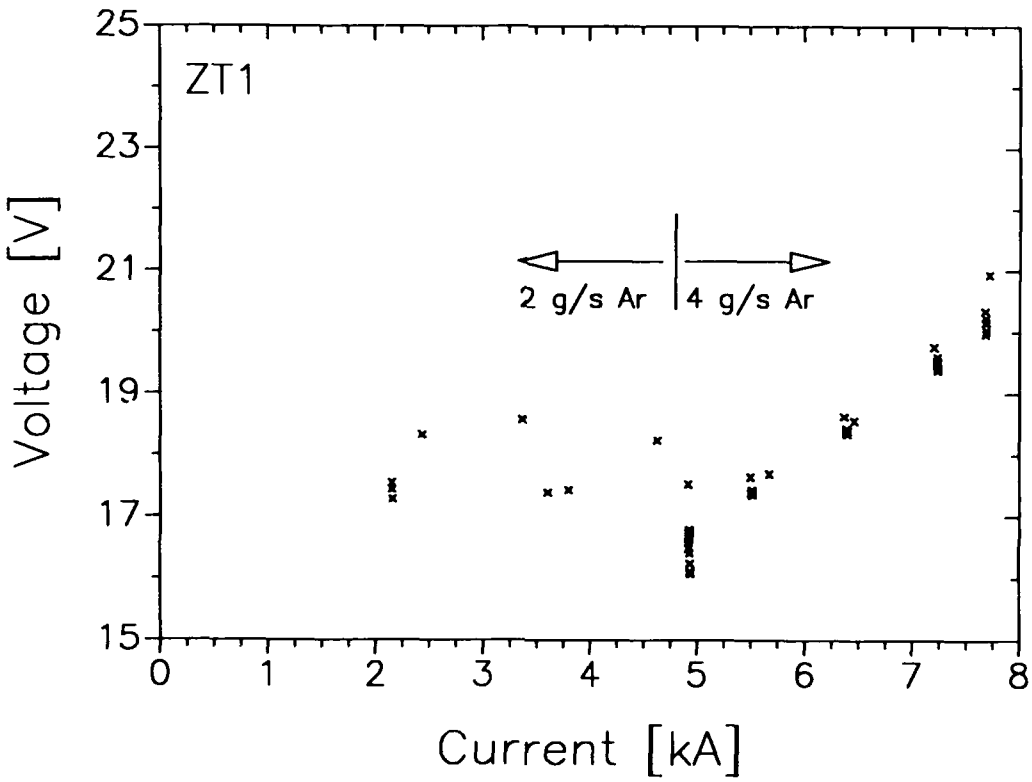

Fig. 2.3.8: Discharge voltage as a function of current, cathode position: 0 mm, for 2 respectively 4 g/s argon

Plenum Pressure

The plenum pressure was measured at a position 1 cm in front of the backplate, which is indicated in Fig. 2.3.1. For two mass flows, 0.8 g/s and 4.0 g/s argon, Fig. 2.3.9a,b and 2.3.10a,b, divided 1:1 between the anode and cathode propellant inlets, the plenum pressure is depicted, parallel to the discharge voltage, as a function of cathode position. The mass flow, being higher by a factor of five, effects also a higher pressure level, but only by about a factor of two.

The pressure corresponds to the voltage, and hence it is an almost linear function of the discharge power, Fig. 2.3.11. It is about one order of magnitude smaller than with the nozzle type DT thrusters, where the cathode is confined in an arc chamber.

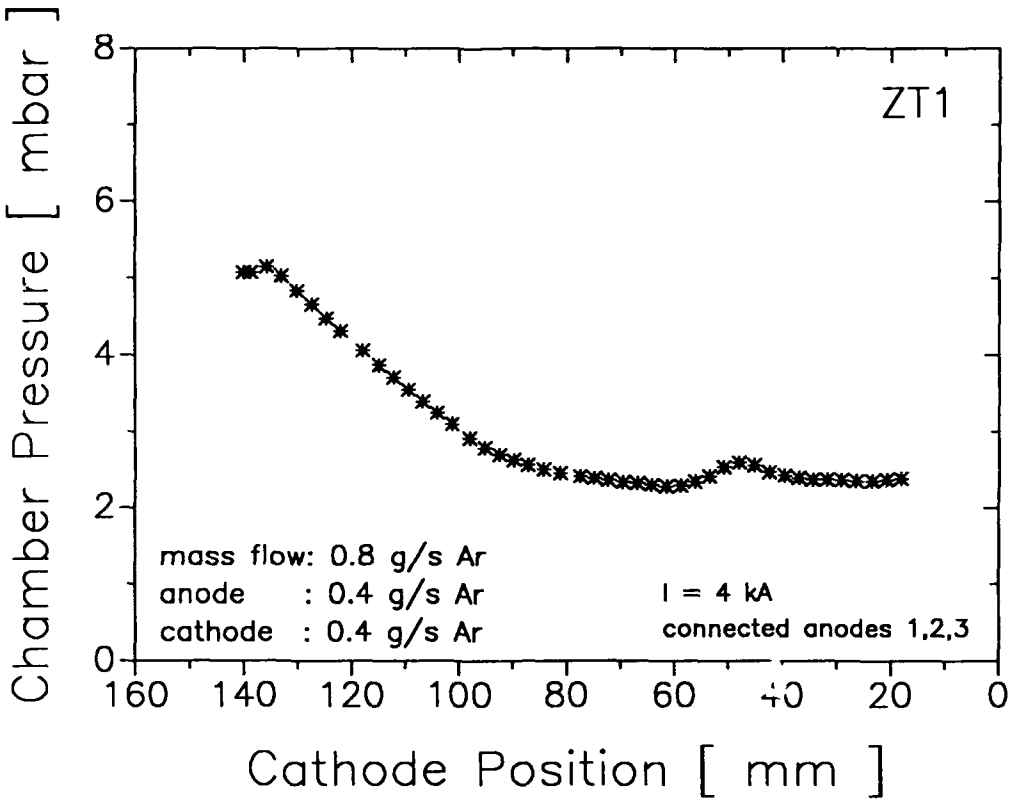

Fig. 2.3.9a: Chamber pressure vs. cathode position for 0.8 g/s argon

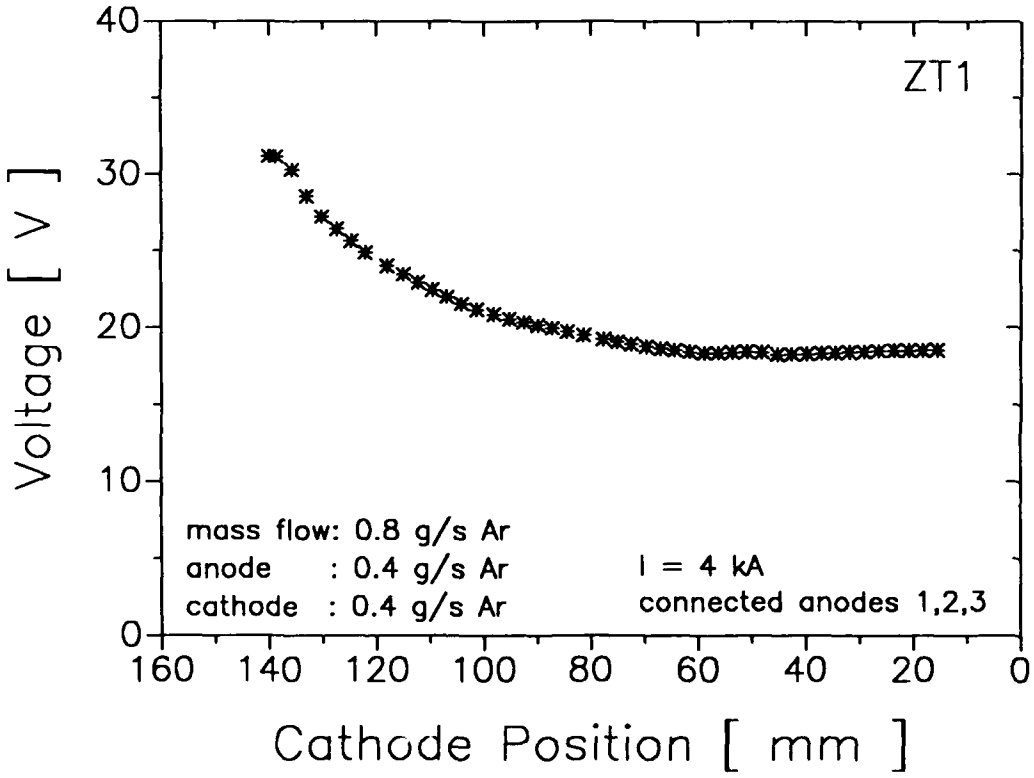

Fig. 2.3.9b: Corresponding discharge voltage vs. cathode position

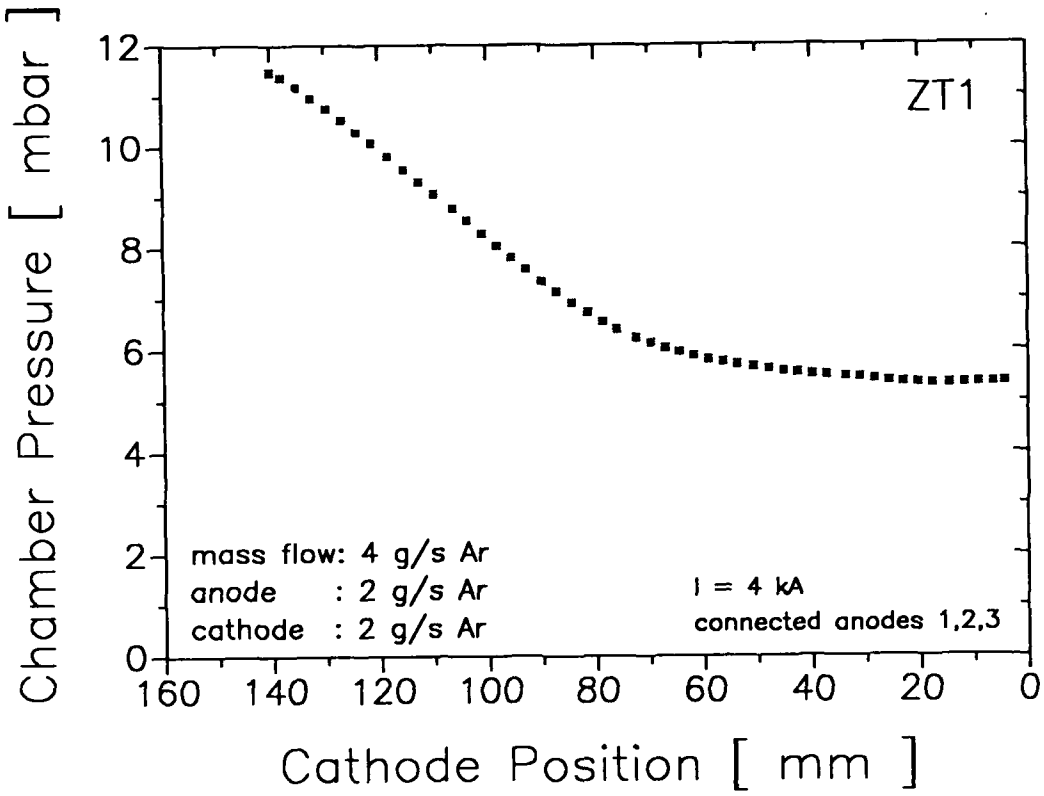

Fig. 2.3.10a: Chamber pressure vs. cathode position for 0.4 g/s argon

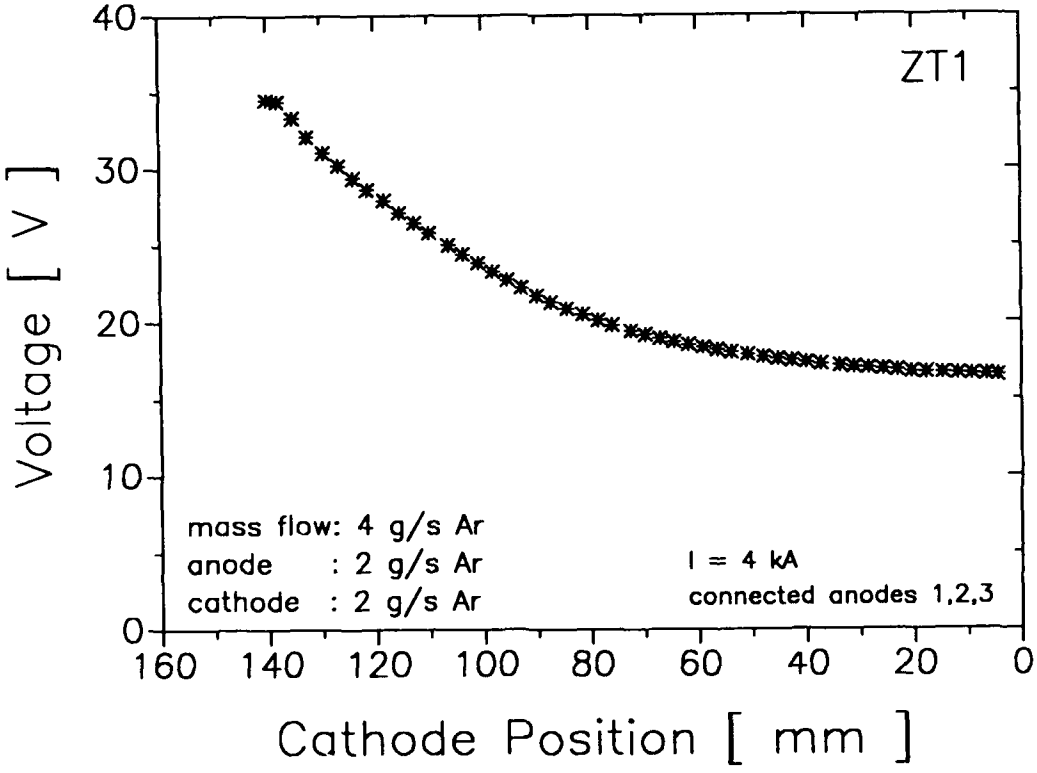

Fig. 2.3.10b: Corresponding discharge voltage vs. cathode position

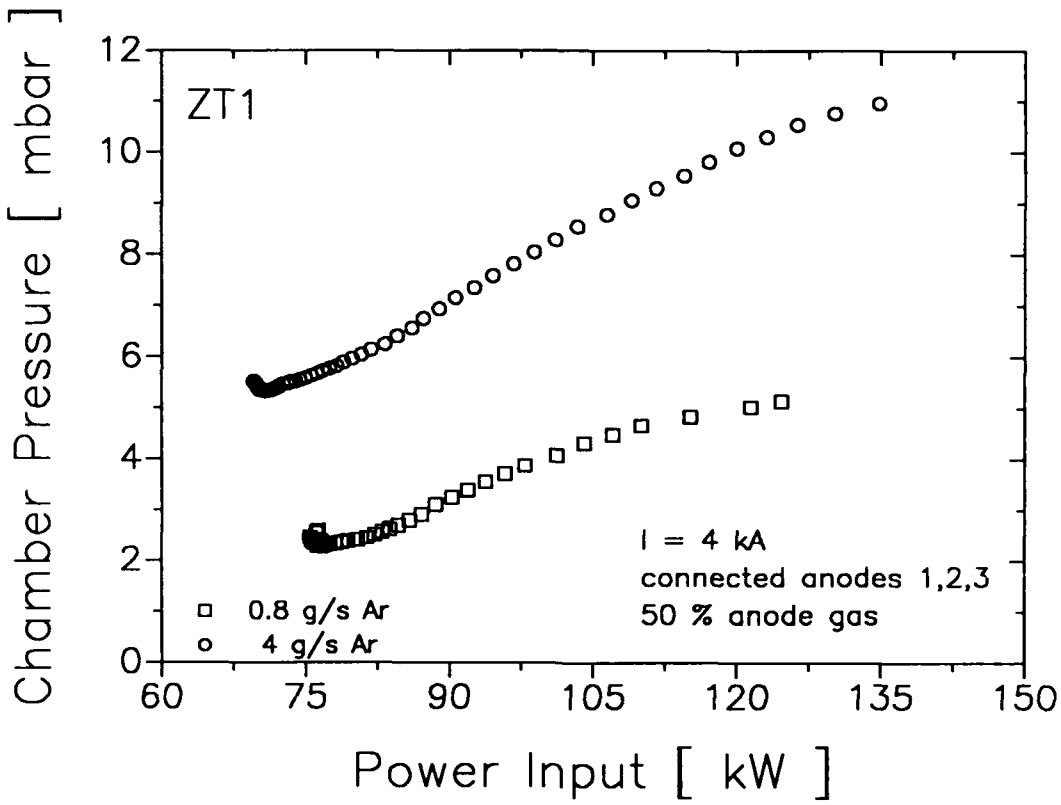

Fig. 2.3.11: Chamber pressure vs. discharge power for two mass flows at a constant current level of 4000 A

Protruding Cathode

In a further experiment, one neutral segment was removed, so that with a fully shifted cathode, the cathode protruded from the anode.

In Fig. 2.3.12a the anode current distribution during the shifting of the cathode is depicted for a total current of 4000 A. At a rear position, 3/4 of the current enters the anode ring 3, and when the cathode is moved downstream, this distribution rearranges totally. Protruding the cathode out of the anode plane augments this process further: at position x= -10 mm, 3/4 of the current now enters the anode ring 1, and less than 5% the anode ring 3.

The corresponding discharge voltage, Fig. 2.3.12b, first decreases with advancing cathode and increases slightly when the cathode tip reaches the anode plane. In Fig. 2.3.13 the variation of the discharge voltage with the current for a retracted cathode is compared to that of a protruded cathode. The voltage with the protruding cathode is almost constant and about 2/3 of that in the retracted case.

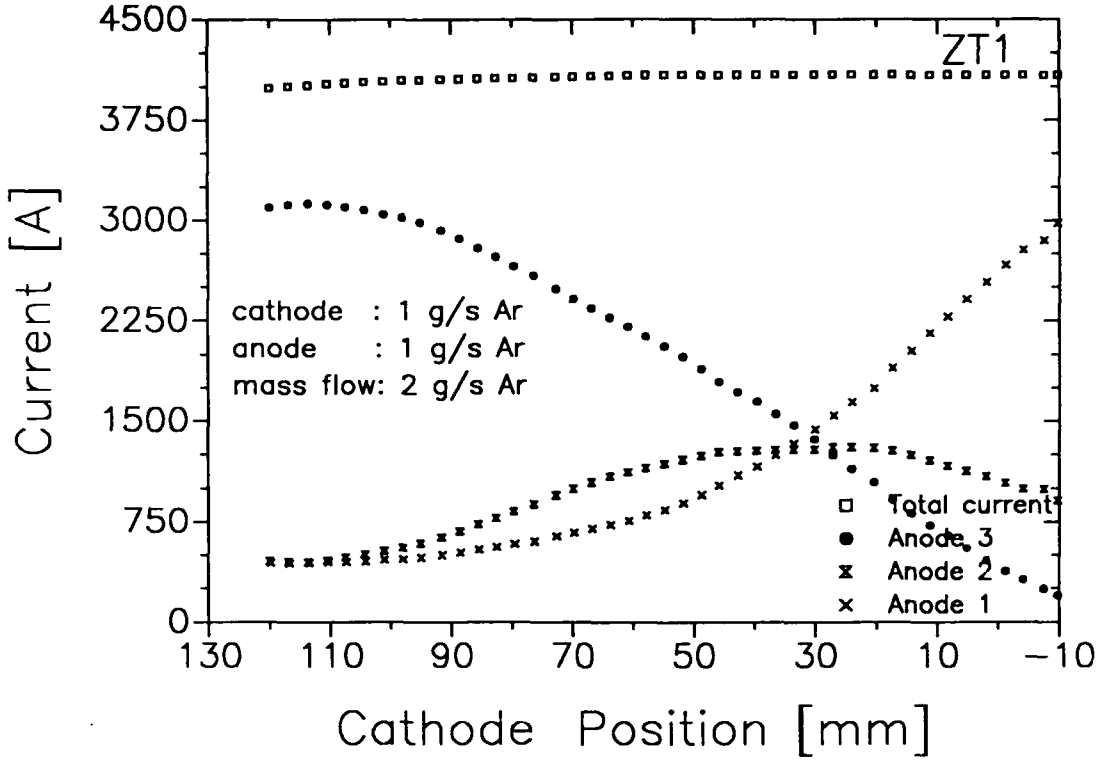

Fig. 2.3.12a: Anode current distribution as a function of the cathode position with a four segmented thruster

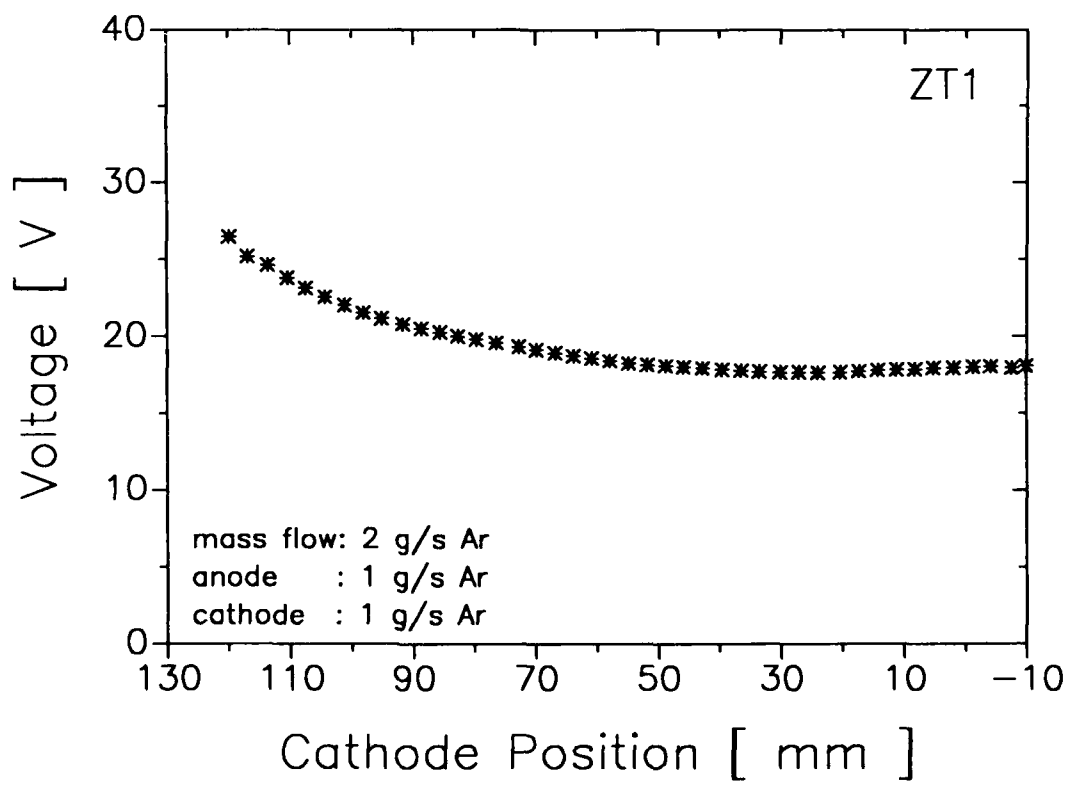

Fig. 2.3.12b: Corresponding discharge voltage vs. cathode position

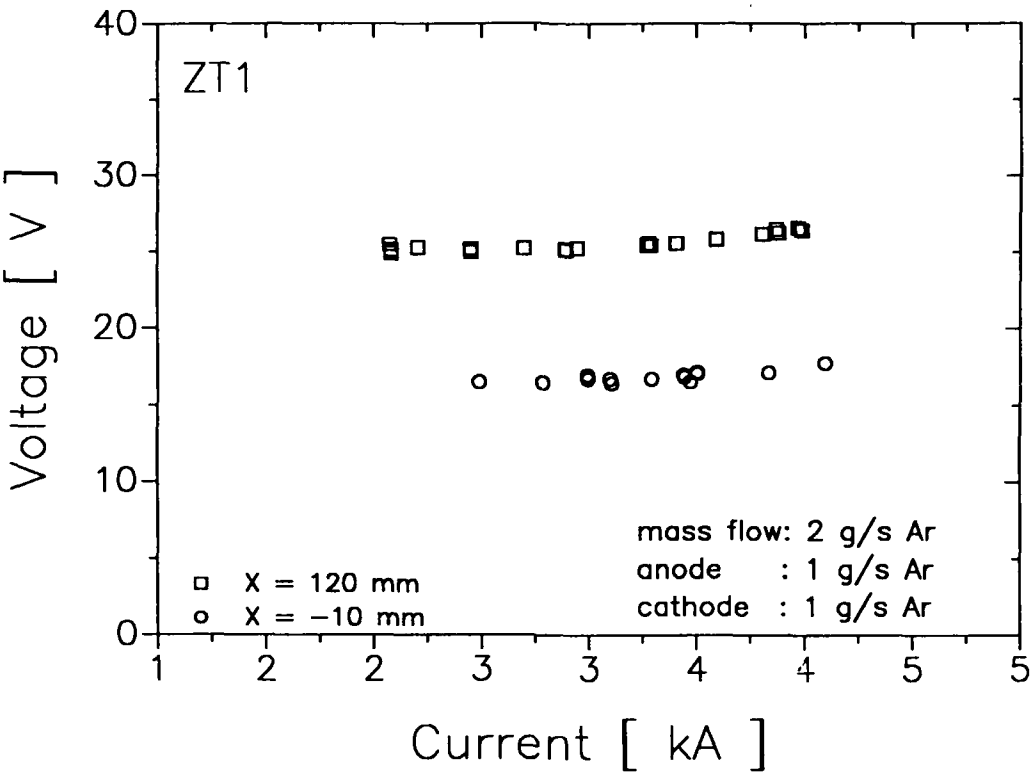

Fig. 2.3.13: Discharge voltage vs. current for a backward and a protruding cathode position

3. Cathode Phenomena

3.1 Erosion

In a previous research period [9] the erosion of MPD devices was investigated systematically. It was shown that two different modes must be distinguished (old erosion rates for argon as propellant in parentheses):

- ignition phase, determined by the cold cathode and by a spotty arc attachment ($\varepsilon \approx 13\ \mu g/C$). It ends when the cathode is hot enough to transit into thermionic emission. This is indicated by a sudden decrease in voltage, together with an increase in current (power supply response), depicted in Fig. 3.1 . The photo in Fig.3.2 shows a sequence out of a high speed movie (2000 frames/s) of the ignition of the ZT1 with the cathode in forward position. The sequence shows the cathode shortly before the transition to the thermionic mode: it already glowed faintly, but the bright "hopping" arc attachment spots can still be seen. The photos also show clearly that the plasma jet has not stabilized as in the "glowing phase".

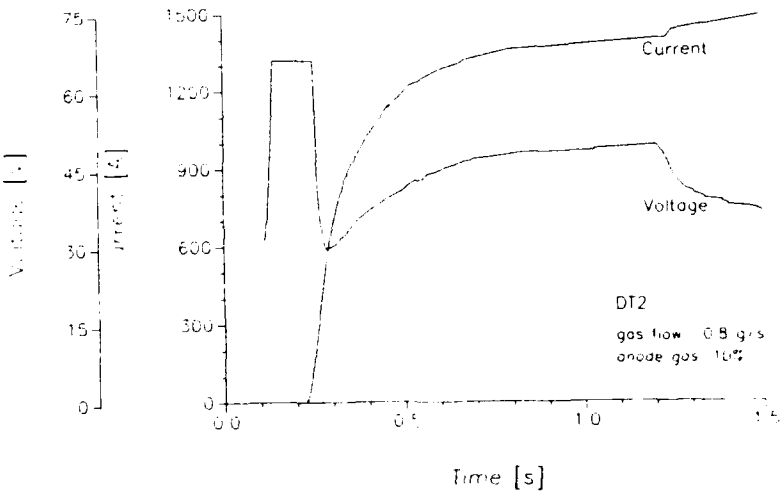

Fig. 3.1: Current and voltage transients during ignition phase

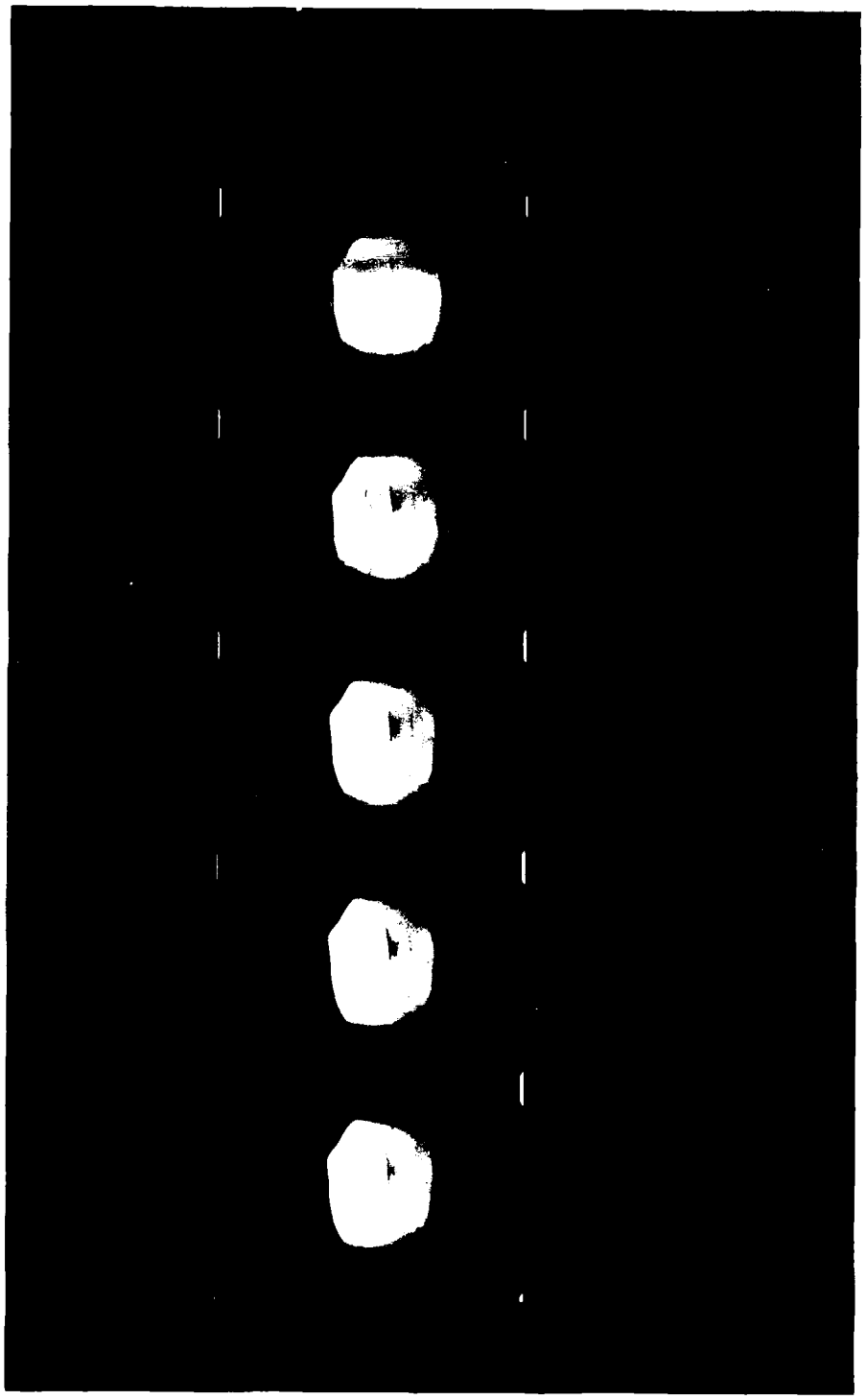

Fig. 3.2: High speed frames taken during the ignition phase, shortly before transition to the stable mode.(2000 frames/s, 0.8 g/s argon, 2000 A)

- steady state phase determined by thermionic emission (ε = 0.03 μg/C)

The above mentioned values had been reached with commercial welding argon, which was used directly. To avoid possible oxidation effects, which could augment erosion, in a new test series the welding argon was replaced by argon of purity grade 4.8 ($\hat{=}$ 99.998%). Additionally, the gas is cleaned by a drying and deoxigenation process ("Oxisorb" from Messer-Griesheim). With these means the following new erosion rates have been measured with argon:

- ignition phase: 6-7 μg/C
- thermionic phase: 1-2 ng/C

The erosion rates in the thermionic case are in the order of magnitude of the sublimation rate: using the formulas from [9] and the vapor pressure data from [10] and assuming current densities in the order of 10^7 A/m^2, which corresponds to the thruster conditions, the erosion rates depicted in diagram 3.3 are obtained. With these assumptions 2 ng/C corresponds to a cathode temperature of ca. 2800°C.

The vapor pressure was calculated according the following equation:

$$\lg p_V = (- 0.2185 \cdot a/T) + b$$

with a = 184099.8 and b = 9.230394 (Handbook of Chemistry and Physics, 51st edition).

The sublimation rate was calculated according to the modificated Dushman equation:

$$s(T) = \frac{\dot{m}_{subl}}{I} = \sqrt{\frac{M}{2\pi \mathcal{R} T}} \frac{p_v(T)}{j} \quad \left[\frac{\mathrm{kg}}{\mathrm{C}}\right]$$

In the further research periods these results as well as the influence of different species of propellants will be investigated systematically.

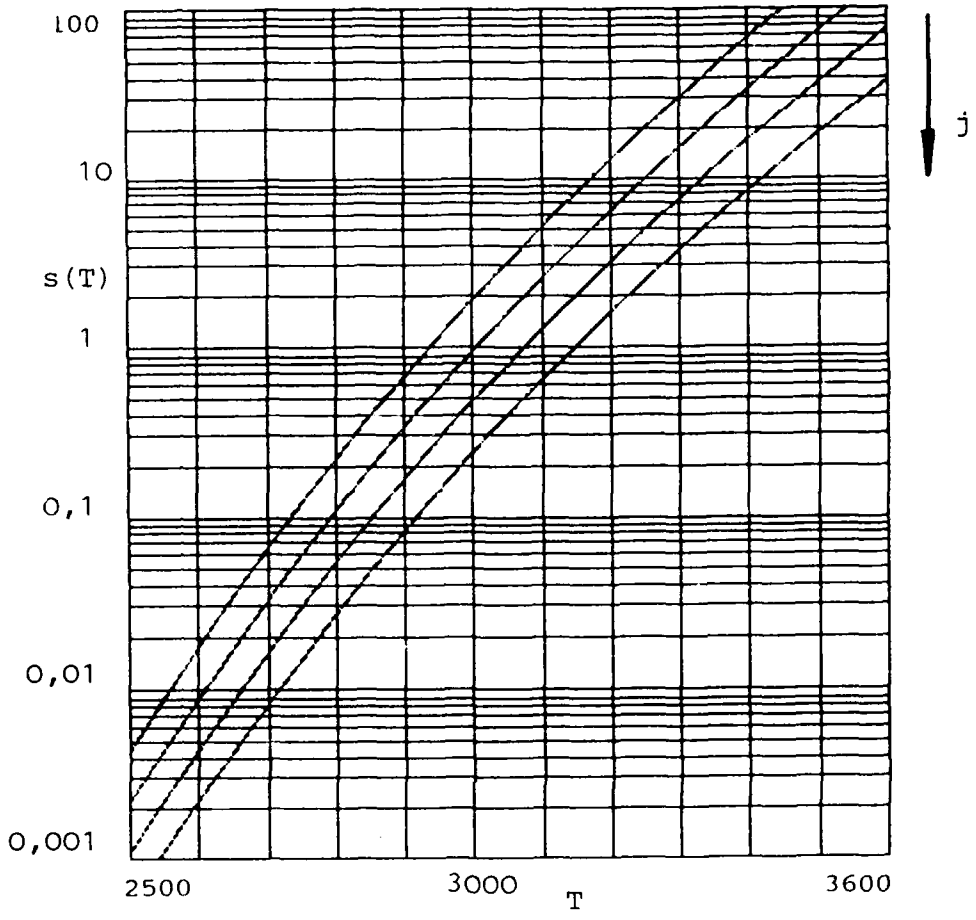

Fig. 3.3: Sublimation rates of tungsten in ng/C as a function of the cathode temperature in K with the current density as parameter (j = 0.5, 1.0, 2.0, 4.0 * 10^7 A/m^2)

3.2 High Current Cathode Damages

The typical cathode used in our steady state devices consists of a 2% thoriated tungsten rod - 50 mm (DT geometry) to 180 mm (ZT geometry) long and 12 to 18 mm in diameter, which is either clamped or, for higher current operation, cast in a water-cooled copper base.

At high current densities within the cathode (6000 A with a 14 mm ø and 8000 A with 18 mm ø), severe damages have been encountered with all thruster geometries. The cathode cracks and starts to melt, but not at the tip, where the heat transfer to the cathode is high and the maximum temperature was expected, but closer to the end of the tungsten part, near to the water-cooled copper base.

An example, a DT-cathode, is shown in Fig.3.4 . The melting begins inside the cathode, and because of the higher vapor pressure the cathode is "blown up". These "bubbles" crack and molten material flows out.

Fig. 3.4: Damaged cathode of the DT2-Thruster, current ca. 6500 A

Fig. 3.5: Metallographic cut through the damaged cathode

To clarify the reason for this behavior, cathodes will be investigated metallurgically in the neighboring Material Testing Institute in the follow-up research period. A first result is shown in Fig.3.5. A metallographic cut of the damaged cathode shown in Fig. 3.4 was prepared in a longitudinal direction. It was inspected in a scanning electron microscope (SEM) using secondary electrons, back-scattered electrons and x-ray microanalysis (energy dispersive and wave-length dispersive respectively).

The unaffected base material is characterized by a more or less homogeneous distribution of ThO_2 particles in the tungsten matrix, with diameters up to about 5 μm and 10 μm in the transverse and the longitudinal direction respectively. During operation the structure of the material changes depending on the local temperature. In regions of obviously relatively low temperature the ThO_2 particles show the tendency to spheroidize without changing their distribution or average size. In the region of the highest temperature the material melts, forming voids of diameters up to about 3 mm. The inner surface of these voids is covered with a layer of pure thorium oxide, about 0.05 mm to 0.15 mm thick. The dendritically resolidified material is of pure tungsten and does not contain any ThO_2 particles. In the temperature region below the melting temperature, recrystallization of the tungsten matrix occurs as well as a nearly perfect spheroidization and a considerable coarsening of the ThO_2 particles to diameters up to about 0.1 mm. This phenomenon is especially pronounced on the cathode tip side of the melted zone, and it is possibly a step which precedes the melting of the material.

4. Numerical Modeling of the Flow in MPD Accelerators

For geometry optimization of continuous self-field MPD thrusters, a stationary semi-two-dimensional computer code has been developed (Partly under contract AFOSR-86-0337) [11,12]. The extended Ohm's law is used to calculate the current contour lines. A one-dimensional, two-component expansion flow model is employed to obtain the velocity, pressure and heavy particle temperature distributions for calculating the gas properties. By means of the electron energy equation, the electronic temperature distribution is obtained.

The expansion flow inside the nozzle was assumed to be adiabatic for the ions and isothermal for the electrons. Outside the nozzle the expansion flow was considered hyperbolic and adiabatic for both components. Inside the nozzle of the thruster, the radial heat transportation is taken into account. The propellant used in this code is argon. In order to compare the results of the computations with measurements in a vacuum tank with residual gas pressure, this high temperature ($T_e \approx 10000$ K) residual gas is included into the model with an estimated free stream boundary.

a) Flow Field Equation

The flow field is taken as a one-dimensional, frictionless expansion flow, assuming adiabatic behavior for the ions and isothermal for the electrones within the whole thruster. The equation of state together with the continuity and Bernoulli equations yield the following expansion equation:

$$\frac{\kappa}{\kappa-1}\frac{p_c}{\varrho_c}\left(\frac{\kappa-1}{\kappa}ln\left(\frac{\varrho_c}{\varrho}\right)+1-\left(\frac{\varrho}{\varrho_c}\right)^{\kappa-1}\right)-\left(\frac{\dot{m}}{\varrho A}\right)^2 = 0$$

Herein, the indice c indicate the chamber conditions.

b) Electromagnetic Equation

Rewriting Ohm's law by means of Maxwell's equations, a vector equation for the magnetic induction vector $\vec{B}$ is obtained in the form:

$$\frac{1}{\mu_0}\nabla\times\left(\frac{1}{\sigma}\nabla\times\vec{B}\right)-\nabla\times(\vec{v}\times\vec{B})+\frac{1}{\mu_0}\nabla\times(\beta(\nabla\times\vec{B})\times\vec{B})=0$$

Here is σ the electric conductivity, ß the Hall factor and μ_0 the permeability in vacuum.

The electromagnetic equation is solved by a Gauss-Seidel iteration. The coupling to the flow field and the electron energy equation is achieved implicitly by calculating the plasma parameter.

c) Electron Energy Equation

For calculations in thermal non- equilibrium an electron energy equation is developed to determine the electron temperature distribution. Therefore, a two-dimensional, cylindrical and curvilinear code was written for the electron energy distribution corresponding to the flow field and the discharge code.

$$\frac{\vec{j}^2}{\sigma} + n_e \vec{v} \cdot \nabla \left(\frac{3}{2} k T_e \right) + p_e \nabla \cdot \vec{v} + \nabla \cdot \vec{q}_e^* = 0$$

Here $\vec{q}_e^*$ includes the heat flux due to the electron temperature gradients and the diffusion heat flux in the electron gas.

The electron energy equation is solved by a Gauss-Seidel iteration.

d) Numerical Results

In order to achieve a geometry optimization, two geometrical thruster configurations have been investigated experimentally. The throat diameter was changed from 24 mm to 12 mm at the thrusters (Fig. 2.1.1). In parallel, calculations were done for the different throat geometries. Fig. 4.1 and Fig. 4.2 shows the electron temperature and the potential lines for a mass flow rate of 0.8 g/s argon and for a current of 2 kA for both throat diameters. In Fig. 4.1 is the maximum electron temperature 37770 K for the big throat diameter and 51117 K for the small throat diameter. The voltage grows up from 39.7 V to 76.6 V at nearly the double value from the big to the small throat diameter (Fig. 4.2).

In the scientific report for the following research programm, this and other related codes wil be described in more detail.

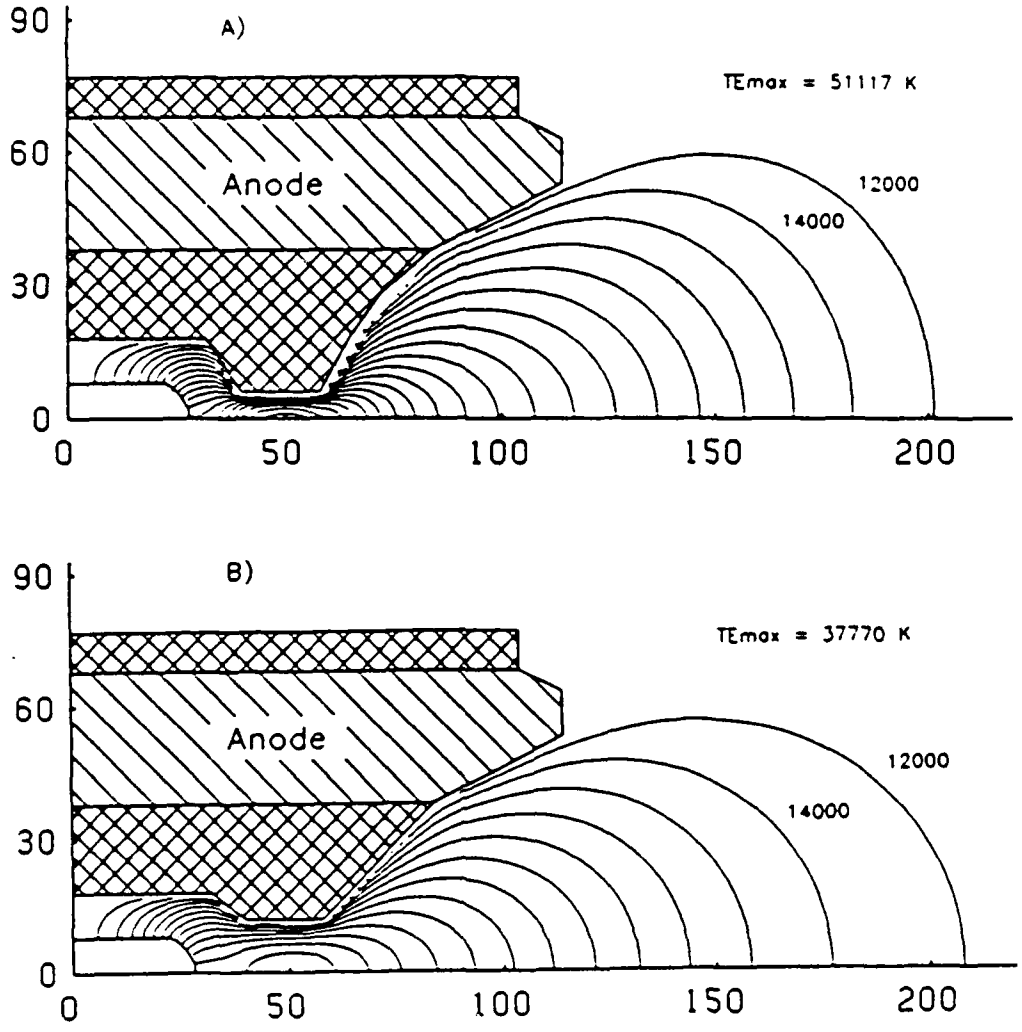

Fig. 4.1: Calculated electron temperature distribution for the thruster configuration: A) DT3 and B) DT2 for 0.8 g/s Ar and 2000 A

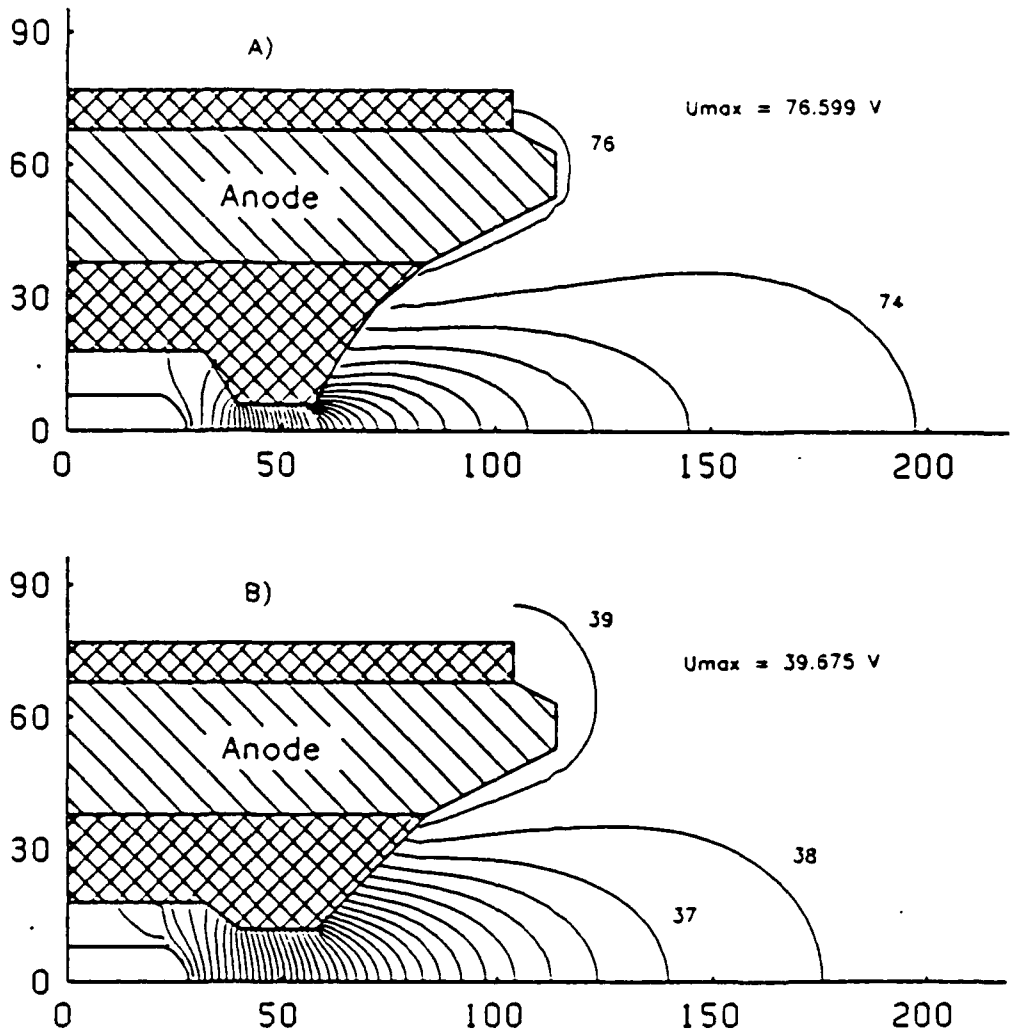

Fig. 4.2: Calculated potential lines for the thruster configuration A) DT3 and B) DT2 with the maximal potential difference (= discharge voltage)

5. References

[1] Auweter-Kurtz, M., Kurtz, H.L., Schrade, H.O.: Optimization of Electric Propulsion Systems Considering Specific Power as Function of Specific Impulse, Journal of Propulsion and Power, Vol. 4, No. 6, 1988, pp512-519

[2] Vondra, R.J., Caveny, L.H.: Plasmathruster Research in the U.S.A., Proceedings of the 17th IEPC, Tokyo, 1984, pp.20-27

[3] Schrade, H.O., Auweter-Kurtz, M., Kurtz, H.L., Merke, W.D., Sleziona, P.C.: Plasma Thruster Development, IRS-87-P-10, Final Report AFOSR-84-0394, Institut für Raumfahrtsysteme University of Stuttgart, 1987

[4] Auweter-Kurtz, M., Kurtz, H.L., Merke, W.D., Schrade, H.O. Sleziona, P.C.: Self Field MPD Thruster Investigations, IRS-P-10, Final Report ONR Grant No. N 00014-87-G-0119, Institut für Raumfahrtsysteme University of Stuttgart, 1988

[5] Hügel,H. "Zur Funktionsweise der Anode im Eigenfeldbeschlleuniger." DFVLR-FB 80-30, Köln, FRG, 1980.

[6] Schrade, H.O., Sleziona, P.C.: Performance Calculations of an H_2 Arcjet by Means of a Dual Channel Model, IEPC-88-104, in: Proceedings of the 20th IEPC, DGLR Bericht 88-02, Bonn, Germany, 1988

[7] King, D.Q., Smith, W.W., Jahn, R.G., Clark, K.E. "Effect of Thrust Chamber Configuration on MPD Arc Jet Performance," in Finke, R.C. (ed) : Electric Propulsion and its Applications to Space Missions, Progress in Astronautics and Aeronautics, Vol. 79, AIAA, New York, USA, 1981, pp. 504-517.

[8] Wolf, M., Kelly, A.J., Jahn, R.G., "A High Performance Magnetoplasmadynamic Thruster," IEPC 84-32, in : Proceedings of the JSASS/AIAA/DGLR 17th International Electric Propulsion Conference, Tokyo, Japan, July 84, pp. 206-212.

[9] Schrade, H.O., Auweter-Kurtz, M., Kurtz, H.L.:Cathode Erosion Studies on MPD Thrusters, AIAA Journal, Vol. 25, No.8, August 1987, pp1105-1112

[10] Weast, R.C. (ed.): Handbook of Chemistry and Physics, The Chemical Rubber Company, Cleveland, OH, 51st Edition, 1971

[11] Auweter-Kurtz, M., Kurtz, H.L., Schrade, H.O. Sleziona, P.C.: Numerical Modeling of the Flow Discharge in MPD Thrusters, Journal of Propulsion and Power, Vol. 5, No. 1, pp. 49-55,1989

[12] Auweter-Kurtz, M., Glaser S.F., Kurtz, H.L., Schrade, H.O. Sleziona, P.C.:An Improved Code for Nozzle Type Steady State MPD Thrusters, IEPC 88-043, in: Proceedings of the 20th IEPC, DGLR Bericht 88-02, Bonn, Germany, 1988